8-2008

Antennas and Arrays for Mobile Platforms -- Direct Broadcast Satellite and Wireless Communication

Songnan Yang
University of Tennessee - Knoxville

To the Graduate Council:

I am submitting herewith a dissertation written by Songnan Yang entitled "Antennas and Arrays for Mobile Platforms -- Direct Broadcast Satellite and Wireless Communication." I have examined the final electronic copy of this dissertation for form and content and recommend that it be accepted in partial fulfillment of the requirements for the degree of Doctor of Philosophy, with a major in Electrical Engineering.

Aly E. Fathy, Major Professor

We have read this dissertation and recommend its acceptance:

Marshall O. Pace, Paul B. Crilly, Mohamed Mahfouz

Accepted for the Council:
Dixie L. Thompson

Vice Provost and Dean of the Graduate School

(Original signatures are on file with official student records.)

To the Graduate Council:

I am submitting herewith a dissertation written by Songnan Yang entitled "Antennas and Arrays for Mobile Platforms — Direct Broadcast Satellite and Wireless Communication." I have examined the final electronic copy of this dissertation for form and content and recommend that it be accepted in partial fulfillment of the requirements for the degree of Doctor of Philosophy, with a major in Electrical Engineering.

Aly E. Fathy
Major Professor

We have read this dissertation
and recommend its acceptance:

Marshall O. Pace

Paul B. Crilly

Mohamed Mahfouz

Accepted for the Council:

Carolyn R. Hodges
Vice Provost and Dean of the
Graduate School

(Original signatures are on file with official student records.)

Antennas and Arrays for Mobile Platforms

-- Direct Broadcast Satellite and Wireless Communication

A Dissertation

Presented for the

Doctor of Philosophy

Degree

The University of Tennessee, Knoxville

Songnan Yang

August 2008

Dedication

This dissertation is dedicated to my parents, Jianchu Yang and Tonghui Zhao, for their generous love and tremendous support.

Acknowledgments

I wish to thank all those who helped me complete my Doctor of Philosophy degree in Electrical Engineering. I am indebted to all the professors and colleagues I have learned so much from at the University of Tennessee, Knoxville. I would like to express my deepest appreciation to Dr. Aly E. Fathy who introduced me to the field of antennas, without whom this dissertation could not possibly have been written. He has been a thoughtful mentor, and a great role model and friend in life. I would like to thank my committee members: Dr. Marshall O. Pace, Dr. Paul B. Crilly and Dr. Mohamed Mahfouz, for reviewing my dissertation and providing helpful advice. Especially, I would also like to thank Dr. Pace for teaching me the principles of Electromagnetic Compatibility and Dr. Mahfouz for introducing me to Micro-electro-mechanical Systems and supporting my training of Micro-fabrication at Cornell University, which are crucial to the completion of this work.

I must thank my previous department head Dr. Samir, M El-Ghazaly, my mentors during my internships at Intel Corporation: Dr. Ulun Karacaoglu, Vijay K. Nair, and Helen K. Pan, as well as Dr. Cheng Wang at the Mathematics department of UT, for their insights and continued encouragement throughout the research process. Special thank-yous also go to Dr. Shady H. Suleiman at Winegard Company for helping me with all the near field measurement of my antenna array prototypes. I owe my sincere gratitude to my colleagues from the antenna and microwave group: Yunqiang, Song, Alex, Adel, Joshua, Mohamed and Asia for many conversations that have provoked my thinking as well as for developing a harmonious and supportive community in the group. Especially, I would like to thank Sungwoo and Chunna for their continuous help with my research and experiments on the DBS antenna array and reconfigurable antennas respectively.

Last but not least, I would like to thank my family and friends, whose unfailing moral support made this work possible. A special thank-you must go to my loving partner and best friend, Hongmei Peng, for listening to my ideas and being there.

Abstract

Flexibility of any proposed communication links is becoming one of the most challenging features. Direct broadcasting satellite services, for example, will be greatly enhanced by providing service-on-the-move. This market is very demanding as it necessitates the development of a low cost, low profile antenna that can be mounted on top of SUVs and minivans, which is capable of continuously tracking the satellite. Another example is the wireless antennas for laptops and smart-phones, where the antennas should fit within an extremely small volume and should be capable of addressing many services over wide frequency range. In this dissertation, both DBS and the wireless antennas are addressed.

In these studies, efforts have been concentrated in developing low profile planar antennas, in particular, slot arrays. Travelling wave slotted waveguide arrays have been utilized to minimize the scanning angle range limits due to their inherent beam tilt angle. CNC machines were utilized first to fabricate the early prototypes for sub-array developments. Subsequently, a low cost fabrication technology is adopted to develop a low cost and light weight full array using substrate integrated waveguides (SIWs). The SIW is fully characterized and an excellent equivalent model has been derived to allow easy "translation" of metallic waveguide components to SIW. Various SIW junctions, transitions, and arrays have been developed for array feed networks including a 64 radiating SIW full array and a 32 radiating SIW array with folded feed.

Meanwhile, for the wireless antennas, the utilization of reconfigurable hardware has been introduced to provide the required multi-functionality services and wide frequency coverage. Various reconfigurable antennas were developed and utilized to demonstrate their advantages compared to other design options such as wide-band or multi-band approaches. Both micro-electro-mechanical switches "MEMS" and "PIN" diodes have been successfully utilized to switch between the different configurations. The placement, control, and modeling of the switches are also discussed and novel modeling and biasing topologies are introduced.

A novel and practical concept of reconfigurable multiband antenna is introduced here too, where advantages of both the multi-band and the reconfigurable antenna structures can be simultaneously achieved while supporting more services.

Table of Contents

List of Figures

List of Tables

Chapter 1

Introduction

Advances in satellite broadcasting and wireless communication have inspired the development of low cost and low profile antennas for mobile platforms to allow maximum connectivity where ever people goes, such as live satellite TV in a moving vehicle or internet and phone services on a laptop computer. There are two common and major challenges for such antennas. First, they should allow easy integration with existing mobile platforms. For example, satellite TV antennas need to have a very low profile to be integrated into the roof of an SUV or a minivan, while antennas for wireless communication are required to support more and more wireless standards in a limited space. Second, the cost of these antennas needs to be very low to justify the additional connectivity/functionality and the mass commercial implementations of these antennas. So, the topology of both satellite TV and wireless antennas need to be optimized to ensure an overall low cost of antenna system. Also, the fabrication/component cost of these antennas needs to be minimized.

Along these lines, the analysis and design of antennas targeting two major and distinctive aspects of the same problem of antennas and arrays for mobile platforms are investigated. These problems are summarized in the following sections.

1.1 Antenna Arrays for Mobile DBS Applications

Along the proliferation of back-seat video systems in vehicles like SUV and minivans, there is an increasing demand for the mobile reception of live entertainments, such as satellite TV. In the United States, the satellite antenna design should provide dual-circular polarization, and the antenna's beam is required to be steerable in two planes: 360° in azimuth, and 20º to 70º in elevation above horizon. Low profile reflector antennas, as shown in Figure 1.1, have been introduced, which can be mounted on the top of a RV and track the satellite mechanically while the vehicle is in motion. But the use of reflector antennas is still limited, especially for SUV and minivans, due to their large volume and a relatively high profile, i.e. height (> 12" with radome).

To reduce the height of the satellite antenna, planar phased arrays can be used, where the beam is steered electronically by controlling a large number of radiating elements individually to form a common phase front toward a certain direction. Although phase arrays can render a very low profile, a large number of microwave circuits, such as amplifiers and phase shifters, are required in the beam forming network, which results in a high cost and prevents mass volume commercial implementation.

Figure 1.1. Low profile reflector antennas used for mobile DBS reception

Hence, the mobile Direct Broadcasting Satellite (DBS) market requires a low profile, steerable and affordable antenna design to adequately cover the needs for DBS reception on the move. In the following chapters, planar travelling wave slotted arrays using conventional waveguides and substrate integrated waveguides (SIW) are introduced. The developed antenna arrays produce two circularly polarized beams at a large inherent tilt angle in elevation. Such beam tilt angle dramatically reduces the steering volume requirements and renders a low profile antenna (less than 3 inches), even when complete mechanical steering (in both elevation and azimuth) is utilized. Meanwhile, the Substrate Integrated Waveguide (SIW) technology is introduced to allow low cost antenna array fabrication.

1.2 Reconfigurable Antennas for Multi-Radio Wireless Platforms

As more and more wireless services are integrated into handheld platforms, such as laptop computers and mobile handsets, additional antennas are required. Instead of dedicating one antenna to one specific service, reconfigurable antennas can be dynamically reconfigured, by altering its antenna structure interconnections, to support one service at a time.

Multi-band antenna, on the other hand is currently the most popular antenna structure for multi-radio platforms. It supports multiple services at the same time but offers significantly less out of band noise rejection as compared to single band reconfigurable antennas. The disadvantage of multiband antennas is more apparent when multiple radios are operating simultaneously, where the poor isolation between them causes severe degradation of radio performances.

However, reconfigurable antennas require switches, which introduce additional cost, insertion loss and DC power consumption. Micro-Electro-Mechanical-Systems (MEMS) are the preferred switching devices due to their low loss and power dissipation. However, PIN diodes are viable alternative in reconfigurable antenna implementation before

MEMS's prices, process compatibility, and operating voltages become significantly lower.

In the following chapters, several reconfigurable antenna designs using both MEMS and PIN diode switches are presented. The concept of reconfigurable multiband antenna, i.e. reconfiguring the multi-band antenna, is also introduced, where multitudes of switches are used to hop between several multi-band configurations. Through judicious grouping of frequency bands for each configuration, advantages of both the multi-band and the reconfigurable antenna structures can be simultaneously achieved while supporting more services. The placement, controlling, and modeling of switching devices are also discussed and novel modeling and biasing techniques are introduced.

1.3 Contributions

This dissertation is consisted of two parts, addressing each of the above problems. The corresponding original contributions are listed below, details of which are discussed in the following chapters.

1.3.1 Mobile DBS Antenna Array

- Analysis of travelling wave slotted waveguides and substrate integrated waveguide (SIW) antennas with symmetric radiating elements.
- Development of synthesis equations for the design of waveguide and SIW T-junction power dividers with arbitrary power split ratio.
- Characterization of propagation and attenuation properties of the SIW and generalization of the design rules and equivalent dielectric filled waveguide model for its implementation in the radiating element and low loss feed network designs.
- Design of wide band transitions from CPWG to SIW and between two stacked layers of a multi-layer SIW structures.

- Implementation of a low profile multi-layer slotted SIW array antennas with tapered feed networks, which are folded to the back of the radiating elements.
- Developing a recipe for a systematic design procedure of the travelling wave slotted waveguide/SIW arrays.

1.3.2 Reconfigurable Antennas

- Development of new antenna concepts based on fractal structures suitable for reconfiguration with a low number of switches.
- Implementation of MEMS switches in wire antenna structure and PIN diodes in PIFA antenna structure.
- Introduction of novel reconfigurable multi-band antenna concepts.
- Design of reconfigurable multi-band meandered monopole antennas for mobile handsets and Twin PIFA antennas for laptop computers.
- Development of new models, identifying optimum placement and integration of DC bias lines of switches.

1.4 Document Organization

In the first half of this dissertation, Chapter 2 to Chapter 5 we will discuss the analysis and design of mobile DBS antennas. The development of reconfigurable antennas is presented in Chapter 6 to Chapter 8 — the second half of this presentation.

Chapter 2 reviews the DBS service and the antenna requirements for its mobile reception. The design challenges of such antenna are also discussed.

Chapter 3 starts with an analysis of the travelling wave slotted waveguide array antenna structure including the generation of circular polarization, control of the beam tilt angle and the optimization of element distribution, followed by the design, simulation and

measurement results of a single radiating waveguide slot array, a 6-waveguide sub-array and the design of a 48 radiating waveguide full array.

Chapter 4 begins with the characterization of propagation and attenuation of the substrate integrated waveguides (SIWs), followed by the study of antenna array feed network component designs using SIW structures. In this chapter, the relationship between SIWs and regular dielectric filled rectangular waveguides is studied to allow direct translation of waveguide structures to SIW. Waveguide junctions for antenna feeding networks, such as the T-junctions and Y-junctions are then translated into SIW and design equations / graphs are generalized. The transitions from SIW to planar circuits and between SIWs on different layers are also described at the end of the chapter.

Chapter 5 introduces a systematic design "recipe" for the synthesis of SIW radiating elements, including the determination of slots' length, spacing and number of slots per radiating SIW. It is followed by design examples and measured results of a 64 radiating SIW slot array and a 32 radiating SIW slot array with folded feed networks.

Chapter 6 serves as an introduction to the second half of the dissertation: and includes a discussion of reconfigurable antennas for multi-radio platforms. In this chapter, reconfigurable antenna concept is introduced. Antenna design challenges of multi-radio wireless devices are discussed and summarized by a comparison between various antenna options.

Chapter 7 demonstrates two single band reconfigurable antenna designs: the "Maze" antenna and the mini-Maze antenna. Both are based on fractal loop structures, where switches are used to control the circumference to render a reconfigurable resonant frequency. The mini-Maze offers a 75% size reduction relative to the original "Maze" and can be reconfigured, i.e. hopped between 3 single band configurations upon using 2 MEMS switches. The implementation of MEMS switches and related modeling considerations in an antenna environment is also discussed.

Chapter 8 introduces the concept of reconfigurable multi-band antennas by demonstrating two designs: meandered monopole antennas for mobile handsets and Twin PIFA antennas for laptop computers. A novel switch biasing scheme is also introduced here; where PIN diode switches are controlled by the DC signal carried by the antenna feeding cable.

Chapter 9 summarizes the relevant contributions of this work.

Chapter 2

DBS Service and Antenna Requirement for Mobile Reception

In this chapter, backgrounds about satellite broadcasting are given; the basics of this technology are reviewed as well, which can help the reader in understanding the various design constraints in our proposed design. It also gives a comparison between stationary reception of satellite broadcasting signals at home and in a mobile platform.

DBS stands for Direct Broadcast Satellite and refers to satellite television broadcasts intended for home reception. In the Americas, the Ku band DBS services have a downlink frequency band of 12.2GHz ~ 12.7 GHz. In the United States, the major service providers are DirecTV and DISH Network and the coverage is primarily in the continental US or CONUS. There are three major satellites located on the geostationary orbit, or GEO, providing the DBS services in US, the 101°W, 110°W and 119°W.

A brief summary of the characteristics of the Ku band US-DBS services is shown in Table 2-1 [1]. The antenna requirements for DBS reception in CONUS is discussed in the following sections by studying the required coverage, i.e. antenna steering range, of the mobile DBS service and analyzing the link budget for mobile reception of satellite TV. The design challenges of low profile mobile DBS antennas are also discussed at the end of this chapter.

Table 2-1 US DBS System Basic Parameters

Frequency Band	Ku, Downlink 12.2-12.7GHz, Uplink 17.3-17.8GHz	
Space Segment Bandwidth	500MHz	
Minimum Separation Between Adjacent Satellites	9° (e.g. 101°W, 110°W and 119°W)	
Satellite Services	BSS - Broadcast Satellite Service	
Satellite EIRP	51-60dBW (Equivalent Isotropic Radiated Power)	
Characteristic of radio channels	Channel Number	32
	Channel Bandwidth	24MHz
	Polarization	Dual Circular, LHCP & RHCP
Cross pole isolation	20dB	

2.1 Satellite Locations -- Geostationary Orbit

Along with most broadcasting satellites, the DBS satellites are located on the Geostationary Orbit (GEO), a circular orbit in the equatorial plane and concentric with the Earth, as shown in Figure 2.1. The altitude of the GEO satellite above the equator can only take values in the neighborhood of H such that the satellites orbits the Earth with the same period as the Earth rotates. This altitude, at which a dynamic equilibrium between the gravitational force and centrifugal force is achieved, can be approximated as:

$$G_g \frac{mM}{R+H^{\,2}} = m\left(\frac{2\pi}{T}\right)\ R+H$$

$$H = \sqrt[3]{G_g \cdot \frac{MT^2}{2\pi^{\,2}}} - R$$

Equation 2-1

Where G_g is the gravitational constant ($6.673 \cdot 10^{-11}$ $m^3kg^{-1}s^{-2}$), M is the mass of the Earth ($5.974 \cdot 10^{24}$kg), R is the radius of the Earth (6378km) and T is the period of the Earth's rotation (23hours, 56 minutes, and 4.1 seconds). H is calculated to be H = 35,768km, which is the altitude above the equator of all GEO satellites. With the altitude (H) and latitude (0°, or above equator) fixed, each GEO satellites can then be referred by their orbital position, or the longitudinal degree at which the satellite locates.

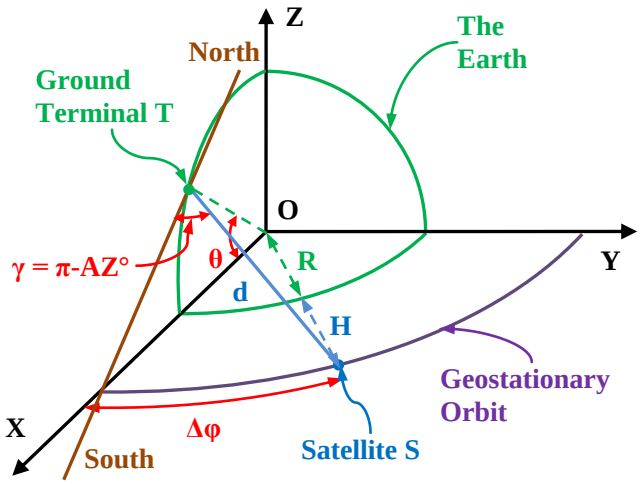

Figure 2.1 Satellite-Ground terminal geometry

2.2 Elevation, Azimuth Angles and Tracking Requirements

The angle at which the receiving antenna on the Earth should be pointing to, can be evaluated based on the receiver's geographic location, and each satellite's coverage specification can be derived. The surface that contains the satellite, the ground terminal and the center of the Earth can be extracted from Figure 2.1 as shown in Figure 2.2. The following trigonometric relations can be derived:

$$\tan EL^\circ = \frac{R+H \cdot \cos\beta - R}{R+H \cdot \sin\beta} \qquad \text{Equation 2-2}$$

$$\cos\beta = \cos\Delta\varphi \cdot \cos\theta$$

where EL° is the elevation angle at which the ground terminal points to the satellite, Δφ is the difference between the ground terminal's longitude and the GEO satellite's orbital position and θ is the ground terminal's latitude. After substituting their numerical values:

$$EL^\circ = \arctan\left(\frac{\cos\Delta\varphi\cos\theta - 0.1513}{\sin\beta}\right) = \arctan\left(\frac{\cos\Delta\varphi\cos\theta - 0.1513}{\sqrt{1-\cos^2\Delta\varphi\cos^2\theta}}\right) \qquad \text{Equation 2-3}$$

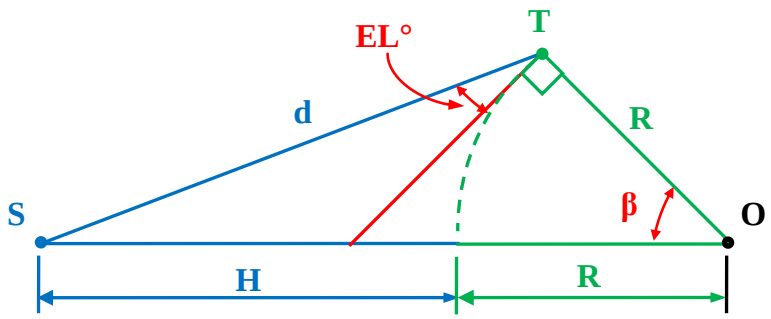

Figure 2.2 Elevation angle EL° calculation

where $0 \leq EL° \leq 90°$. For the azimuth angle at which the ground terminal points to the satellite, it can be shown that:

$$\tan \Delta\varphi = \sin\theta \cdot \tan\gamma$$

$$AZ° = \pi - \gamma = \pi - \arctan\left(\frac{\tan \Delta\varphi}{\sin\theta}\right) \qquad \text{Equation 2-4}$$

Where AZ° is the azimuth angle measured from the geographic north pole in the northern hemisphere. Subsequently, it can be seen that both azimuth and elevation angles are functions of the ground terminal's geographic location, and they also vary if a different satellite needs to be addressed. So, in order to cover all the DBS satellite services in the continental US, the elevation angles requirements of all major DBS satellites in US (101°W, 110°W and 119°W) are studied. As shown in Figure 2.3, the contour of elevation angles requirements for the reception of 119°W satellite in continental US is plotted. The required elevation angle ranges from less than 20° in northern Maine to more than 50° in southern Arizona. Meanwhile, a similar graph is plotted for the 101°W satellite in Figure 2.4, where the required elevation angle ranges from 30° in Seattle, WA to 60° in Houston, TX. The elevation angle requirements of all other satellites that has an orbital position between these two, such as the 110°W, should be within these limitations, i.e. 20° ~ 60° from horizon.

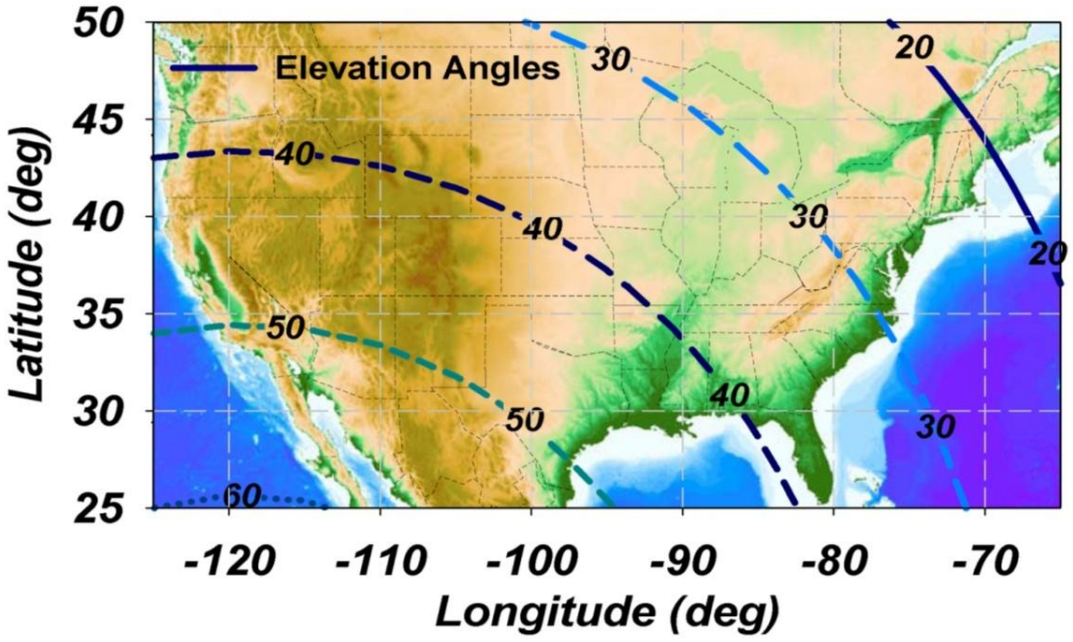

Figure 2.3 Elevation angles requirements for the reception of 119°W

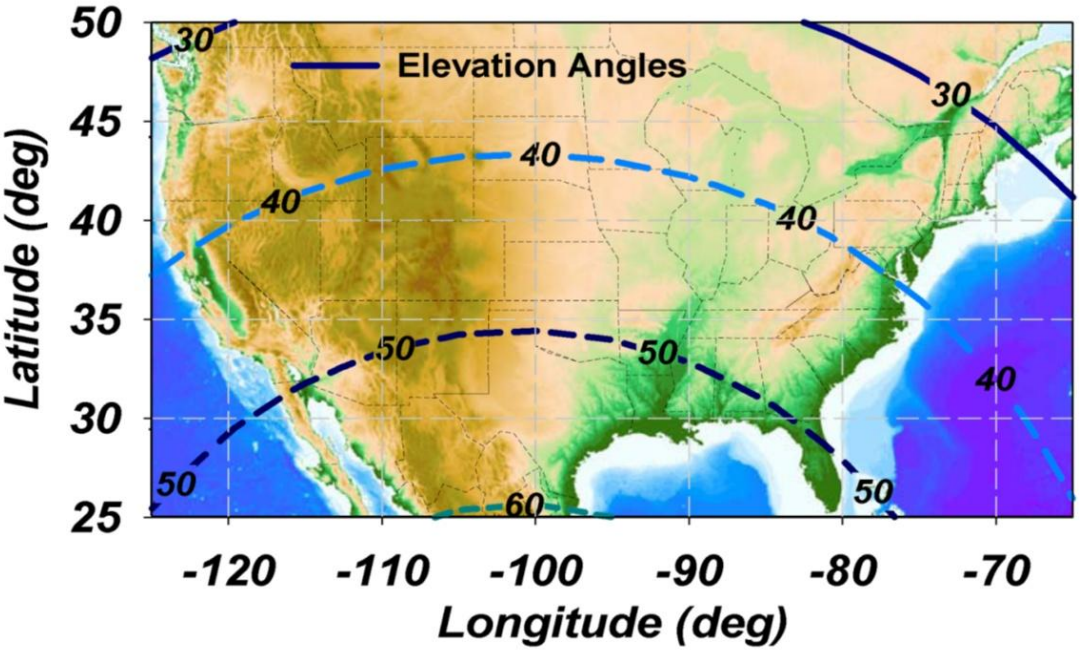

Figure 2.4 Elevation angles requirements for the reception of 101°W

So, for mobile reception of DBS services in CONUS, the antenna should at least have a beam steering range from 20° ~ 60° from horizon. Wider elevation coverage is necessary to cover the potential increase of elevation angle requirements while on the move, such as the slope of the road. So, elevation coverage of 20° ~ 70° is set as the goal for the mobile DBS antenna development. In the azimuth plane, the antenna should be able to track the satellite while the vehicle is moving towards whatever direction. So, a full 360° scan is required in the azimuth plane.

2.3 Link Budget Analysis and Gain Requirements

The carrier to noise ratio (C/N) is mostly used to evaluate the satellite broadcasting systems. It defines the ratio between carrier power at intermediate frequency (IF) and the corresponding noise power in the noise bandwidth (B) of the IF amplifier. For DBS system, the C/N can be written as:

$$\frac{C}{N} = \frac{P_t G_t G_r}{kTL_b B} = \frac{EIRP}{kL_b B} \cdot \frac{G_r}{T_A + T_R} = \frac{EIRP \cdot G/T}{kL_b B} \qquad \text{Equation 2-5}$$

where P_t is the transmitted power from satellite in watt, G_T and G_R are gain of the transmitting and receiving antennas respectively. T_A and T_R are the antenna noise temperature and the receiver noise temperate respectively in Kelvin. L_b represents the free space loss and k is the Boltzmann's constant ($1.38 \cdot 10^{-23}$ J/K).

EIRP stands for the Equivalent Isotropic Radiated Power, which identifies the power level that a theoretical isotropic antenna would need to be radiated to produce the peak power density observed. As shown in Figure 2.5, a typical footprint map of the DBS satellite located at 119°W is depicted as EIRP (dBW) contours. As can be seen, the signal strength is not uniformly distributed across the CONUS, where higher signal levels are transmitted toward the areas that suffer from higher path losses and more likely to rain, like the east coast and the south.

Figure 2.5 Typical EIRP footprint of DBS satellite at 119°W

G/T, the ratio between the receiving antenna's gain and the system's noise temperature, expressed in dB/Kelvin, is the figure of merit of the satellite receiving system. The system noise temperature is consisted of two parts, the antenna noise temperature and the receiver noise temperature. The antenna noise temperature can be estimated according to operating frequency and the satellite ground terminal's elevation angle. For Ku band satellite antennas with elevation looking angle less than 30°, a T_A of 35K is a close estimate for clear sky condition [2]. The receiver noise temperature can be calculated by:

$$T_R = F - 1\ T_0 \qquad \text{Equation 2-6}$$

where F is the receiver's noise factor and T_0 is ambient temperature, i.e. 290K, and the total system noise temperature is:

$$T_R = T_A + F - 1\ T_0 \qquad \text{Equation 2-7}$$

Currently, typical Ku band Low Noise Block (LNB) offers noise figure less than 1 dB. So, the corresponding system noise temperature is approximately 100K.

According to the Friis equation, the path loss L_b can be calculated as:

$$L_b = \left(\frac{4\pi d}{\lambda} \right)^2 \qquad \text{Equation 2-8}$$

where d is the distance between the satellite and the ground terminal, and λ is the free space wavelength. However, the distance d is different from one location to another. As shown in Figure 2.2, d can be calculated as:

$$d = \sqrt{R+H\ ^2 + R^2 - 2R\ \ R+H\ \ \cos\Delta\varphi\cos\theta} \qquad \text{Equation 2-9}$$

after substituting the numerical values, the path loss can be expressed in dB as:

$$L_b\ \ dB\ \ = 185 + 20\log f\ \ GHz\ \ + 10\log\ \ 1 - 0.296\cos\Delta\varphi\cos\theta \qquad \text{Equation 2-10}$$

The variation of path losses is plotted in Figure 2.6 , where the transmitted signal from 119°W satellite has a maximum of 0.7 dB differences across CONUS.

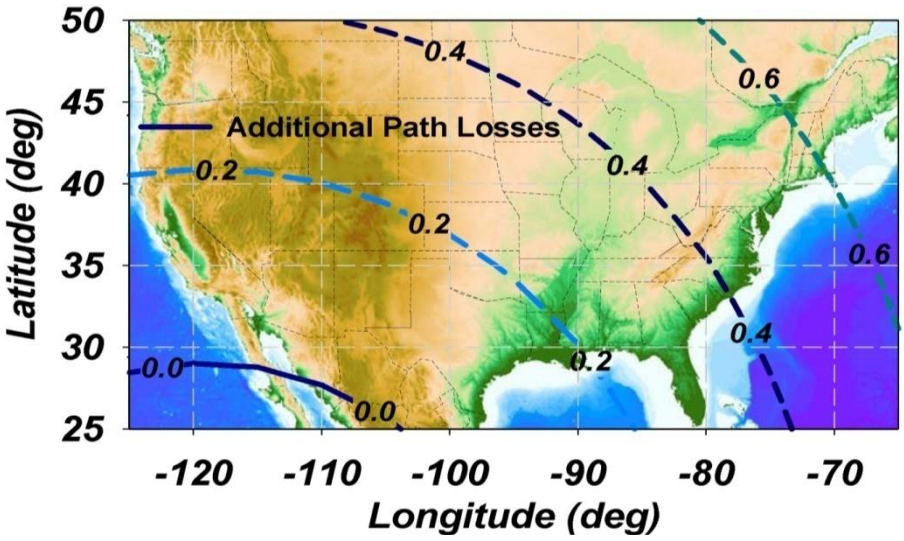

Figure 2.6 Additional path losses (dB) from 119°W satellite

In summary, the carrier to noise ratio can be calculated as:

$$C/N\ \ dB\ = EIRP\ \ dB\ + G/T\ \ dB/K\ \ - L_b\ \ dB\ - B\ \ dB.Hz\ \ + 228.6\ \ dBW/K.Hz \qquad \text{Equation 2-11}$$

For example, in Knoxville, TN area (36°N 84°W) the EIRP from 119°W satellite is approximately 53dBW (Figure 2.5). Noise temperature is about 100K or 20 dB.K. The IF bandwidth for Ku band service is 24MHz (Table 2-1), or 73.8dB.Hz. The path loss is calculated to be 206dB. The elevation and azimuth looking angle are: 35° from horizon and 230° from North. Numerically, we get:

$$C/N\ \ dB\ = G\ \ dB\ \ - 18.2\ \ dB \qquad \text{Equation 2-12}$$

According to the above equation, the required antenna gain can be derived from the receiver C/N ratio requirements.

The current DBS systems utilize digital transmission techniques to reduce the requirement for C/N [3]. Compared to analog video signals which typically requires a C/N of about 10-14dB, digital transmission can work with C/N values of 4-8dB, depending on the modulation and coding schemes [2].

In this case, the minimum antenna gain required to receive the digital DBS signal ranges from 22.2dB ~ 26.2dB in a clear sky condition. For stationary reception of DBS, the reflector antennas usually offer a gain margin of over 9dB [4] (or a gain of ~ 33.2dB), to ensure the reliability is greater than 99.7%, that is less than 30 hours of outage per year. In the mobile case, a slightly lower reliability of 99% is acceptable which reduces the link margin by more than 2dB. So in our mobile DBS antenna development, the antenna gain needs to be greater than 31dB with a G/T greater than 11dB/K.

2.4 Low Profile Mobile DBS Antenna Design Challenges

As a summary, a list of the required mobile DBS antenna specifications is shown in Table 2-2**,** where the major challenges for the design of such low profile DBS antenna are the following:

- To achieve a wide scanning range in the elevation while maintaining a low profile antenna.
- To construct a large antenna/array to achieve a high gain while sustaining a highly efficient antenna feed, hence a high efficiency and G/T
- To generate dual circular polarization beams pointing toward a large elevation angle while supporting good axial ratio
- To keep the overall antenna cost down while keeping the same manufacturing accuracy.

The solutions to these challenges will be discussed in the following chapters.

Table 2-2 Required Specifications for Mobile DBS in USA

Antenna Gain	> 31 dB
Maximum physical Area	1 m diameter
G/T	>11dB/K
Azimuth Coverage	$\Phi = 360^{o}$
Elevation Coverage	$20^{o} < \theta < 70^{o}$ from Horizon
Polarization	Dual Circular
Low Profile	< 3"

Chapter 3

Travelling wave slotted Waveguide Array Antennas

As discussed in chapter 2, the key challenge for the mobile DBS antennas is to achieve a high gain with a very low profile. Planar microstrip arrays are the most popular structure for high gain broadside antenna developments. If electronically steered by costly phase shifters, they will best suit this low profile. However, they may experience significant gain drop and unacceptable cross-polarization when scanning off broadside up to extreme angles, i.e. ±70° degrees. On the other hand, if planar broadside arrays are mechanically steered, the overall antenna height at large scanning angles will not meet the low profile requirement. Add to that, these large planar microstrip arrays are relatively inefficient due to the accumulated losses of their feed networks [5]. Therefore, in order to circumvent these serious structural and efficiency problems, the utilization of travelling wave slotted rectangular waveguide arrays has been evaluated. As they can be a very viable alternative to planar broadside antennas for their low steering volume and superior insertion loss performance in comparison to that of planar microstrip arrays. The proposed slot array based antenna topology would require mechanical steering for both the elevation and the azimuth directions. The 360° in azimuth can be achieved using a "Lazy Susan", and the mechanical steering in elevation could be limited to ±25º or less by the inherent beam tilt angle of the travelling wave arrays, which could lead to overall height reduction of the

antenna and avoiding the aperture projection loss and significant unacceptable cross polarization degradation due to electronic steering at the extreme scanned angle of 70º.

In section 3.1, the generation of circular polarization, control of beam tilt angle and the optimization of element distribution will be discussed. In section 3.2, the design of a single radiating waveguide slot array will be demonstrated, followed by the simulation and test results of a 6-waveguide sub-array in section **Error! Reference source not found.**, design of the full array with conclusion will be given in section 3.3 and conclusions in section 3.4.

3.1 Analysis of Circularly Polarized Travelling Wave Slot Array

Travelling wave slot array antennas' main beam radiation is off broadside and can be designed for circular polarization with relatively low axial ratio [6]. The beam's off-broadside tilt angle could be selected in the middle of the scanning range in order to reduce the pitfalls associated with the wide scanning angle. The aperture distributions can also be tapered to achieve a desirable balance between gain/efficiency and sidelobe levels. Moreover, a slot array with symmetrical element distributions can also be fed from both waveguide ports/sides to receive signals with either type of circular polarizations. The above features of the travelling wave slot array will be discussed in detail in the following sub-sections.

3.1.1 Design for Circular Polarization:

Slots with certain shapes, when cut at a proper location on the broad wall of rectangular waveguide, can produce circularly polarized radiation "CP" [7]. Generally, to achieve a proper circular polarization, two orthogonal currents with the same magnitude and are quadrature in phase need to be excited by these slots. As shown in Equation 3-1, the magnetic field of the dominant mode (TE_{10}) in a rectangular waveguide can be expressed as [8]:

$$H_x^+ = H_0 \frac{\beta_z}{\omega\mu\varepsilon}\frac{\pi}{a}\sin\left(\frac{\pi}{a}x\right)e^{-j\beta_z z}$$
$$H_y^+ = 0 \qquad \text{Equation 3-1}$$
$$H_z^+ = -jH_0\frac{1}{\omega\mu\varepsilon}\left(\frac{\pi}{a}\right)^2\cos\left(\frac{\pi}{a}x\right)e^{-j\beta_z z}$$

The transverse (H_x) and longitudinal (H_z) components are inherently orthogonal in space, have quadrature phase and have the same magnitude, i.e. $|H_x|=|H_z|$ at a specific location x:

$$\beta_z \sin\left(\frac{\pi}{a}x\right) = \frac{2\pi}{\lambda}\sqrt{1-\left(\frac{\lambda}{2a}\right)^2}\sin\left(\frac{\pi}{a}x\right) = \frac{\pi}{a}\cos\left(\frac{\pi}{a}x\right)$$
$$x = \frac{a}{\pi}arcctg\left[\pm\sqrt{\left(\frac{2a}{\lambda}\right)^2 - 1}\right] \qquad \text{Equation 3-2}$$

where λ is the free space wavelength.

So, at these locations, the magnetic fields excite orthogonal surface currents with equal magnitude and quadrature phase, according to the boundary condition $\vec{J} = \hat{n}x\vec{H}$. Furthermore, if a circular hole is cut on the broad wall of a waveguide, the interrupted surface current will produce circular polarized radiation.

There are two locations that are possible solutions to get CP, but they correspond to different leading or lagging conditions of the H fields that will determine the sense of the circularly polarized surface currents. As shown in Figure 3.1, for propagation in the +z direction, a hole cut on the left solution location (i.e. x > a / 2) will create a Right Hand Circular Polarized (RHCP) wave, while on the right solution location (i.e. x < a / 2) will create a Left Hand Circular Polarized (LHCP) wave. Obviously, for propagation in the negative -z direction, the senses of these rotations are reversed.

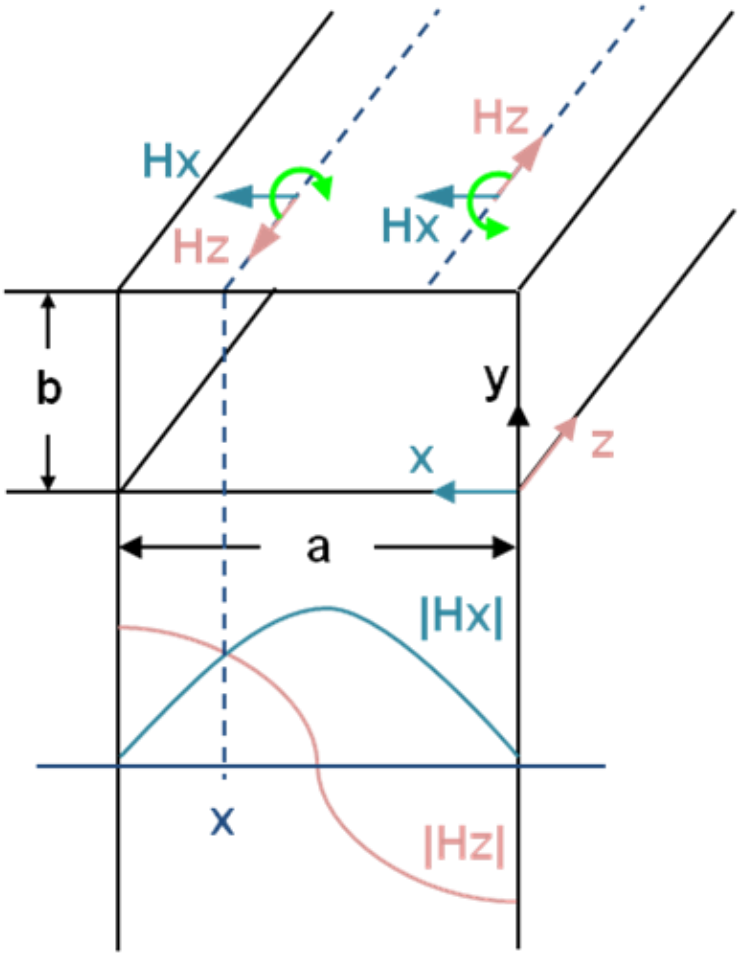

Figure 3.1 Field components for TE_{10} mode and locations of CP excitation

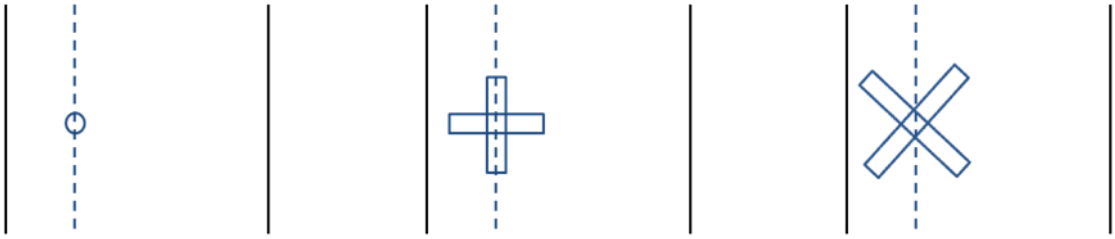

(a) (b) (c)

Figure 3.2 Radiating element configurations (a) Small hole radiating CP, (b) Small slot pair radiating CP, (c) Non resonating slot pair radiating CP

The radiation of a small hole in the broad wall of a guide is limited as it does not have many degrees of freedom, hence we will use a pair of crossed slots instead. For example, the length of these slots shown in Figure 3.2 can be used to control the amount of radiated power. Additionally, the slot pair can also have any arbitrary orientation. Hence, it is more convenient to rotate them by a 45° in order to allow cutting relatively long slots.

3.1.2 Beam Tilt Angle Control

In order to achieve a certain beam tilt angle (θ°), a travelling wave slot array topology is selected. The travelling wave arrays when compared to the standing wave antenna arrays can create off broadside beam radiation, they are easier to be matched at the input, but may have lower aperture efficiency due to uneven aperture distributions and the absorbed power lost and dumped in their terminations. As shown in Figure 3.3, multitudes of non-resonant crossed slot pairs are closely arranged on the broad wall of a rectangular waveguide. The "X" shaped slots are offset from the waveguide center line and optimized to achieve a good circular polarization.

According to the traditional travelling wave antenna theory [9], the beam tilt angle can be determined by Equation 3-3, where β_z represents the longitudinal wave number within the waveguide, k_0 is the free space wave number, and θ is the beam tilt angle measured from zenith.

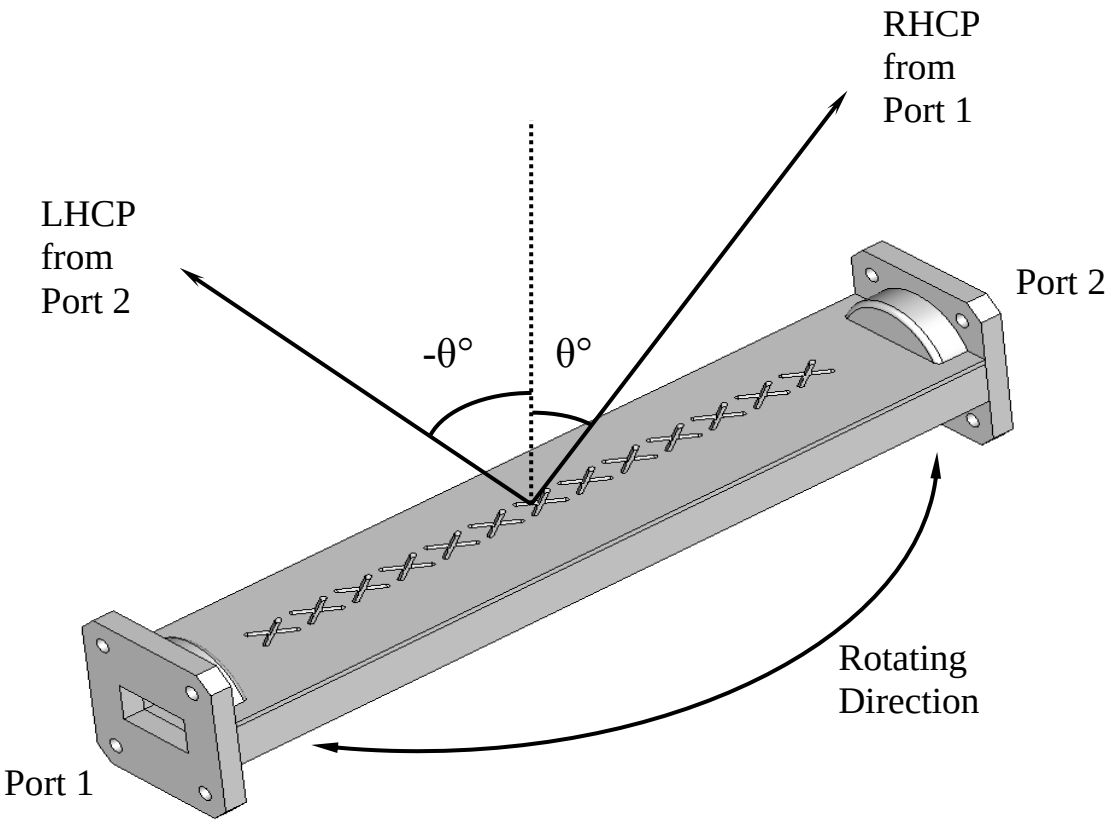

Figure 3.3 Single waveguide travelling wave slot array

$$\theta = \arcsin\left(\frac{\beta_z}{k_0}\right) \qquad \text{Equation 3-3}$$

However, Equation 3-3 is only appropriate for long leaky wave antennas with a constant cross section and that have very relatively low leakage factors through these slots. In our case, due to the low profile height requirement during mechanical scanning in the elevation, the radiating waveguide overall length is limited. Hence the maximum number of slots per radiating waveguide is in the range of 10-15. Each of these slots need to radiate a large fraction of the power passing by it, or in other words, having a relatively strong leakage/coupling coefficient [10]. Such coupling disturbs the fields' distribution of the wave traveling down inside the waveguide, and introduces sudden jumps of the phase

of both the radiated wave (P_r) outside the waveguide and the travelling wave (P_t) inside that waveguide.

The phase diagram of two adjacent slots of the designed travelling wave antenna is shown in Figure 3.4. The main beam location of the travelling wave antenna is formed when all the radiation from all the slots are combined in space in phase. For a rectangular waveguide, where the beam is pointing forward ($\theta > 0$), the phase relationship is:

$$P_{r1} + k_0 \cdot L \sin\theta = P_{t1} + \beta_z \cdot L + P_{r2} \qquad \text{Equation 3-4}$$

where P_r and P_t represents the phase change of the radiated and travelling wave caused by the slots respectively.

Here, in this slotted array analysis, we approximately assume that the phase change introduced to the radiated wave of two adjacent slots with similar size is the same, i.e. that is $P_{r1} = P_{r2}$, then the relationship of Equation 3-4 can be simplified as shown in Equation 3-5.

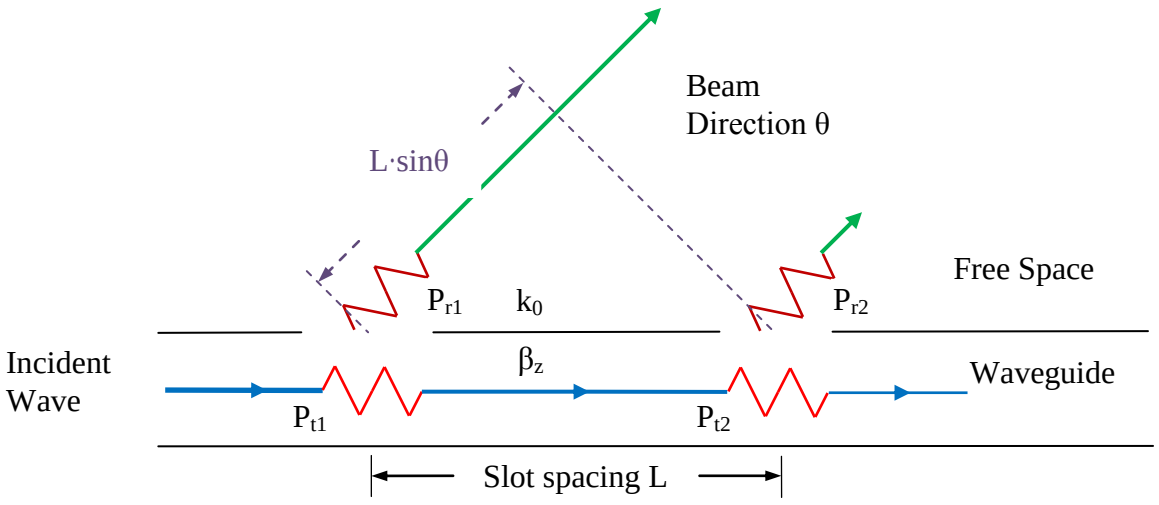

Figure 3.4 Phase diagram of travelling wave slot antenna (cross section)

$$\sin\theta = \frac{\beta_z}{k_0} + \frac{P_{t1}}{k_0 \cdot L} = \sqrt{1 - \left(\frac{\lambda}{2a}\right)^2} + \frac{\lambda \cdot P_{t1}}{2\pi L} \qquad \text{Equation 3-5}$$

The first term is the beam tilt according to Equation 3-3 and it can be controlled by changing the waveguide width ("a" dimension). The second term represents the additional phase shift introduced by the strongly coupled slots, and it is a function of both the coupling strength (defined by the slot length) and the element spacing and it can be evaluated numerically as will be discussed in Chapter 5. The same additional phase change phenomenon can also be treated as a change in β_z due to the loading of these slots as described in [11], which yields the same results.

The beam tilt angle is a function of the operating frequency as well. At higher frequency, the beam tilt angle decreases (moving toward zenith) and vice versa. This beam squint needs to be taken into account in the elevation steering, where the antenna should be adjusted according to its operating frequency — a major drawback for these types of antennas.

3.1.3 Aperture Distribution Optimization

According to the previous analysis, the selected travelling wave crossed slot array structure is capable of receiving dual circular polarization by feeding both ends of the waveguide. As can be seen from Figure 3.3, when the "X" shaped slots are excited by the TE_{10} mode propagating from Port 1 to Port 2, the slots radiate RHCP, and the beam tilt angle off-broadside is θ. Similarly, when the same slots are excited by TE_{10} mode traveling in the opposite direction, a LHCP with a beam tilt angle of $-\theta$ is generated. However, in order to address the same satellite, it is necessary to mechanically rotate the whole antenna by a 180 degree in azimuth to switch between the two polarizations, therefore this will only provide one polarization at a time — another drawback in this type of antennas.

In traditional traveling wave antenna array designs, the coupling of these radiating elements (the slot length in this case) is usually tapered to be monotonously increasing such that the array elements have almost uniform excitation, so as to achieve a maximum aperture efficiency. However, in order to have the same performance for both RHCP and LHCP, this slot array design needs to be symmetric with reference to the center. Hence, conventional tapering cannot be applied and the tapering of this symmetric distribution scenario needs to be studied; details will be given below.

3.1.3.1 Formulation

For an array of N slots, we will assume that each of these slots has a coupling factor of α(n), (n = 1. 2. 3. ... N). This coupling factor represents how much of the power passing through this particular slot is radiated, and this should be directly related to the length of and the spacing between these slots. According to the symmetry of the slot dimensions, α(n) = α(N-n+1). Also, assume that P(n) indicates the total power coupled to the n-th slot, and the total power is normalized to 1, that is P(1) = 1. Then we define the normalized aperture field intensity as E(n):

$$
\begin{aligned}
&P(1)=1;E(1)^2=\alpha(1)P(1)\\
&P(2)=1-E(1)^2;E(2)^2=\alpha(2)P(2)\\
&P(3)=1-E(1)^2-E(2)^2;E(3)^2=\alpha(3)P(3)\\
&\vdots\\
&P(N-1)=1-\sum_{n=1}^{N-2}E(n)^2;E(N-1)^2=\alpha(2)P(N-1)\\
&P(N)=1-\sum_{n=1}^{N-1}E(n)^2;E(N)^2=\alpha(1)P(N)\\
&T=P(N+1)=1-\sum_{n=1}^{N}E(n)^2
\end{aligned}
\qquad \text{Equation 3-6}
$$

where T is defined as the power leftover after the last slot, or in other words, the termination loss. The above equation assumes that the slots are way shorter than the length required for resonance, and not much reflection is generated from each slot. Under these conditions, it is acceptable to neglect reflections at the input port to simplify the array analysis and synthesis.

The antenna directivity is defined as the ratio of the peak radiation intensity in a certain direction and the total radiated power [12]. It can also be expressed as the ratio between the radiated power density (W) at certain location versus the power density resulted from an isotropic source (W_i) with the same total radiated power (P_{total}). In this case, the peak directivity is designed to be at θ off broadside, assuming each element's radiation is controlled to be in phase at this angle, we can express the peak power density as:

$$W\ \theta, r\ = \frac{\left|E\ \theta, r\ \right|^2}{L_b\ \ r} = \left(\sum_{n=1}^{N} \left| E\ \ n\ \right| \right)^2 \Big/ \frac{\lambda^2}{4\pi r^{\ 2}} \qquad \text{Equation 3-7}$$

and at the same location, the power density generated from an isotropic source with same total power is:

$$P_{total} = \sum_{n=1}^{N} \left| E\ \ n\ ^2 \right| = 1 - P\ \ N + 1\ = \ 1 - T \qquad \text{Equation 3-8}$$

$$W_i\ \ r\ = \frac{P_{total}}{4\pi r^2} = \frac{\sum_{n=1}^{N} \left| E\ \ n\ ^2 \right|}{4\pi r^2} \qquad \text{Equation 3-9}$$

Where P_{total} is the total radiated power, so the directivity at θ can be expressed as:

$$D\ \theta\ = \frac{W\ \theta, r}{W_i\ r} = \frac{4\pi \cdot \left(\sum_{n=1}^{N} \left| E\ n\ \right| \right)^2}{\lambda^2 \cdot \sum_{n=1}^{N} \left| E\ n\ ^2 \right|} \qquad \text{Equation 3-10}$$

Accounting for the termination loss, the expression for the gain can be derived and is given by Equation 3-11. For a given aperture size, the antenna efficiency (gain over directivity) is proportional to the antenna gain.

$$G\ \theta\ = D\ \theta\ \cdot\ 1 - T\ = \frac{4\pi}{\lambda^2} \cdot \left(\sum_{n=1}^{N} \left| E\ n\ \right| \right)^2 \qquad \text{Equation 3-11}$$

So the antenna efficiency can be optimized by maximizing the sum of the aperture field density under the conditions of both satisfying Equation 3-6, and the assumption of low reflections due to the successive slots discontinuities.

3.1.3.2 Uniform coupling case

Here, we assume that all the N slots have the same power coupling coefficient α(n), which is the same percentage of power passing by the slot is radiated. As a result, the slots are inherently symmetric and the excitation of the aperture decreases as the power travels down the waveguide. If we assume an infinite array, then the aperture field density can be expressed as:

$$E\ n\ ^2 = \alpha\ 1 - \alpha\ ^{n-1} \qquad \text{Equation 3-12}$$

As shown in Figure 3.5, the normalized gains of slot arrays with different number of elements are derived against different uniform coupling factor, where the corresponding α for a maximum antenna gain/efficiency can be obtained and shown in Table 3-1.

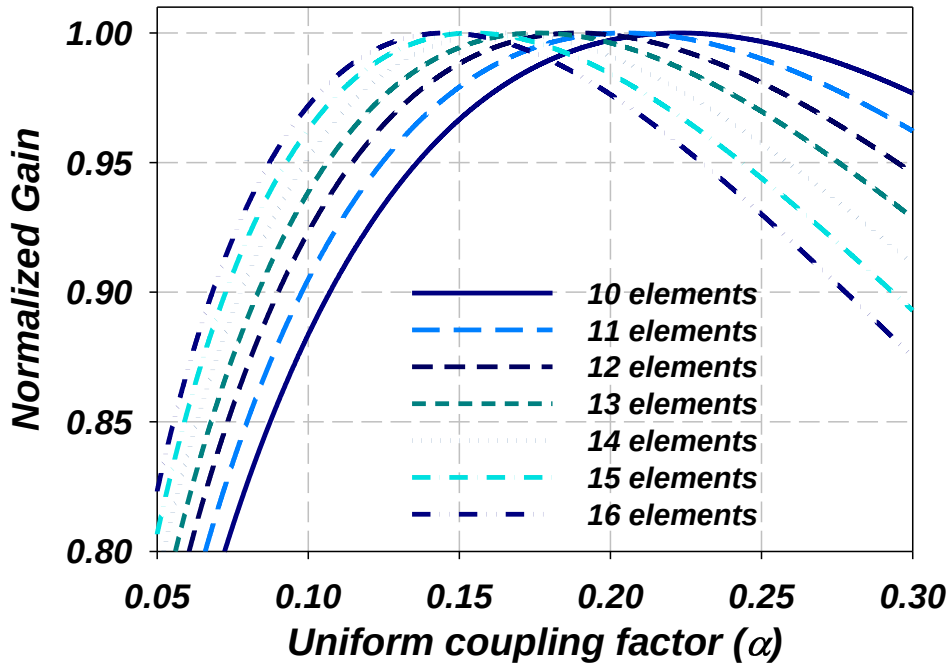

Figure 3.5 Normalized gain of antenna array with uniform radiating elements

Table 3-1 Coupling factors for the maximum gain of a uniform radiating element array

Number of radiating elements	10	11	12	13	14	15	16
Optimum coupling factor	0.223	0.205	0.189	0.176	0.165	0.154	0.146

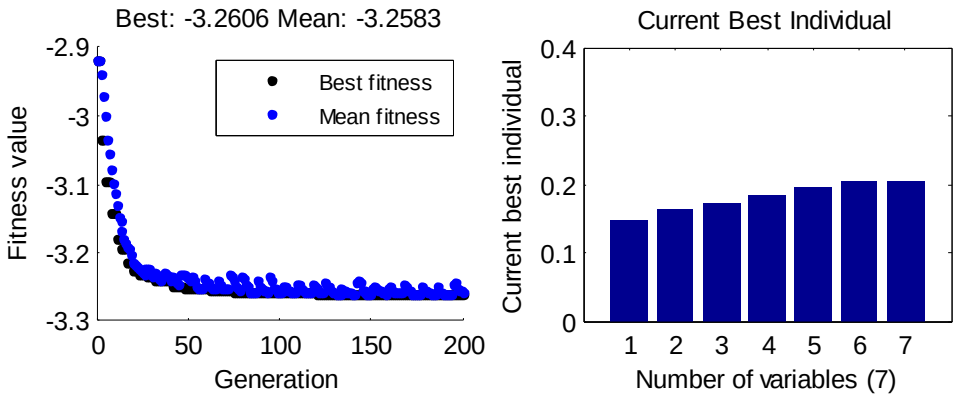

Figure 3.6 GA optimization of symmetric array with 7 coupling factor variables

3.1.3.3 Non-uniform coupling case

The slot dimensions can also be tapered to control the sidelobe levels and gain. However, for an N element array, there are N/2 variables need to be optimized. Hence, it is very convenient, in this case, to use Genetic Algorithm (GA) to perform the optimization. As shown in Figure 3.6. for a symmetric array with 7 variables (13-14 radiating elements), the coupling factors can be optimized in a few hundred generations using GA, which takes only a few seconds for a PC. The optimum coupling factors for a symmetric array are listed in Table 3-2.

3.1.3.4 Comparison of Distributions

After carrying out the previous analysis, we have optimized the power coupling factor distribution of the radiating elements along a travelling waveguide. Here we compare the synthesized aperture distribution and the far field gain patterns using three different suggested optimized distributions. They are: a. Uniform aperture distribution, commonly used in Leaky Wave antenna arrays, where radiating elements are tapered to achieve E(n) = const. b. Uniform radiating element coupling factor optimized for maximum gain, where $\alpha(n)$ = const. as shown in Table 3-1 c. Coupling factor and aperture distribution optimized for maximum gain, as shown in Table 3-2.

Table 3-2 Optimum coupling factors for a symmetric travelling wave array

Number of elements	α(1) & α(N)	α(2) & α(N-1)	α(3) & α(N-2)	α(4) & α(N-3)	α(5) & α(N-4)	α(6) & α(N-5)	α(7) & α(N-6)	α(8) & α(N-7)
10	0.1908	0.2104	0.2294	0.2450	0.2540	N/A	N/A	N/A
11	0.1742	0.1907	0.2070	0.2212	0.2312	0.2349	N/A	N/A
12	0.1603	0.1743	0.1884	0.2012	0.2112	0.2168	N/A	N/A
13	0.1485	0.1606	0.1728	0.1842	0.1938	0.2002	0.2025	N/A
14	0.1382	0.1488	0.1594	0.1697	0.1786	0.1853	0.1890	N/A
15	0.1293	0.1385	0.1480	0.1571	0.1654	0.1721	0.1765	0.1779
16	0.1215	0.1296	0.1380	0.1462	0.1538	0.1602	0.1650	0.1675

Take N = 13 for example, the required coupling factor distribution for the three cases are shown in Figure 3.7(a), and the corresponding aperture distributions are shown in Figure 3.7(b), where it is obvious that in order to achieve a uniform aperture distribution, the coupling factor cannot be symmetric along the array center. Also, the last radiating element is required to radiate a 100% of the power passing by, which is obviously very hard to achieve. However, such uniform aperture distribution does give an idea about the highest gain, as shown in Figure 3.8, where the normalized gain of the travelling wave antenna with isotropic radiating elements at half wavelength spacing and 45° progressive phase advance is plotted. It is calculated that the uniform coupling distribution gives about 0.9dB less gain than the uniform aperture distribution case. Similar results are obtained for different element numbers. In our case, this gain drop is the price for trying to feed from both ends of the waveguide and harvest both circular polarizations using the same slot array antenna.

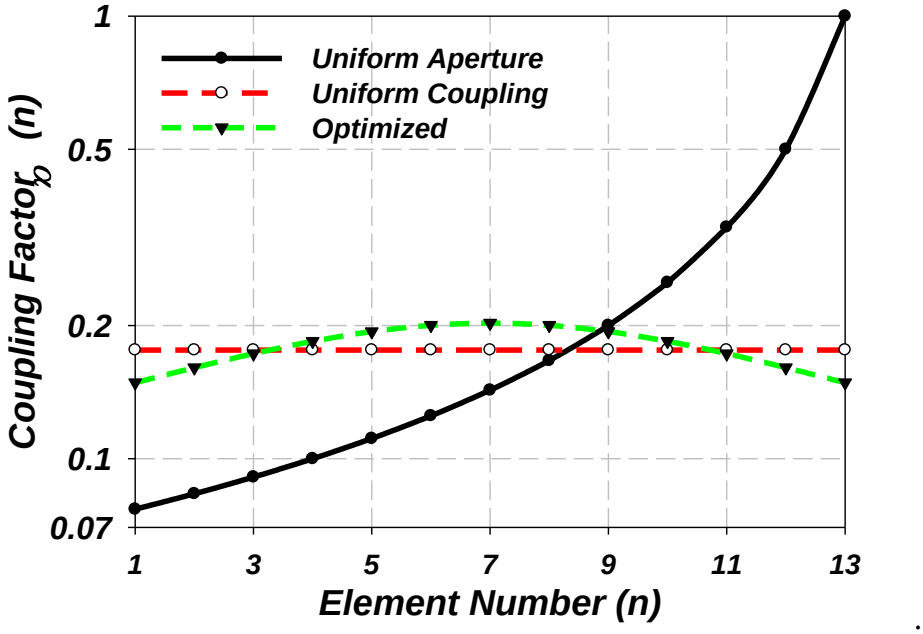

(a)

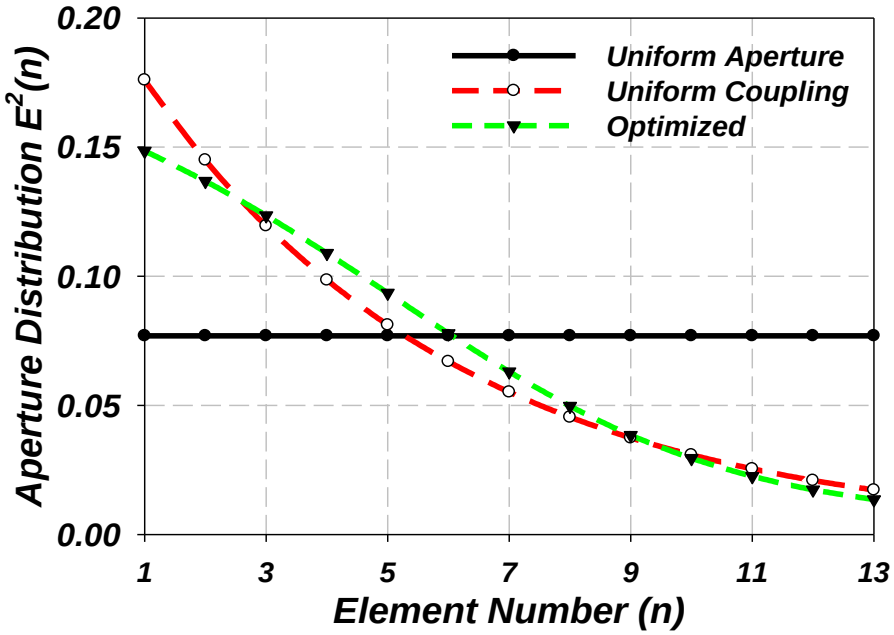

(b)

Figure 3.7 Distribution of (a) Coupling factor (vertical axis in log scale) and (b) Aperture excitation of optimized 13 element travelling wave antenna array.

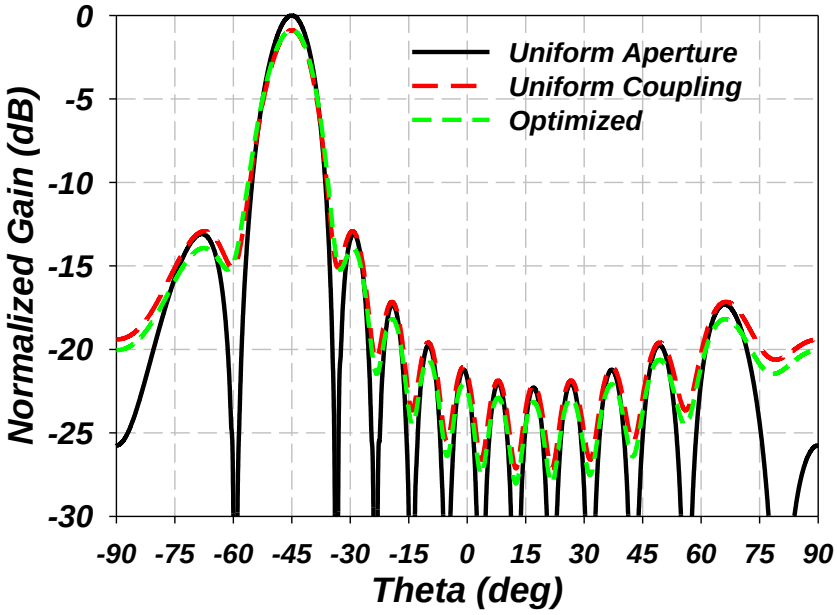

Figure 3.8 Normalized radiation pattern of three different distribution cases

It can also be calculated that the optimized non-uniform distribution gives less than 0.1dB gain improvement over the uniform coupling case and have slightly lower side lobe levels. However, these calculations does not take into account the phase change due to the different coupling factors, which would disturb the periodicity of the array and result in a lower side lobe levels.

In conclusion, the traveling wave array needs to have symmetric radiating elements to give the same performance for both polarizations while feeding from opposite directions. New aperture distribution is analyzed to achieve the maximum gain and efficiency performances under the symmetric conditions. Compared to the traditional uniform aperture distribution approach, which is not practical under the symmetric array conditions, both optimized uniform and non-uniform coupling distributions demonstrates less than 0.9 dB gain drop. The non-uniform coupling distribution offers negligible improvement in gain over its uniform counterpart, but offers reduced side lobe levels. Detailed results will be shown in Chapter 5.

3.2 Single Radiating Waveguide

According to the previous discussions, we can summarize our findings by that the planar antennas are the best low profile choice, yet steering up to 70° would lead to a significant gain drop and performance deterioration. Hence, a low profile, planar, slotted array antenna structure suitable for dual circular polarization for the US market has been developed. Slotted waveguide radiating elements to sustain the high efficiency and travelling wave topology to radiate at off-broadside angles and reduce the elevation steering volume have been utilized. A brief theory of the travelling wave slot array antennas was given in the previous section. In this section, the design of a single radiating slotted rectangular waveguide will be explored.

3.2.1 Steering range

As shown in Figure 3.3, the slotted rectangular waveguide has "X" shaped slots that are densely arranged on the broad wall of the radiating waveguide with a predefined offset from the waveguide center line to control the polarization. This leaky waveguide antenna radiates a circular polarization at the main beam, which already has a tilt angle θ. In order to minimize the mechanical steering requirement in the elevation, θ is selected to be 45º. As a result of this inherent tilt, a maximum of only ±25º mechanical tracking in elevation is required to cover the 20º to 70º DBS elevation observation range as shown in Figure 3.9.

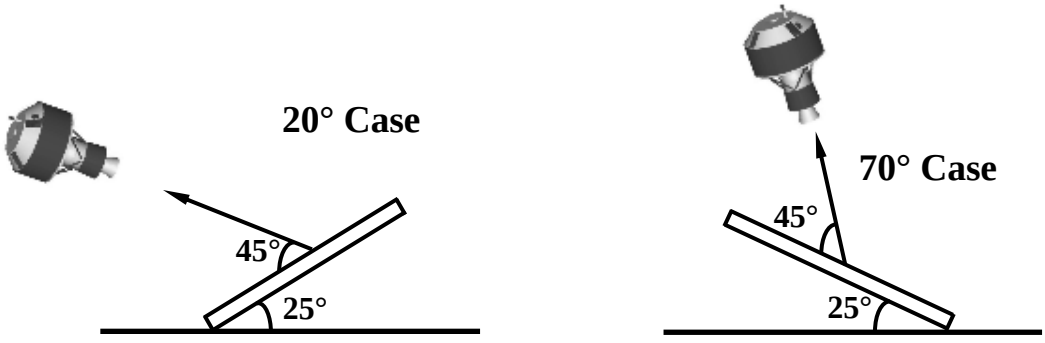

Figure 3.9 Elevation tracking coverage of leaky wave slot array antenna

3.2.2 Single Element Design

The single element is designed using a WR62, a standard waveguide size for Ku band. As can be seen in Figure 3.10, thirteen "X" shaped slots are cut on the top wall, with an offset from the center line S_1 = 3mm and cross angle $\delta = 80°$. These values are optimized from the result of 3.1.1 to accommodating longer slots while maintaining an acceptable circular polarization. As discussed in 3.1.2, the travelling wave slotted waveguide radiates at an angle off broadside that can be primarily controlled by the choice of the radiating waveguide's wide dimension "a". However, the beam tilt angle is also a function of the coupling strength of the slots (e.g. the slot length), the spacing between the "X" shaped slots and frequency. Meanwhile, the efficiency of a symmetric travelling wave slot array is analyzed in 3.1.3, where the gain hits maximum at particular predetermined coupling factors. So the length and spacing of the slots need to be carefully selected to simultaneously achieve the 45° beam tilt angle and maximum antenna gain. Due to the frequency dependence of the beam tilt angle, a fine adjustment for each channel's selection is required — again a drawback in this type of antennas as previously mentioned. The slot length L_2 is the same for each slot, and is designed to be 9.6mm with a slot width S_2 = 1mm, meanwhile the spacing between the two radiating elements is L_1 = 9.3 mm.

3.2.3 Single Element Performance

In addition to approximate equations in section 3.1, the Ansoft HFSS, a 3D full wave EM simulation tool based on finite element method (FEM) has been utilized to optimize the single radiating waveguide element structure. Figure 3.11 shows the prototype built using CNC machine. Thirteen "X" shaped slots were selected to assure better than –10 dB termination loss while adding more slots would increase the overall height of the roof mounted antenna. Also, utilizing less than ten elements would reduce the amount of radiating power and power will be dumped into the waveguide termination; thus the overall antenna efficiency would be significantly degraded.

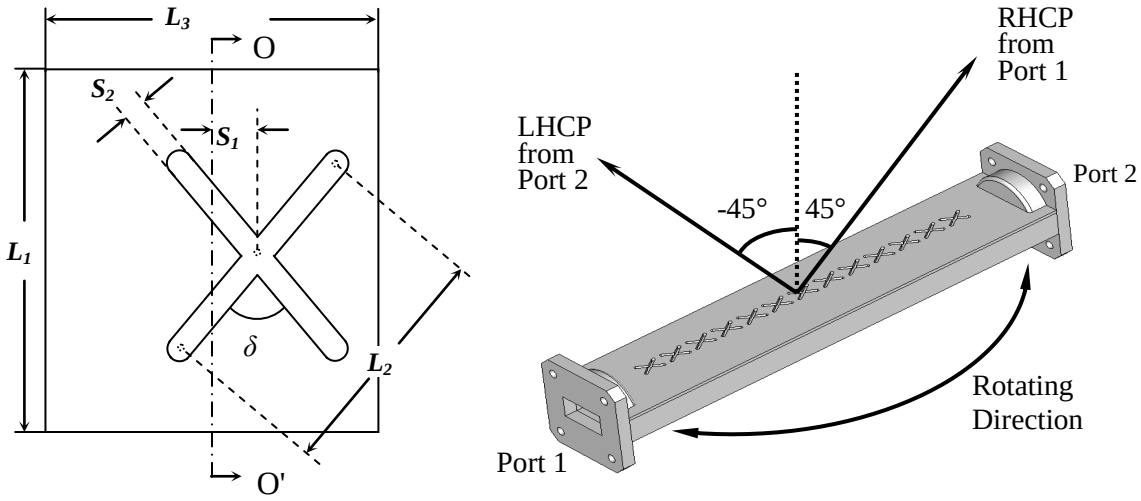

Figure 3.10 A single "X" shaped slot and realization of dual circular polarization

This slot array antenna is measured in the far field and the predicted and measured results are shown in Figure 3.12 and have demonstrated more than 15dB gain and that the sidelobe levels are at least 13dB down. The main beam is located around 45° off-broadside in the elevation direction. Due to the manufacturing limitations, the side of the slotted surface is several mm higher to allow the placement of fastening screws. This metallic "wall" acts as a mirror and causes degraded cross polarization radiation performance at the main beam. It is also noticed that with finite waveguide width, the radiation at the back ($\theta < -90°$ and $\theta > 90°$) is high. This back lobe will shrink as we go from a single element to a 6 element sub-array and eventually the 48 element full array as will be discussed in the following sections, this full array results are shown in Figure 3.12(a). A quarter of the RHCP performance in the elevation is measured and it shows good agreement with the simulated results.

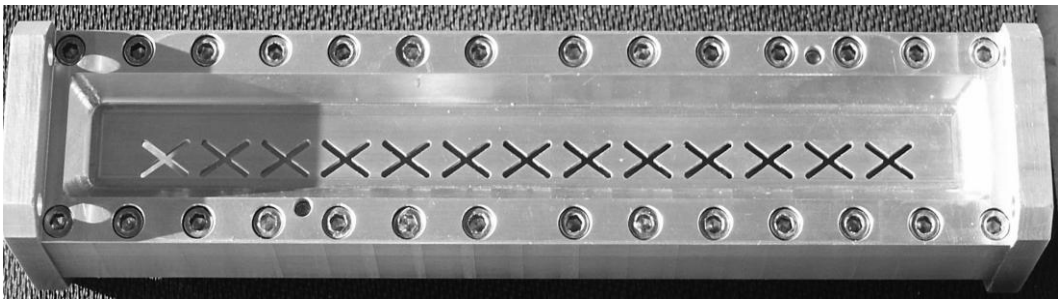

Figure 3.11 Fabricated single radiating slotted waveguide element prototype

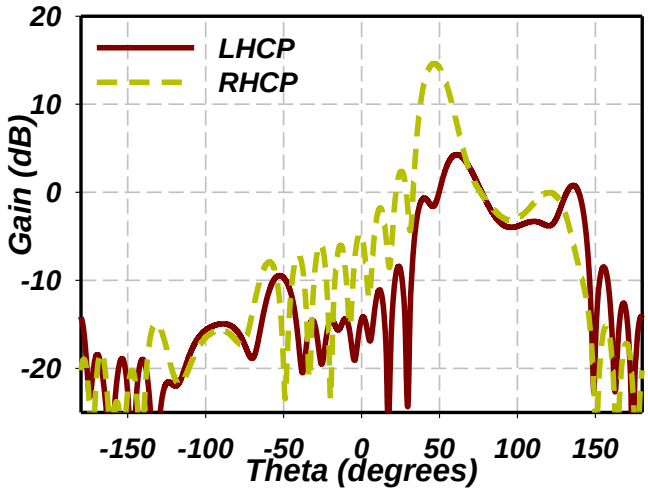

(a) Simulated radiation pattern

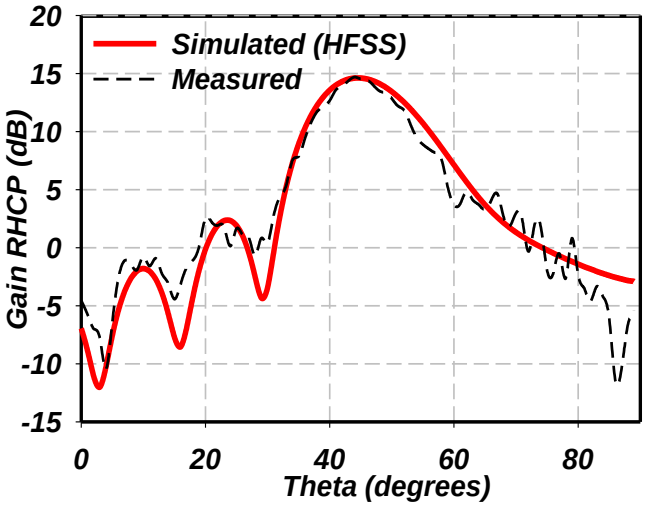

(b) Measured radiation pattern

Figure 3.12 Simulated and measured results of a single element

3.2.4 Sub-array Feed Network Design

In order to maximize the performance of the sub-array design, a feed network that can provide a uniform and in phase power distribution for the radiating waveguides is needed. We developed a 1 to 6 power divider structure, as shown in Figure 3.13, where a 1 to 3 series feed sections are jointed with a 1 to 2 T-Junction power divider. Series feed sections requires the least real estate but are prone to long line effect, where the phase of the divided power does not maintain a good balance over a wide frequency range. T-junctions on the other hand, generates perfect power divisions and phase balance at its outputs but consume lots of real-estate as power can only be combined in a binary manner. This hybrid series parallel feed topology can achieve a relatively good phase balance in a very compact size, which allows more sub-arrays to be added and connected with T-junction power combining stages in the full-array implementation.

On top of the feeding waveguides, each radiating waveguide is fed using center-inclined coupling slots, also shown in Figure 3.13. A short circuit termination is placed a half guided wavelength of the radiating waveguide "$\lambda_{gr}/2$" -- away from the center of the inclined slot. Coupling slots are placed along the centerline of the broad side of both the top of the feeding waveguide and at the bottom of the radiating waveguide. The outmost coupling slots and the radiating waveguides are placed at half guided-wavelength of the feeding waveguide "$\lambda_{gf}/2$" from the short circuit terminations at both ends of the feeding waveguides. A rotation of a specific angle ψ_1 is applied to those slots and optimized to provide approximately a $1/6^{th}$ of the power coupled to the radiating waveguides. The second slot is placed $\lambda_{gf}/2$ from the first slot and is tilted by $-\psi_1$ in order to couple the same amount of power to the radiating waveguides while compensating for the 180° difference introduced by the $\lambda_{gf}/2$ spacing. The inner most coupling slots are inclined by ψ_2 to compensate for the phase change due to the discontinuities in the T-junction. The design of these coupling slots is straightforward as in [13][14], where in our design, ψ_1 = 26°, and ψ_2 = 13° and all coupling slots share the same length of 10.8mm.

The predicted performance of these splitters as a function of frequency are shown in Figure 3.14, where the imbalances are less than 0.5dB in amplitude and 14° in phase. We have utilized HFSS to analyze and predict the performance of these sub-array structures. A sketch of the overall structure is shown in Figure 3.15, and the fabricated sub-array prototype is shown in Figure 3.16 [15]. The fabrication of the prototype using CNC machining is generally very expensive especially for prototyping. Far field radiation pattern measurements were carried out for the co-polarization over half of the elevation plane due to our experimental facility limitations. As shown in Figure 3.17, the measured overall gain of the sub-array exceeds 22 dBi, and the radiated beam is off-broadside by a 45° as predicted [16].

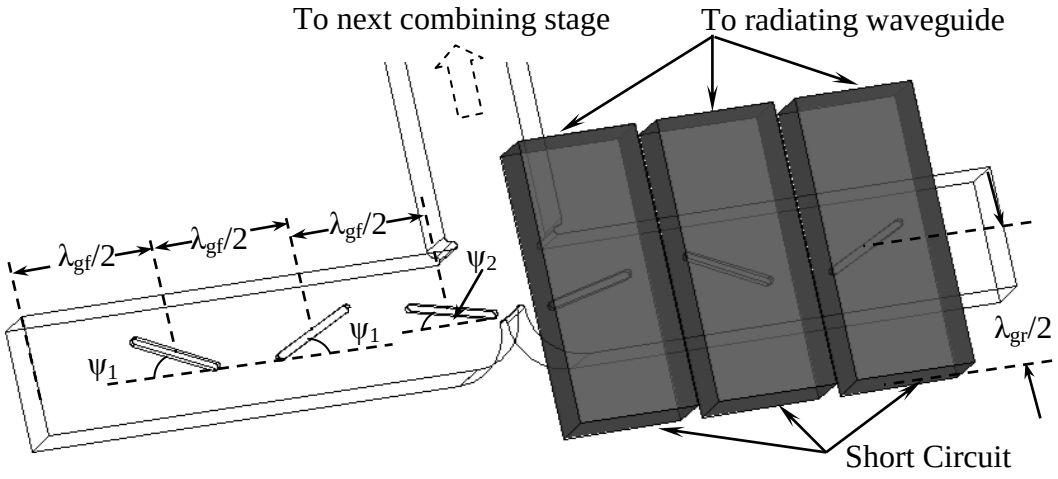

Figure 3.13 Feeding structure of the 6 elements sub-array

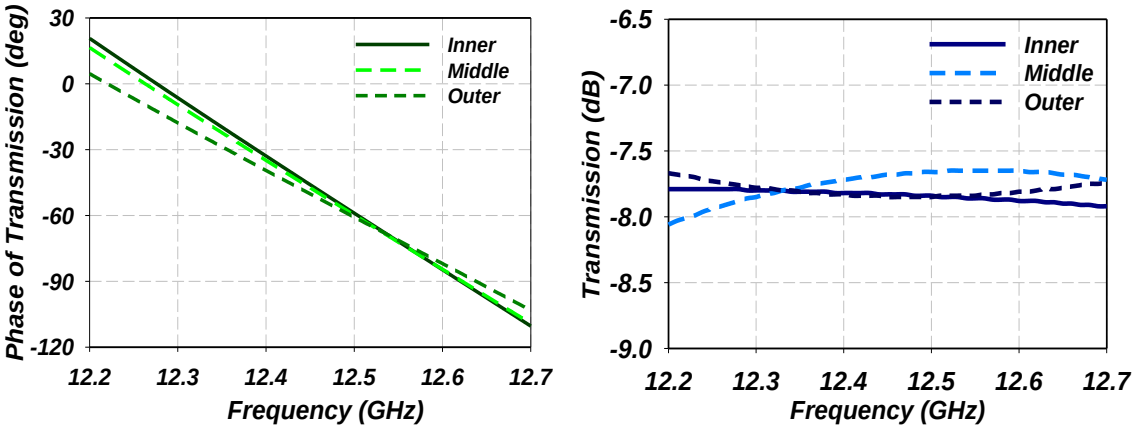

Figure 3.14 Simulated amplitude and phase of 6 equal split outputs

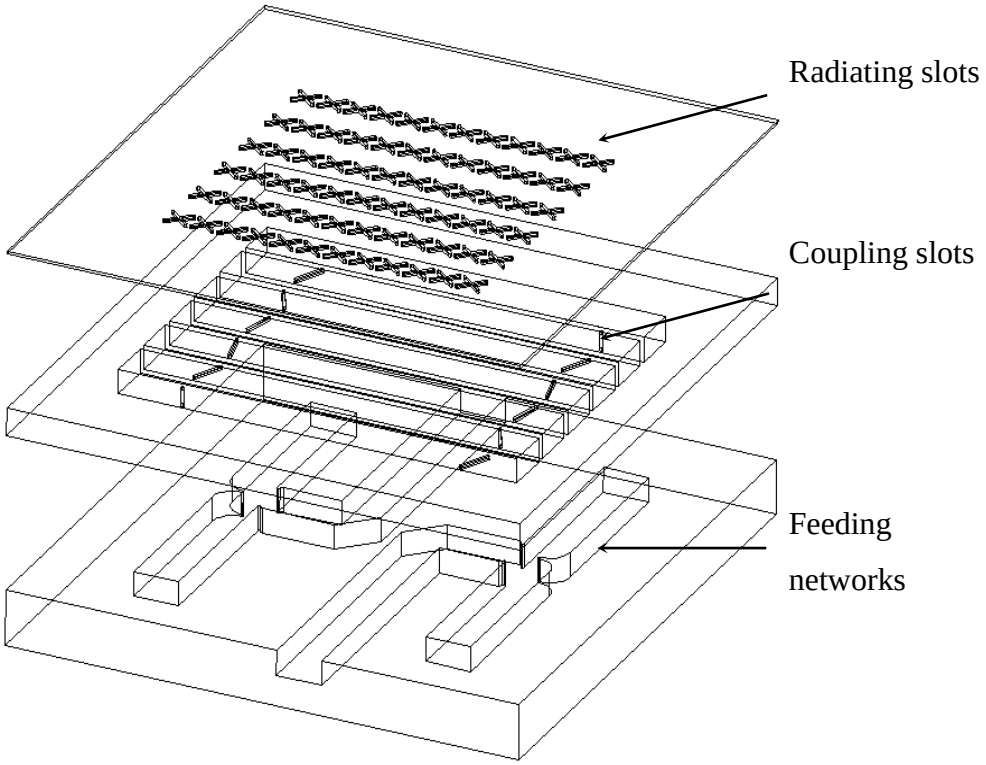

Figure 3.15 6 radiating waveguide sub-array stacks up

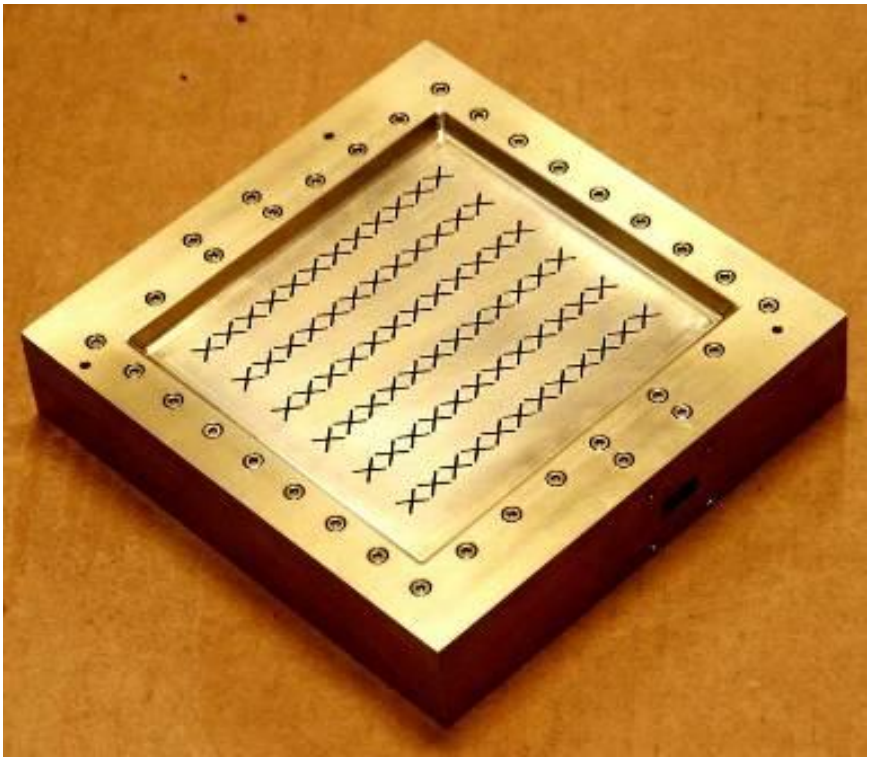

Figure 3.16 Fabricated 6 waveguide sub-array prototype

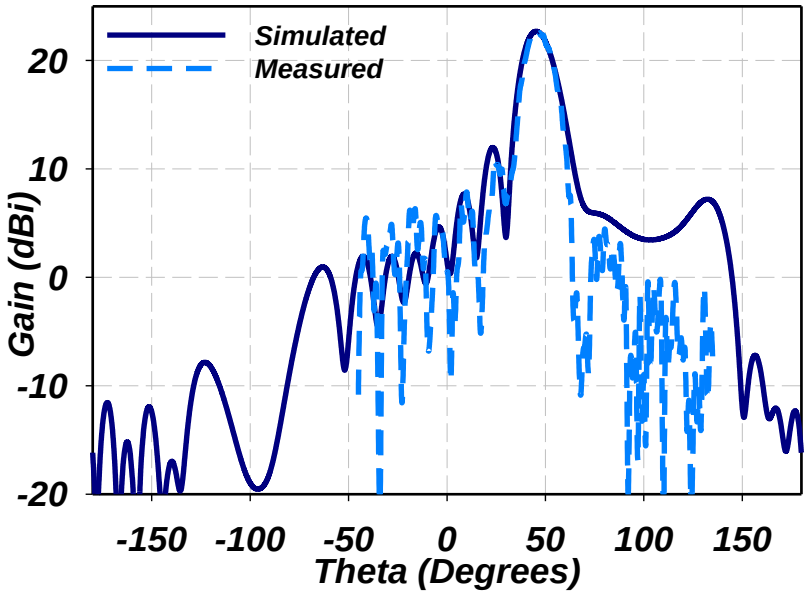

Figure 3.17 Comparison of simulated and measured radiation patterns

3.3 Full Array Design

The gain of the main beam at elevation angle θ of the antenna array can be calculated as:

$$G(\theta) = \eta_f \frac{4\pi A_e}{\lambda^2} \cos\theta \qquad \text{Equation 3-13}$$

Where A_e represents the effective aperture area of the antenna. According to the previous analysis in section 3.1.3, the aperture efficiency of the symmetric travelling wave slot array is about -0.9 dB or 81.3%, the same as the gain drop due to the non-uniform excitation of the aperture. So A_e is 81.3% of the physical surface area of the slot array. The cost factor takes into account the projection of the antenna aperture when the main beam is off-broadside. η_f is the efficiency of the feed network and it is a function of the number of radiating elements in the array. Since, for rectangular waveguide feed network, the loss of the feed network is mainly due to the ohmic loss of the waveguide, it nearly doubles every time the number of radiating waveguide is doubled, assuming a binary feed network is used above the sub-array level.

The maximum achievable gain based on the radiating waveguide and sub-array structures is shown in Figure 3.18, as a function of the unit ohmic losses of the feeding waveguide and the number of the radiating slots. It can be seen from the figure that as the unit loss of the feed network increases, the gain improvement upon adding more radiating elements becomes less and less. So the loss factors must be significantly reduced to justify the expansion of the array size. In our case, ohmic loss of brass, from which the sub-array is made from, is about 0.01dB/inch. So, in order to achieve over 32 dB gain, 48 radiating waveguides are needed, which amounts to using 8 sub-arrays.

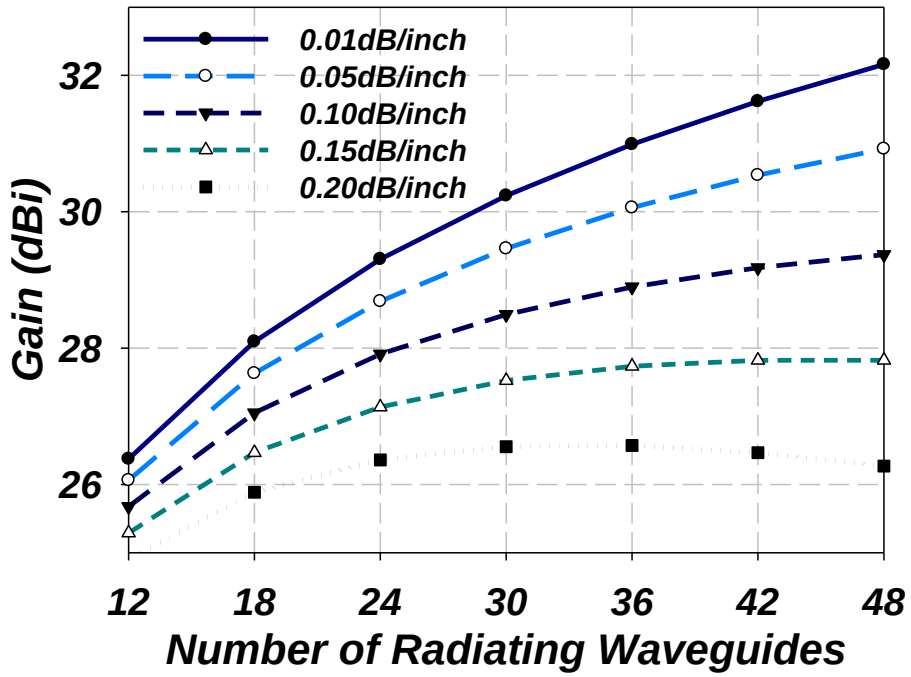

Figure 3.18 Gain of array with various radiating waveguides and feed waveguide losses

Drawings of the full array design is shown Figure 3.19, where 8 sub-arrays are combined on the back of the radiating waveguides with a 3-stage T-junction binary combining network (i.e. 1: 8 power splitters). The design of both equal and unequal power split rectangular waveguide T-junctions are very crucial in building the overall feed network. Their design is based on utilizing inductive windows and wedges. The details of their design are discussed in [17]. The overall dimensions of the structure are a height of 0.8 inch, a length of 31 inch, and a width of 7.1inches.

The structure is designed to be mounted at its centerline, which is elevated a 1.5 inch off the bottom of the whole antenna. Its maximum movement will not exceed a vertical distance of 3inches as shown in Figure 3.20.

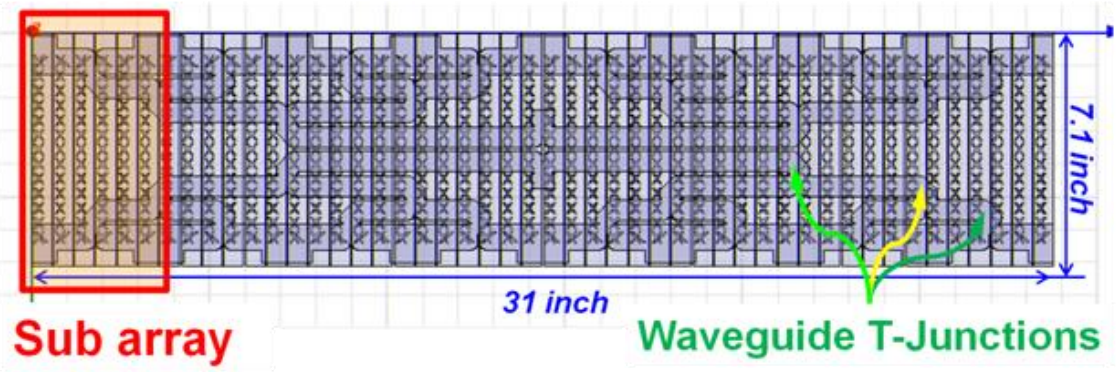

Figure 3.19 Drawing of a 48 radiating waveguide full array

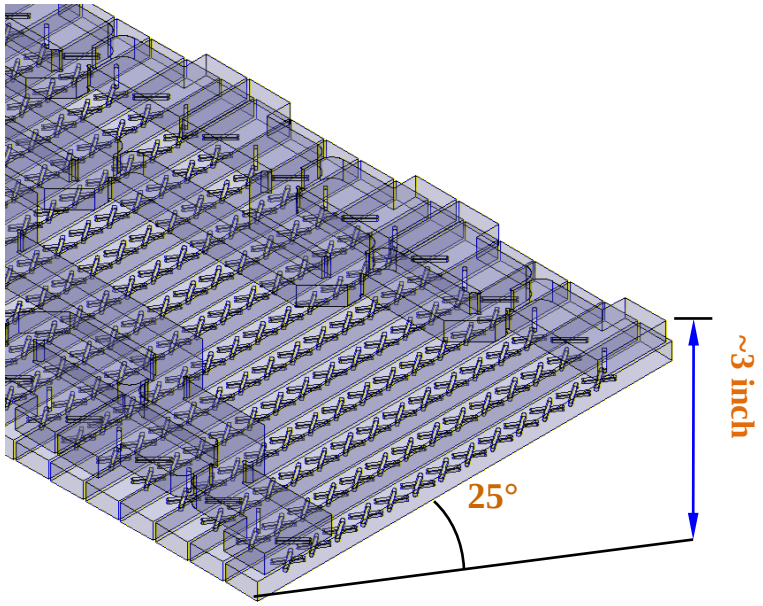

Figure 3.20 Antenna's height at maximum scan angle

A Pro-E drawing of the overall antenna structure is shown in Figure 3.21, and it requires three metal layers to construct the slot array antenna. The feed network, consisting of 4 stages of binary and one stage of series power splitter, and it is designed to be on the bottom metal layer as shown on the left. In the middle layer, reside all the 48 radiating waveguides with coupling slots on their bottom wall to transfer power to the feed network. The top layer is a sheet of metal with 48 columns and 13 rows of "X" shaped crossed slots cuts on the top surface.

After all, the full array was not fabricated due to its prohibitive prototyping cost -- as it requires high accuracy CNC machining. The weight is another problem that stopped us from its materialization, as a heavy antenna will slow the tracking of satellite. An alternative technology is required to achieve the same functionalities of the metallic waveguide while sustaining the low loss characteristics of waveguides, with a much lower manufacturing cost and a much lighter weight. The solution is the substrate integrated waveguide structures "SIW" technology, which will be discussed in the next chapter.

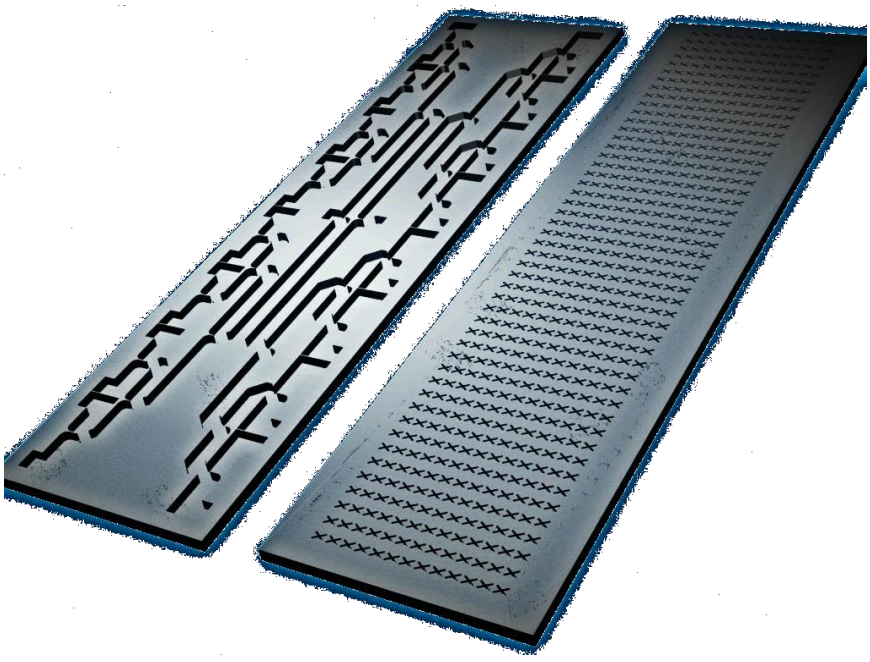

Figure 3.21 Pro-E drawing of the full array design.

3.4 Conclusions

Travelling wave slotted waveguide array antennas are excellent low cost alternatives to planar phased arrays. Mechanical steering in both the azimuth and elevation planes is acceptable and is considered here in order to develop a low profile structure. A fully mechanical steering slotted waveguide array structure, which has the main beam radiation with an inherent tilt angle of 45° has been proposed. This feature is used to limit the required scanning range to ±25°, which results in a low profile design. "X" shaped crossed slots are closely arranged along the broad side of the rectangular waveguide to achieve one type of circular polarized radiation by feeding from one port/side of the waveguide and the other type by feeding from the opposite port/side. The location of the slots to achieve good CP, proper slot dimensions and spacing to achieve certain beam tilt angle, and the optimum tapering of the slots to achieve maximum aperture efficiency under symmetric array environment are all analyzed. Additionally, the utilization of a waveguide feed structure is crucial here in sustaining high efficiency. A single radiating waveguide and a 6 radiating waveguide sub-arrays has been fabricated and measured and demonstrated good performance. A full array consisting of 48 radiating waveguides is designed but not fabricated due to the high cost of CNC machining/prototyping and its weight. A light weight alternative structure with a low fabrication cost is required for the realization of the full array, which will be introduced in the following chapter.

Chapter 4

Substrate Integrated Waveguide (SIW) Technology & Feed Network Design

As discussed in Chapter 3, a slotted waveguide array comprised of 6 radiating waveguides has been designed and prototyped. The prototype is fabricated using CNC machining and their measured results were very encouraging. However, the design implementation was hindered by the prohibiting cost of its manufacturing, as well as its heavy weight, i.e. not suitable for consumer type applications. Recently, the substrate integrated waveguide (SIW) technology has been introduced as a low cost solution for mm-wave systems [18], where waveguide components can be fabricated using standard PCB processes on dielectric substrates. However, the techniques can be also suitable for antenna array developments at microwave frequencies.

In this section, the propagation and attenuation characteristics of the substrate integrated waveguide are discussed. Additionally, the antenna array feed network components designed using SIW structures are studied in detail. In section 4.1, the relationship between SIW and regular dielectric filled rectangular waveguides will be studied to simplify the evaluation of the propagation constant and loss factor coefficients . In section 4.2, waveguide junctions for antenna feeding networks, such as the T- and Y-

junctions will be developed using our newly developed generalized SIW design equations/graphs. In section 4.3, the transitions from SIW to planar circuits and between SIWs placed on the different layers of the structure stack are studied, followed by the conclusion of this chapter in section 4.4.

4.1 Substrate Integrated Waveguides

Conventionally, metallic rectangular waveguides are utilized to fabricate both the slotted array antennas and their associated feed networks for their extremely low loss performance. However, they are bulky, heavy, and expensive to fabricate. Hence for consumer type applications, a lower cost alternative technology -- Substrate Integrated Waveguides (SIWs) structures fabricated on printed circuit boards are proposed here. Where SIW sidewalls are constructed from lined via holes, as shown in Figure 4.1, rather than solid fences. This technology is simple to fabricate, less expensive, and renders light structures.

In an effort to extend the design guidelines of the metallic rectangular waveguide travelling wave slot arrays developed in Chapter 3 to SIW designs, extensive full parametric study of the SIW structures was carried out. The study is based on a 3D full wave analysis using Ansoft HFSS to develop an equivalent conventional dielectric loaded rectangular waveguide to represent the SIW structure. The developed equivalent structure can then be used to estimate the complex propagation characteristics of the SIW guides using the known rectangular waveguide expressions. Design charts have been developed here, and will be a great asset in significantly facilitating the selection of the substrate dielectric material, as well as the SIW dimensions in the system level feed network design step. These equivalence relationships will also allow the seamless transfer of the radiating waveguide analysis results in Chapter 3 to the development of a travelling wave slotted SIW array, as will be introduced in Chapter 5.

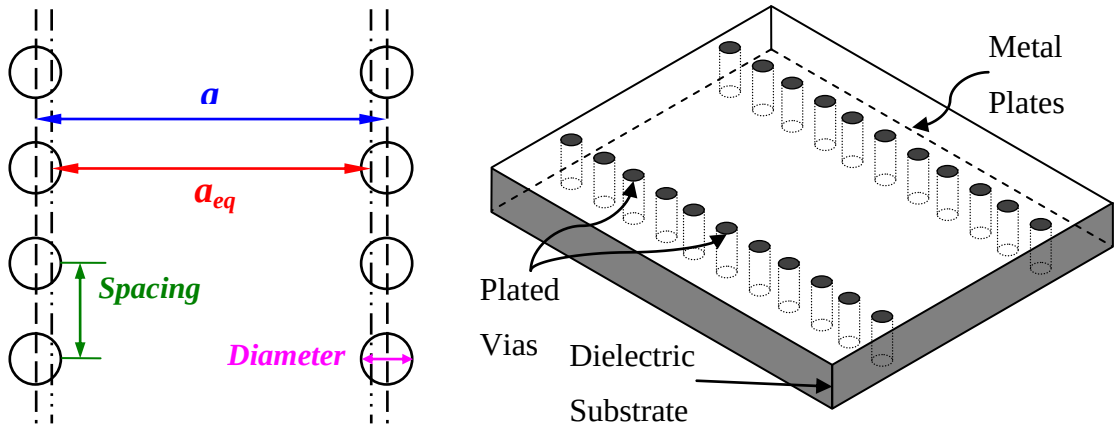

(a) Top view (b) 3D view

Figure 4.1 Substrate integrated waveguide defined on dielectric substrates.

4.1.1 Equivalent Waveguide Width "a_{eq}"

In order to develop an equivalent width "a_{eq}" for the SIW width dimension, as a function of the diameter and spacing of the vias, an extensive 3D EM simulation has been carried out, where the top and bottom walls, and the lined vias are assumed to be perfect electric conductors. In addition, absorbing boundary conditions have been applied along the SIW walls to allow energy to leak through the gaps between the lined vias, i.e. posts. The dielectric in this step, is assumed to be lossless, and has ε_r = 2.2 throughout this simulation step as most of the commercially available low loss dielectric substrate materials have dielectric constants close to that value. The waveguide "a" dimension is selected in our design to be 13.5 mm, such that at the center frequency of our operating band, that is 12.45 GHz, the SIW is under single waveguide mode operation. Meanwhile, a thickness of 3.175 mm has been used to ensure only the TE_{10} mode is allowed to propagate.

The propagation constant of each diameter/spacing combination of these posts are numerically estimated based on HFSS simulation. Where the phase of the scattering matrix was extracted and compared to that of the regular dielectric loaded rectangular

waveguide, given that the propagation constant of the rectangular waveguide filled with dielectric is calculated based on the well known closed form expression:

$$\beta_z = \beta\sqrt{1-\left(\frac{\lambda}{2a}\right)^2} = \frac{2\pi}{\lambda}\sqrt{1-\left(\frac{\lambda}{2a}\right)^2} \qquad \text{Equation 4-1}$$

Where $\lambda = \lambda_0/\sqrt{\varepsilon_r}$ and λ_0 is the wavelength in free space.

The extracted equivalent waveguide width "a_{eq}" is plotted as shown in Figure 4.2 as function of the posts diameters and spacings. Based on these previous simulations, the equivalent waveguide "a_{eq}" dimension is smaller than the actual lateral spacing of the posts "a" due to their reactive loading. However, the effective/equivalent "a" value tends to increase whenever thinner or widely spaced posts are used. But, the wider the spacing between the posts, the higher the leakage loss is, as will be indicated in the next Section. For high loss cases, the SIW can then be no longer suitable for building the feed network for the antenna arrays.

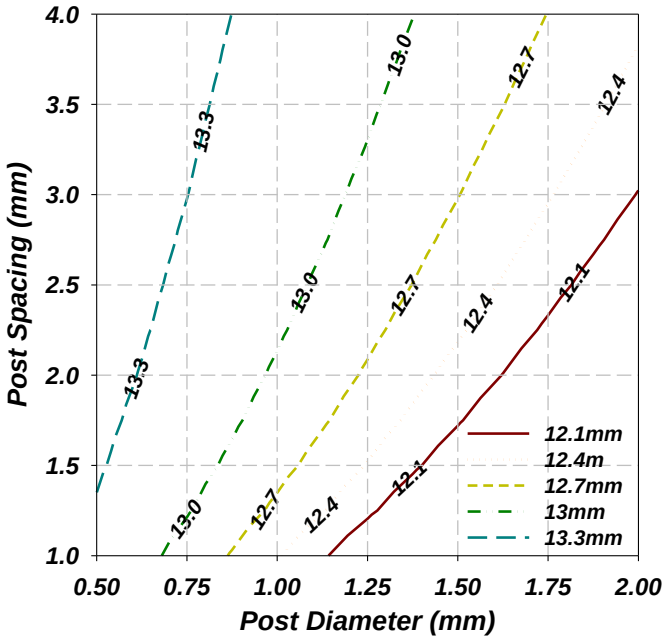

Figure 4.2 Equivalent waveguide "a_{eq}" dimensions of SIW with different post parameters

Approximate design equations of the equivalent dielectric filled waveguide "a_{eq}" as a function of the post diameter and spacing can also be generalized as described in [19] basked on curve fitting:

$$a_{eq} = a - 1.08 \cdot \frac{diameter^2}{spacing} + 0.1 \cdot \frac{diameter^2}{a} \qquad \text{Equation 4-2}$$

4.1.2 Leakage Loss

The side walls of the SIW structure can be represented by a lossy reactive load, obviously the losses are due to the leakage through the openings between the posts. This leakage loss "$L_{leakage}$" together with the dielectric "$L_{dielectric}$", and the conductor's loss "$L_{conductor}$" contribute to the total attenuation of the SIW feeding structure. To estimate the leakage coefficient, the transmitted power of a lossless SIW structure is calculated, the attenuation of which is then solely related to its leakage loss. A contour map has been generated as a function of the post parameters as shown in Figure 4.3

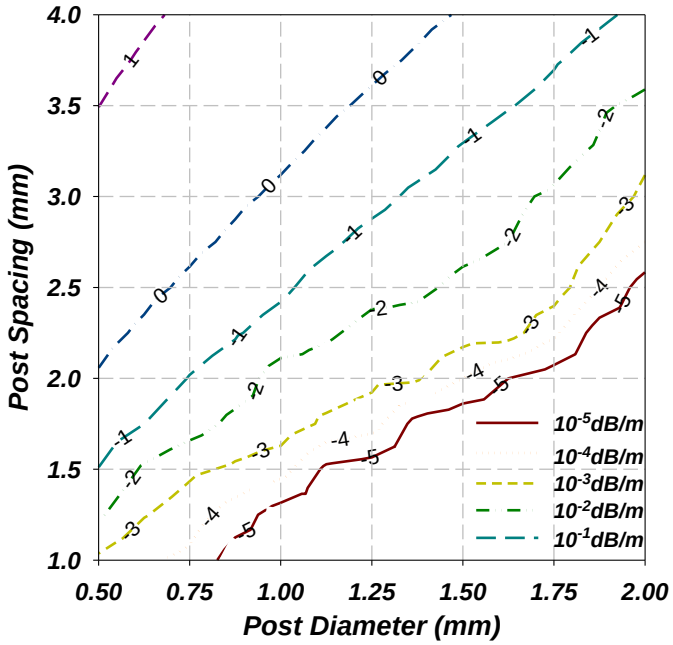

Figure 4.3 Contour plot of the unit leakage loss of the SIW in logarithmic scale

It is important here to recognize that when the post spacing is moderately large, the leakage effects are rather high and could be unacceptable. On the other hand, it is not practical to massively load the SIW structure with closely-spaced vias to eliminate leakage. However, a compromise between lowering the loss and lowering the fabrication cost can be achieved. In most cases, the leakage loss can be easily reduced several folds by reducing the spacing between the posts. Also, it is not a dominant loss contributor, if well controlled, it can even be neglected in most cases. Results of Figure 4.3 can also be normalized to "a_{eq}" as shown in [20] to be used for more general SIW parameters combinations.

4.1.3 Dielectric Loss

To estimate the SIW dielectric loss, the well known dielectric loss formulas of a dielectric filled rectangular waveguide in association with the equivalent width "a_{eq}" have been utilized. The losses are given by [8]:

$$L_{dielectric} \cong \frac{\varepsilon''}{\varepsilon'}\frac{\pi}{\lambda^2}\frac{\lambda}{\sqrt{1-\left(f_c/f\right)^2}} = \tan\delta\frac{\pi}{\lambda}\left(\frac{\lambda_g}{\lambda}\right) \text{ Np/m} \qquad \text{Equation 4-3}$$

Where ε' and ε'' are the real and imaginary parts of the complex dielectric constant of the lossy dielectric loading, λ and λ_g are the wavelength and guided-wavelength in a dielectric media and tan δ represents the dielectric loss tangent. A contour plot has been generated for the dielectric loss for a set of different materials and shown in Figure 4.4(a). The same structure has been simulated using HFSS too, and the extracted results are shown in Figure 4.4(b). These results validate our assumptions of using Equation 4-3 to predict the SIW dielectric losses. This experimental validation further proves that it is an excellent approximation to evaluate the dielectric loss of a SIW by the dielectric loss of a rectangular waveguide that is filled by the same dielectric.

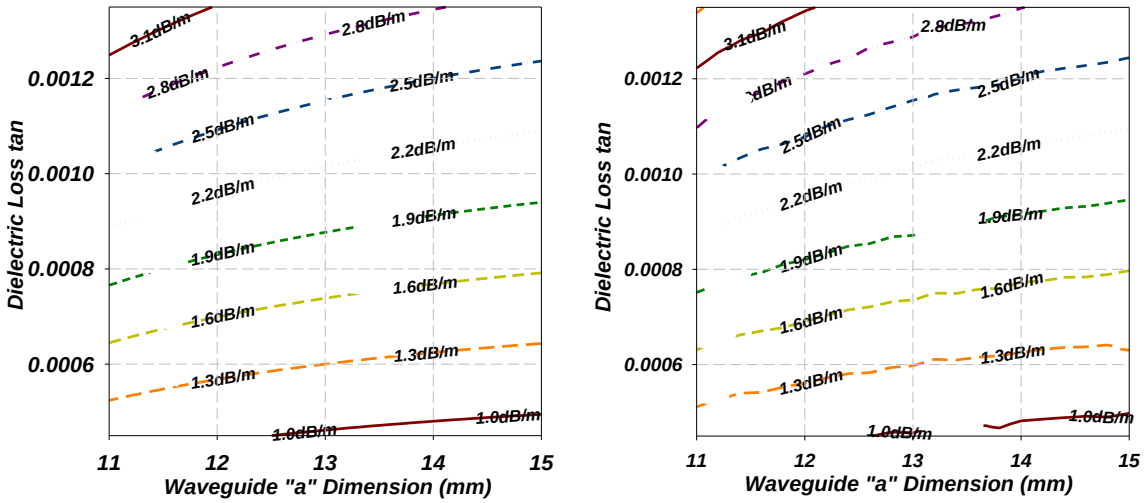

(a) Calculated from Equation 4-3 (b) HFSS simulation results

Figure 4.4 Contour of dielectric loss as a function of dielectric loss tangent and the waveguide "a" dimensions.

For high performance antennas, the selection of the dielectric material is extremely important step when designing large arrays. The dielectric loss could be relatively high even for a substrate with a very low loss tangent. Hence, it is recognized that for regular high frequency laminate materials (tan $\delta \sim 0.0009$ and up), the dielectric losses can be prohibitively large if the antenna array contains many radiating elements. As shown in Figure 3.18, for lossy feed lines, increasing the number of the radiating elements may not produce higher gain.

4.1.4 Conductor Loss

Similar to the dielectric loss, the conductor loss can also be approximately evaluated using the rectangular waveguide equations after accounting for sidewalls extra loss, given that they are made of plated via-holes. In addition, the surface roughness of the plated metal layers degrades the conductivity of the equivalent waveguide walls. The conduction loss of the TE_{10} wave propagating in a single mode rectangular waveguide is given by [8]:

$$L_{conductor} = L_{sidewalls} + L_{top\&bottom} = \frac{2R_{s1}}{\eta a}\frac{\left(f_c/f\right)^2}{\sqrt{1-\left(f_c/f\right)^2}} + \frac{R_{s2}}{\eta b}\frac{1}{\sqrt{1-\left(f_c/f\right)^2}} \text{ (Np/m)} \quad \text{Equation 4-4}$$

$$R_s = \Re\left\{\sqrt{\frac{j\omega\mu}{\sigma + j\omega\varepsilon}}\right\} \cong \sqrt{\frac{\omega\mu}{2\sigma}} \text{ (Ohm) and } \eta = \sqrt{\mu_0/\varepsilon_0\,\varepsilon_r}\,, \quad \text{Equation 4-5}$$

Where R_{s1} and R_{s2} represent the real part of the complex surface impedances of the sidewalls and top/bottom conductors respectively, which can be approximated by Equation 4-5. From these equations, it can be seen that the conductor losses are function of the physical dimensions of the waveguide, and the conduction losses contributed by sidewalls are independent of the substrate thickness. A set of loss curves per unit length at 12.45GHz is plotted below in Figure 4.5 that are based on Equations 4-4 & 4-5, where a lossless dielectric with $\varepsilon_r = 2.2$ is used and the waveguide "b" dimensions are selected to be one of the standard PCB board thicknesses, also, the conductivity of metal is that of copper will be assumed here for all the conductive surfaces at this step, it is expected that measured conductor losses will be higher due to the use of a copper coated commercial substrates with lower metal conductivity values and their surface roughness effects too should be accounted for.

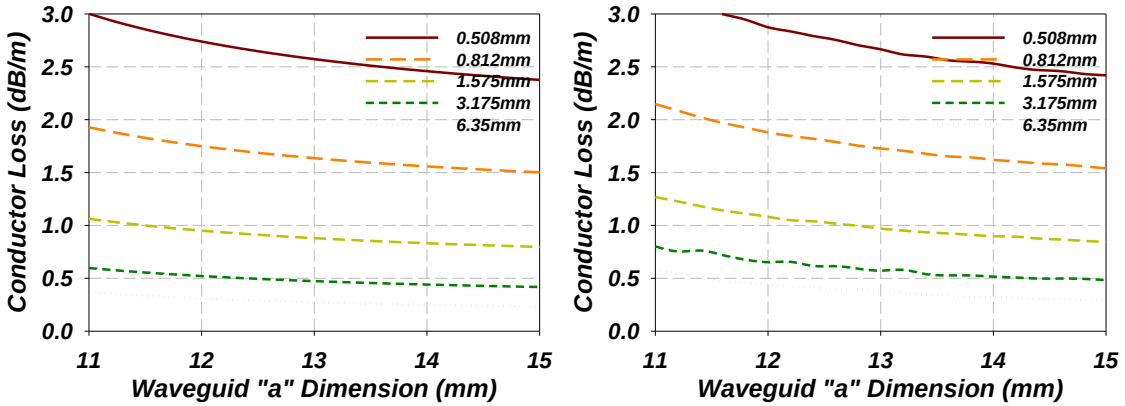

(a) Calculated using Equation 4-4 (b) Simulated results.

Figure 4.5 Conductor loss for various substrate thickness and waveguide "a" dimensions

As can be seen from the plots, the conductor loss cannot be neglected. It is quite comparable to the dielectric loss, even for the case when using large "a" and "b" dimensions. Significant conductor loss reduction, however, can be achieved upon using thicker substrates, as indicated from the second term of Equation 4-4's dependence on the substrate height "b". Moreover, it is obvious that there are some differences between the HFSS simulated results and the calculated closed-form expressions results. I believe the differences are due to the extra sidewall losses of the SIW structure. And the conductor loss of the SIW can only be approximately estimated by the dielectric filled rectangular waveguide formula with the SIW's "a_{eq}" substituted for the waveguide dimension a.

4.1.5 Design Parameters Selection and Overall Loss Prediction

According to the previous loss analysis of the SIW, the minimum insertion loss of the antenna array feed network can be achieved upon using thick low loss dielectric loss substrates. In addition, the leakage loss can be reduced by several orders of magnitude smaller than the dielectric and conductor losses by carefully selecting the spacing and diameter of the posts, e.g. close to 0.01dB/m line as shown in Figure 4.3. Extensive use of posts to the point that the spacing between the posts is less than twice of the post's diameter should be avoided too to minimize overall fabrication costs.

In our design, dielectrics with ε_r ~ 2.2 and a thickness of 125mil (the maximum available standard thickness is 3.175mm = 125mil) is used to provide ~ a 0.6dB/m conductor loss for a SIW structure with an equivalent width of 12.8mm. The dielectric loss tangent is presumed to be less than tan δ= 0.001, which still accounts for about a 2.0dB/m dielectric loss (which is quite significant). The posts diameter is selected to be 1.25mm and the spacing is twice the post diameter to avoid "overloading" the substrate with plated vias. According to these dimensions, a leakage loss factor of around 0.01dB/m is predicted, which is insignificant, when compared to either the conductor or the dielectric losses. Based on Figure 4.5, the overall loss is estimated to be in the range of 2.4 to 3dB/m, which is a function of the "a" dimension.

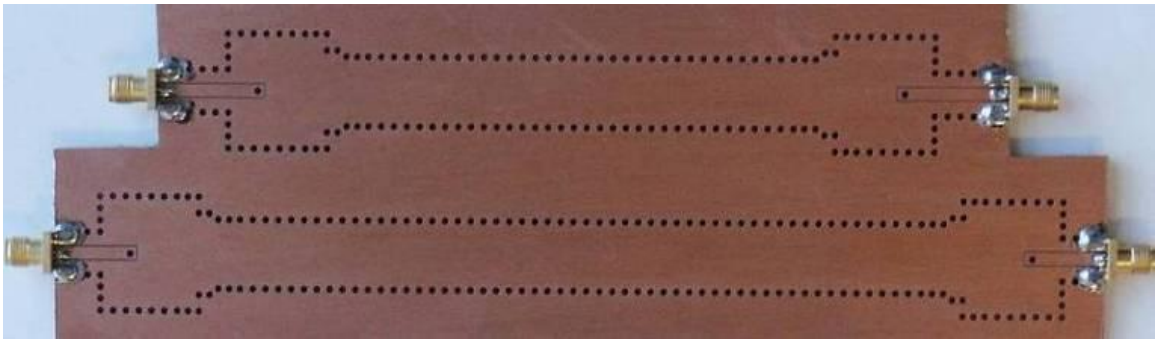

Figure 4.6 Back to back transitions with different lengths for insertion loss measurement.

4.1.6 Experimental Results

In order to experimentally evaluate the overall insertion loss per unit length of the SIW and verify the previous simulated results, two test fixtures were fabricated using a 125mil thick Rogers RT Duroid 5880 material with ε_r = 2.2 and a dielectric loss tangent of 0.0009. As shown below in Figure 4.6, the "a" dimension of these two SIWs is 13.5mm and they are designed to have 2 inches difference in lengths. Back-to-back measurements were carried out to measure the differential insertion loss in dBs between the two test fixtures and their results are shown in Figure 4.7. Based on these measurements, it is estimated that the loss of the SIW is 0.07dB/in, which translates to a 2.75dB/m. The measured losses are higher than predicted based on the actual copper conductivity. A fudge factor might be used in our metal loss calculations to account for the lower plated metal surface conductivity of the vias.

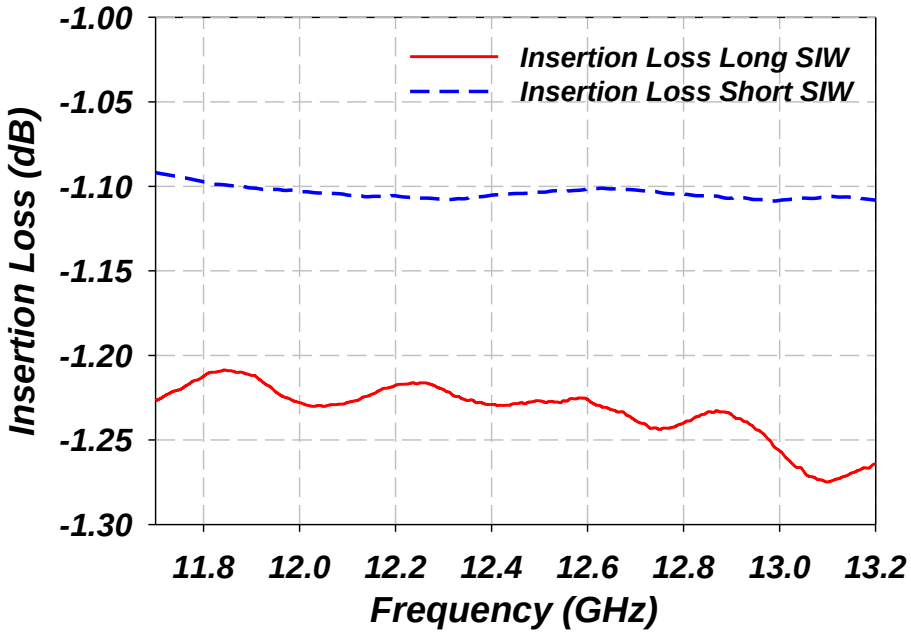

Figure 4.7 Measured insertion losses of two SIW lines with 2 inch difference in length

4.2 SIW Feed Network Components

The basic building blocks to construct a slotted SIW feed network include:

- Substrate integrated waveguides with low loss to construct the feed network.
- Binary feed network based on SIW T and Y-junctions to achieve adequate bandwidth and good phase balance at the inputs of all the radiating waveguides.
- Modified SIW junctions for compact feed network development
- Transition between two layers of SIW, i.e. the radiating SIW layer and the feed SIW layer, to allow compact multi-layer slot array design.
- Smooth coaxial line to SIW transition through a grounded CPW at the antenna input.

In the following sections, each block and its associated design/synthesis procedure will be discussed in details.

4.2.1 Synthesis of the SIW T-Junctions

Waveguide T-junctions are key components for the antenna array feed network construction. Feed network can be either a serial or a parallel network. Parallel feed (i.e. the binary feed) generally requires more stages, hence more real estate. But it would achieve the widest bandwidth for in-phase excitation.

Extensive studies have already been carried out to develop different T-junctions power dividers in metallic waveguides [21]. These designs have included a post placed inside the junction, as shown in Figure 4.8(a), to enhance the operating bandwidth. However, the manufacturing of such isolated posts inside the junction is a major difficulty for mass production, especially when the design contains sensitive dimensions. Alternatively, a synthesis procedure for waveguide T-junctions power divider to achieve arbitrary power split ratio, while keeping a balanced phase between the output ports has been developed [17]. In our design, a wedge and diaphragms have been placed inside the junction and the input ports respectively, as shown in Figure 4.8(b). Neither the wedge nor the diaphragms are separated from the junction body (i.e. full height posts), so it is relatively easier process to fabricate these structures especially when casting is used. SIWs are defined by vias on the dielectric substrate, hence, there is no additional difficulty to introduce a matching post in the junction, as long as, and it is the same size like the vias. So, according to the equivalent concept developed in section 4.1, Our previous T-junction designs for metallic waveguides have been extended to the SIW after replacing the wedge by posts with the same diameter. This new equivalent structure renders a T-junction structure that is suitable for the SIW fabrication.

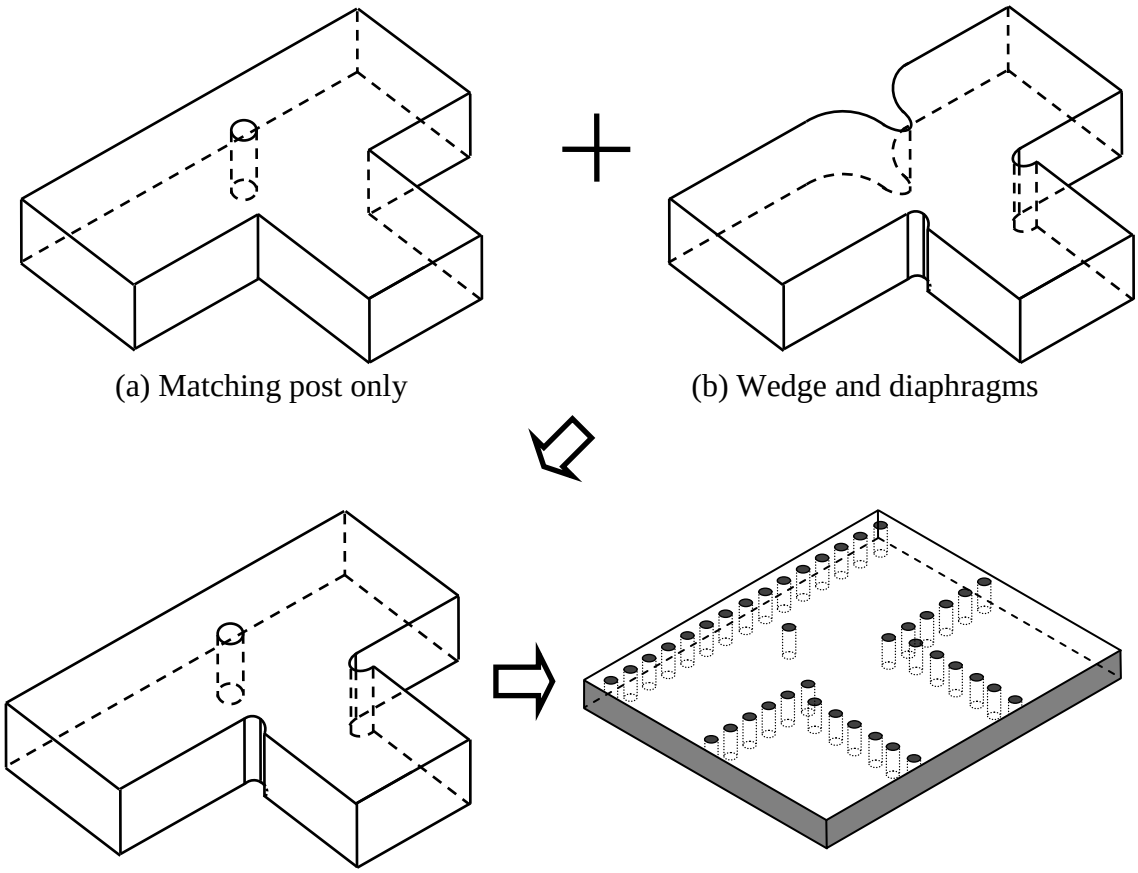

(a) Matching post only (b) Wedge and diaphragms

(c) Combination (d) SIW version of the combined

Figure 4.8 Waveguide and SIW T-junctions with various matching components

In addition, a set of design charts for the SIW T-junction design parameters based on extensive HFSS simulations have been developed. This set of curves can be used to design the post-diaphragm configuration of SIW T-Junctions. As shown in Figure 4.9, both the L_p (distance of the post in the junction from the common sidewall of two outputs) and the L_d (indent of the vias forming the diaphragms from the sidewalls of the input SIW) have been optimized to achieve a perfect match at our design center frequency of 12.45GHz. Design curves for unequal power split are also generalized in [20], where all dimensions are normalized, such that it can be used for any SIW dimensions.

4.2.2 Synthesis of the SIW Y-Junctions

The previous analysis has been extended here to include a special case of the T-junction -- the Y-junction. This Y-junction is usually used at the input of the binary feed network. In a similar fashion, the Y-junction can also be compensated by introducing the diaphragms and the offset of the common sidewalls of the two outputs as shown in Figure 4.10. Following the same method described in the previous section, a set of design curves, as shown in Figure 4.11, have been generated for the SIW Y-junction design for our design frequency with the selected SIW material.

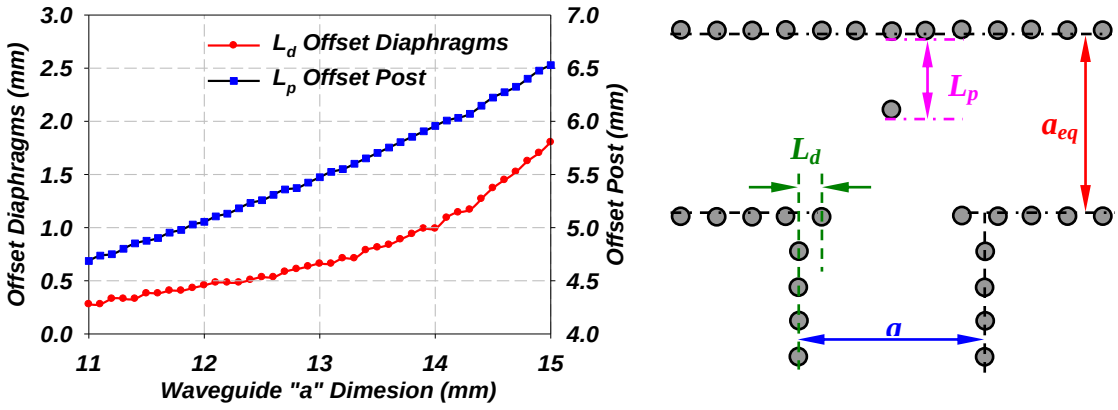

(a) (b)

Figure 4.9 Design charts (a) and parameters (b) of the post-diaphragms SIW T-junction

4.2.3 SIW Feed Network Design

For a SIW feed network with the selected dielectric material, substrate thickness and other parameters in section 4.1.5, the feed guide "a" dimension needs to be designed to minimize its insertion loss. Obviously, increasing the "a" dimension would lead to further conductor loss reduction, however this dimension is limited by the maximum allowed space of the feed network. In addition, the developed designs for both the T and Y-junctions should cover at least 500 MHz, i.e. the DBS bandwidth in USA.

As shown in Figure 4.12, the simulated bandwidth (for return loss < -30dB) of both the Matched SIW T and Y junctions are functions of the waveguide "a" dimension, and both structures provide a fairly wide operating bandwidth. It was noticed too that when the SIW is narrow, the bandwidth peaks at 13% and 10% for the T- and the Y-junctions respectively. Along the increase of diaphragms offsets, the quality factor of these junctions becomes higher and higher, so the bandwidth continues to get narrower as the width of the SIW increases. However, for both junctions, it is easy to achieve a 500MHz bandwidth at 12.45GHz (~4% bandwidth). Therefore, in order to sufficiently minimize the feed network loss, the "a" dimensions of the different sections of the SIWs in the feeding network can be maximized given that the bandwidth requirement is satisfied.

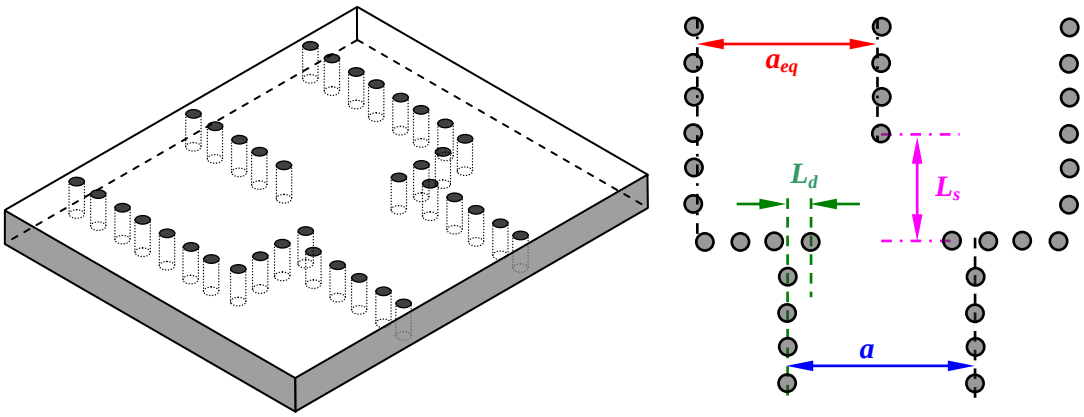

(a) (b)

Figure 4.10 SIW Y-junction (a) structure and (b) design parameters

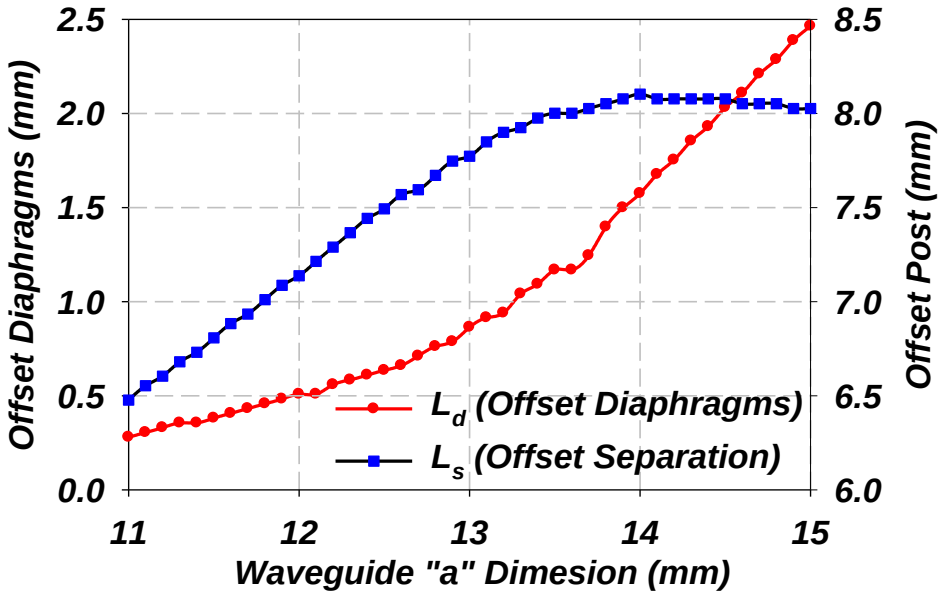

Figure 4.11 Design charts of the SIW Y-junction.

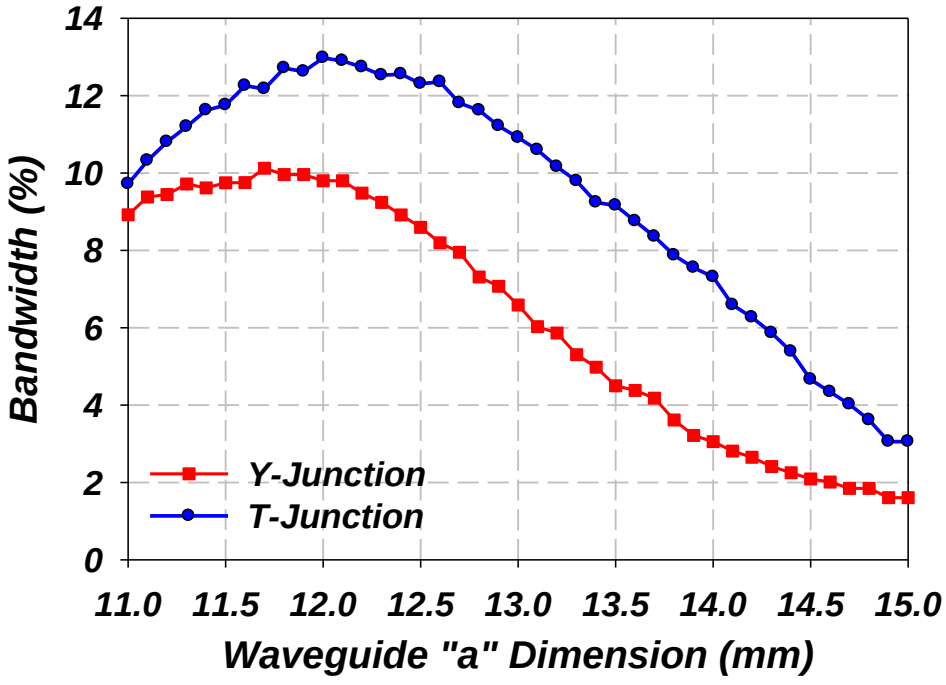

Figure 4.12 Bandwidth of Matched SIW T and Y junctions

4.2.4 Compact SIW Junctions

Both of the SIW Y and T junctions can be modified by rotating the input waveguide by a 90° to achieve compact junction designs. As shown in Figure 4.13(a), the input port of a regular SIW T-junction is rotated to be parallel to the output waveguides, and a short circuit termination is added. A matching post needs to be introduced at strategic locations to cancel the reflections from the junction. A similar T-junction structure is discussed in [22] for rectangular waveguides, and here, we "translate" it into an alternative SIW structures in order to build compact feed networks.

As shown in Figure 4.13(b), the Y-junction can be modified by the same way with short circuit termination and matching posts. If the end of the input waveguide is not terminated, a fourth port can be added to form a "π" shaped junction. Same as its counterpart in rectangular waveguide [23], the four terminal SIW "π"-junction can also be cascaded to form a compact series feed network. However, the modified junctions are no longer symmetric, so an even power distribution with balanced phase is not achievable over a wide frequency band. Design of the compact "t" and "π"-junctions are not straight forward as there are more than 5 design parameters in each case. Extensive EM simulation is required in both cases.

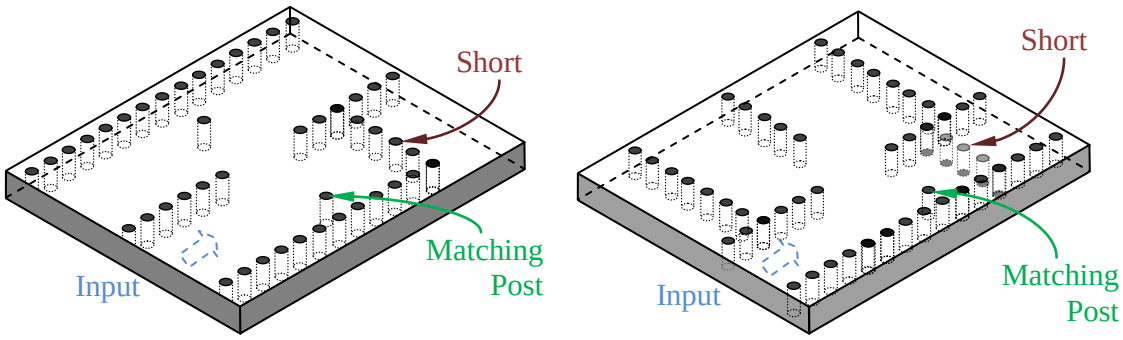

(a) (b)

Figure 4.13 Compact SIW Junctions. (a) "t"-junction, (b) "π"-junction

4.3 SIW Transitions

Transitions from planar circuits, such as that for the low noise block "LNB" to SIW are required at the input of the SIW feed network. Different topologies can be used to transform SIW to either microstrip or Coplanar Waveguide though an E-filed or H-field coupling depending on the thickness of the SIW. For multi-layer SIW slot arrays with the feed network and the radiating SIWs on two different layers, a transition between these two layers is also required. In the following sections, various transition designs between the SIW and planar circuits or even layers of the SIW multi-layer structure will be discussed in detail.

4.3.1 CPW to SIW transition

For SIW with thin substrates, the SIW can be transitioned to microstrip line through a simple tapering [18]. However, for thick substrates, SIW to coplanar waveguide (CPW) transition is more appropriate as CPW's characteristic impedance is almost independent from the substrate thickness, and has closer value to the SIW's characteristic impedance. A SIW to CPW transition based on an E-field coupling is introduced in [24], where the insertion loss is very high due to radiation. A current probe transition (H-field coupling) from the grounded coplanar waveguide (GCPW) to SIW [25] is used in our design to convert SIW to planar circuits. Such transition allows the slotted SIW antenna to be easily integrated with active devices as required in the later design stages. As shown in Figure 4.14(a), a plated through hole is placed in the junction to operate as a current coupling probe. To insure full power transfer, the GCPW is terminated by an open circuit right next to the coupling probe, where the current flowing through the probe generates a magnetic field that has similar distribution to that of the H-field of the TE_{10} mode in the SIW. In addition, via holes are strategically placed along the GCPW to cancel the parallel plate mode in the GCPW line, and to cut off the waveguide modes entering the GCPW from the SIW. In order to allow easy connection to the coaxial connectors, a characteristic impedance of 50 Ω is selected for both the GCPW and the SIW lines.

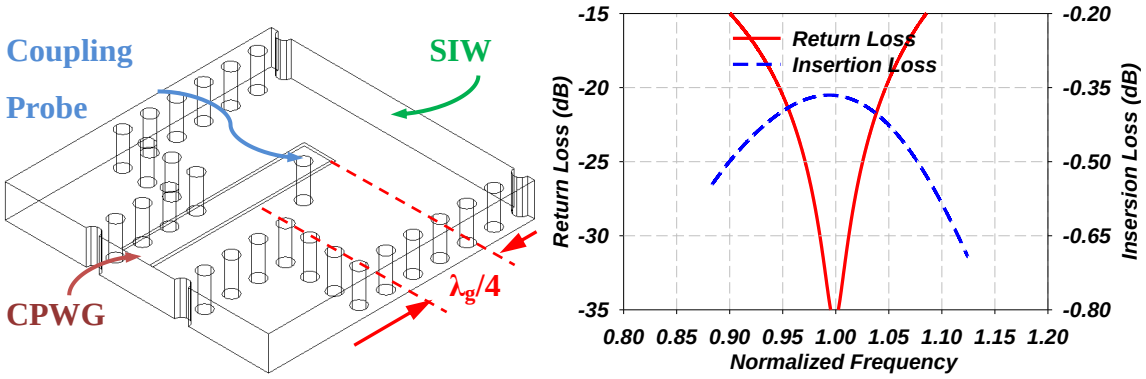

(a) (b)

Figure 4.14 (a) CPWG to SIW transition, (b) Simulated results of back to back transitions

Based on the simulated return and insertion losses of a back to back transition, shown in Figure 4.14(b), it is anticipated that we can achieve excellent input match for these transitions. In this design however, for the selected dielectric substrate material and thickness, we have to use the minimum manufacturable slot width in the GCPW structure to achieve a 50 Ω characteristic impedance. Similarly, the SIW "a" dimension has to be increased to form a 50 Ω line. So it is appropriate to use this transition structure in the array design, but a wideband transition with flexible characteristic impedance on the SIW side would be more suitable for general testing purposes, details of which are discussed in the next section.

4.3.2 Wide-band CPWG to SIW Transition

As discussed in the previous section, the use of CPW with a ground would reduce the loss caused by the radiation of the transition structure. Here we propose a CPWG to SIW transition using an E-field coupling, the drawing of which is shown in Figure 4.15(a). As can be seen, the coupling slots are cut on the top surface of the SIW and placed right next to the short circuit termination of the SIW. The coupling slots act like a magnetic dipole antenna with a strong E-field across the slot in the center and it is weaker on the end of the slot. Such distribution matches the E-field distribution of the TE_{10} mode in the SIW structure, hence a smooth transition can be achieved.

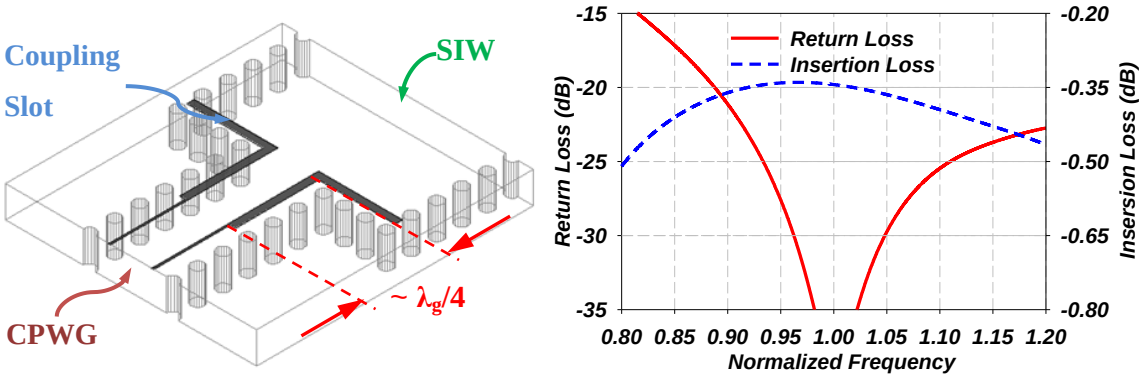

(a) (b)

Figure 4.15 (a) CPWG to SIW transition using coupling slots. (b) Simulated results

The simulated results of the SIW to CPWG transition using coupling slot is shown in Figure 4.15(b), where a wider operating bandwidth is achieved (>15%@-25dB) comparing to the coupling probe structure (~6%@-25dB). Additionally the corresponding insertion loss performance is also improved. Meanwhile, this slot coupling transition structure does not require the SIW section to be 50 Ω as a quarter wavelength impedance transformer is added in the CPWG region to convert the SIW characteristic impedance to the CPWG port impedance.

4.3.3 Ultra Wide Band (UWB) CPWG to SIW Transition

The impedance transformer used in the previous wide-band CPWG to SIW transition limits its bandwidth. An even wider transition bandwidth can be achieved by integrating the coupling slot and the impedance transformer into one tapered coupling slot. As shown in Figure 4.16(a), the sidewalls of the SIW are tapered along the triangle shaped coupling slot such that the direction of the electric field on the coupling slot is always perpendicular to the SIW sidewalls, where a smooth transition can be achieved. The tapered coupling slot also serves as an impedance transformer to transform any arbitrary impedance line in SIW to the CPWG port impedance.

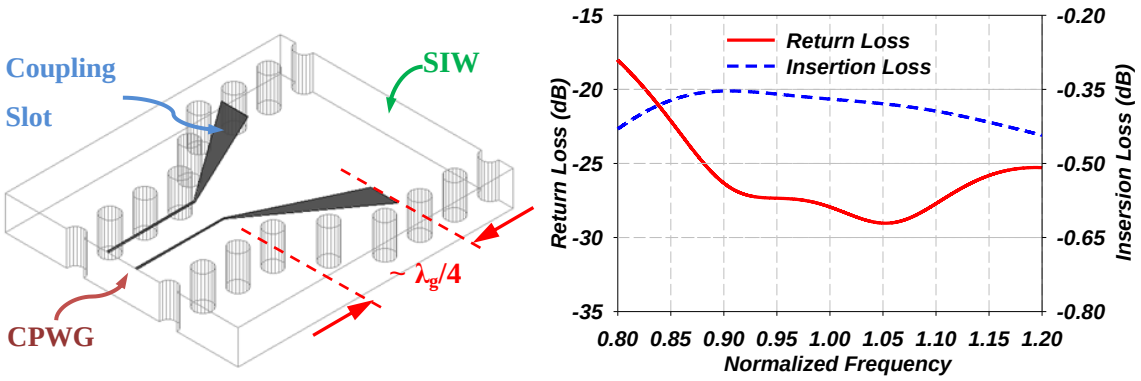

(a) (b)

Figure 4.16 (a) UWB CPWG to SIW transition using coupling slots. (b) Simulated results

The simulated result of an UWB CPWG to SIW transition is shown in Figure 4.16(b) where more than 35% bandwidth is achieved at -25dB return loss. The insertion loss is almost the same as the other two topologies -- but with much wider usable bandwidth too. This UWB transition can also be used to feed high efficiency UWB antenna arrays as described in [26][27], and other UWB antennas as well [28].

4.3.4 Transition between SIW Layers

Antenna array feed networks can be folded to the back of the radiating SIW elements to save space and to reduce the antenna height in our application. This requires a smooth transition between the multi-layer SIWs built on two stacked layers. Coupling using slots is one convenient way of connecting the two SIW layers as it allows the two connecting layer to be manufactured separately and then attached together. As shown in Figure 4.17(b), at the end of each SIW in the feed network, a transverse slot is cut on the top broad wall to couple to the radiating waveguides. Similar slots are also cut at the bottom of radiating SIWs and should be aligned with that of the feed layer. During assembly, the two SIW layers that were built separately can be "glued" together with the coupling slots facing each other, using a very thin layer of bonding film. To assure secure contact between the two layers, extra screw holes through two layers are placed around the coupling slot to allow good mechanical attachment and alignment of the two boards.

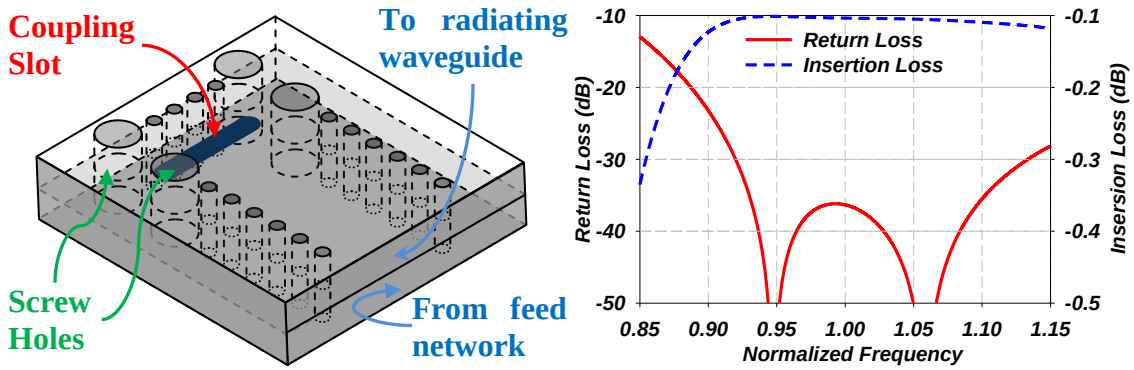

(a) (b)

Figure 4.17 (a) Coupling slots between two substrate layers. (b) Simulation Results

Since the output of the feed network and the radiating waveguides are designed to have the same "a" dimensions, this through layer transition should provide an excellent match over a wide bandwidth as predicted and shown in Figure 4.17(b).

4.4 Conclusion

In this chapter, the concept of Substrate Integrated Waveguide has been introduced to the development of low cost, light weight antenna array and their low loss feed networks. The propagation constant and the attenuation coefficients of the SIW structure were studied, where an equivalent dielectric filled rectangular waveguide model is developed according to the SIW's propagation characteristics. The loss estimate using the equivalent model is proved to be accurate for dielectric and leakage losses, but the conductor loss developed estimate still need to be scaled using a fudge factor to account for manufacturing limitations.

Various types of SIW junction components have been developed as "translations" from their rectangular waveguide counterparts. Design charts are summarized for the SIW T and Y-junctions, and their compact design versions are introduced as well. The design guideline for a low loss feed network were outlined, where the SIW with the lowest loss

can be selected for each section as long as the junction structures with corresponding dimensions are capable of supporting the required bandwidth.

Three structures for transitioning between the SIW to planar or other SIW layers are introduced with their corresponding operating bandwidths and insertion loss performances. Especially, two of these novel structures support adequate wide band operation and good results have been demonstrated.

Chapter 5

Slotted Substrate Integrated Waveguide Array Antennas

In this section, a direct "translation" of the same travelling wave slot array antenna implemented onto printed circuit substrates using SIW technology rather than metallic waveguides will be introduced. Several SIW slot arrays are developed and there radiation patterns are evaluated using near field measurements. In section 5.1, the previously developed equivalent dielectric filled rectangular waveguide model, the SIW junctions and transitions are tested in the design or of both a single radiating SIW and a 16 elements sub-array. Comparisons are made between the sub-array on SIW structure and the previously developed metallic rectangular waveguide sub-array. In section 5.2 a systematic design "recipe" is introduced for the synthesis of the SIW radiating elements, including the determination of slots' length, spacing and number of slots per radiating SIW. It is followed by design examples and measurement results of a 64 radiating SIW slot array in section 5.3 and a multi-layer 32 radiating SIW slot array with folded feed in section 5.4. Conclusions are drawn in section 5.5.

5.1 Slotted SIW Antenna Construction and Comparison

In this section, the radiating waveguide design of travelling wave slot array using rectangular waveguide is "translated" into SIW based on the equivalent dielectric filled rectangular waveguide relationships developed in the last chapter. However, for SIWs, due to the dielectric loading, the phase velocity inside the SIW is much slower, such that it cannot "catch up" with the phase velocity of free space propagation outside the SIW to form a forward looking radiation. Instead, a new beam angle control mechanism different from 3.1.2 is introduced here. The SIW T, Y- junctions and probe coupling of a CPWG to SIW transitions are also implemented in a 1 to 16 binary power divider for a 16 radiating SIW sub-array design. The measurement results of the sub-array are presented here and the SIW sub-array is compared to its metallic waveguide counterpart as well.

5.1.1 Beam Angle Control of Slotted SIW Array

The radiated beam in a dielectric loaded waveguide rather being in the forward direction of the travelling wave, will be backward (i.e. $\theta<0$). This is due to the effect of the dielectric loading on the phase velocity. As shown in Figure 5.1, this phase relationship in the dielectric filled waveguide case can be expressed as:

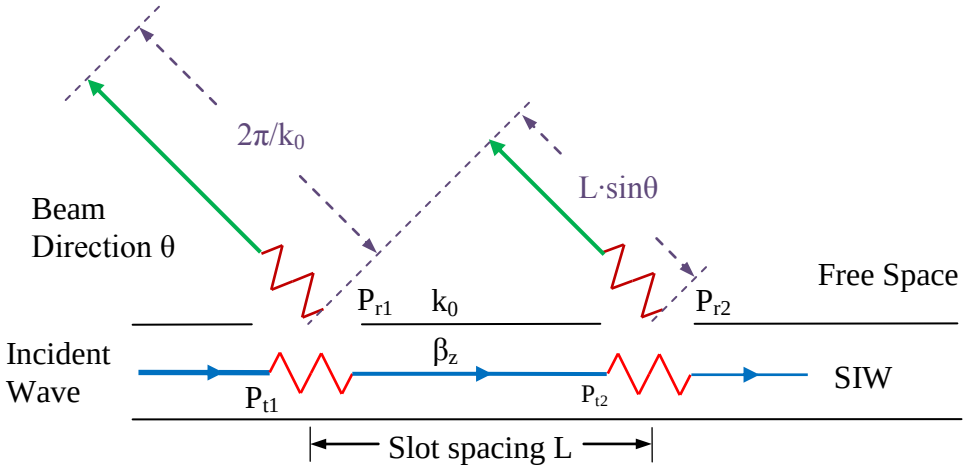

Figure 5.1 Phase diagram of travelling wave slotted SIW antenna array

$$P_{t1} + \beta_z \cdot L + P_{r2} + k_0 \cdot L \sin\theta - P_{r1} = 2\pi$$

$$\sin\theta = \frac{\lambda}{L}\left(1 - \frac{P_{t1}}{2\pi}\right) - \sqrt{\varepsilon_r - \left(\frac{\lambda}{2a}\right)^2} \qquad \text{Equation 5-1}$$

where λ indicates free space wavelength and ε_r represents the dielectric constant of the filling dielectric, i.e. the substrate, P_r and P_t represent the phase change of the radiated and travelling waves caused by these slots respectively. Meanwhile, the beam tilt angle is still a function of the operating frequency. At higher frequency, the beam tilt angle decreases (moving toward zenith) and vice versa.

For the translated design using SIW, the concept of dual circular polarization is the same as the previously developed design for the metallic waveguide slot array in section 3.1.1. As shown in Figure 5.2, "X" shaped slots are densely arranged on the broad wall of the radiating SIW structures, where the leaky waveguide radiates a circular polarization at the main beam that with a large tilt angle that can be controlled to be about 45º degrees from zenith. Fortunately, these slots now can be accurately defined using chemical etching -- a low cost and accurate process relative to the CNC machining required for the fabrication of the metallic waveguides.

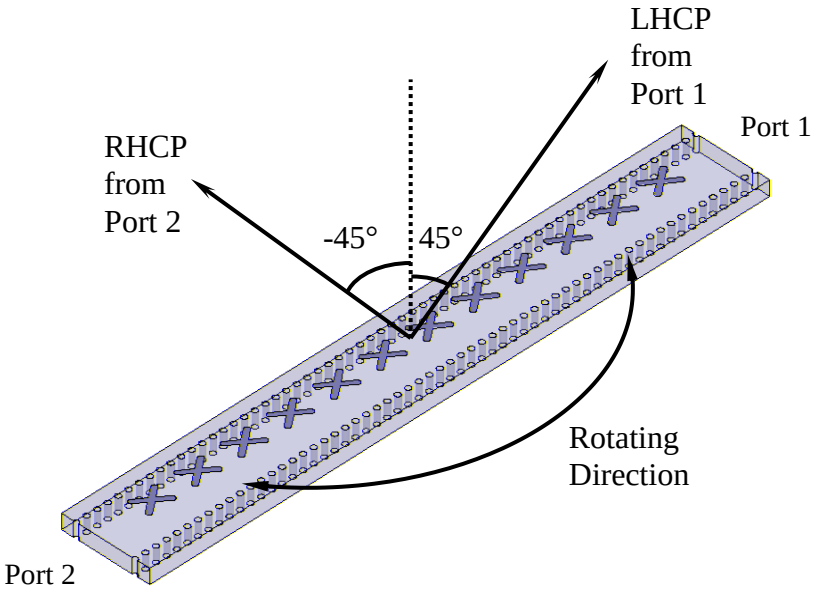

Figure 5.2 Dual Circular Polarization realization using SIW

As can also be seen from Figure 5.2 as an example, because of the backward radiation, when the cross-slots are excited by a mode propagating from Port1 to Port2, the slots radiate a main beam with a 45º tilt angle and left-hand circular polarization. On the other hand, when the same slots are excited by a mode traveling from Port2 to Port1, a right-hand circularly polarized beam is generated with a tilt angle of -45º.

5.1.2 Single Radiating Element Design

In order to validate the slot array design concept when implemented on SIW structures, single radiating element is first designed and prototyped utilizing SIW. As shown in Figure 5.3, a 3.175mm (125mil) thick Rogers RT/Duroid 5880 substrate is used and via holes are drilled through the dielectric substrate to outline the SIW structure and these vias will be subsequently plated with metal. At the same time, 12 "X" shaped slots were etched on the top metallization of the substrate and comprise the radiating structure. At each end of the antenna, a SIW to CPWG probe transition is used to connect the antenna to a SMA connector. Figure 5.4(a) shows the radiating element dimensions, where the width of the SIW "L_3" is selected to be 14.2 mm, which is the same size as the low loss feed network that will be introduced in section 5.1.3. The sidewalls of the SIW consists of a 1.27mm diameter vias with a 2.54mm spacing, which gives an equivalent "a_{eq}" = 13.5 mm according to the analysis of section 4.1.1. The offset of the slots from SIW center line OO' is S_1 = 2.29 mm, which is selected to obtain circular polarization radiation. The total length of each unit cell, also known as the element spacing between slots, "L_1" is 11.18 mm, and the slots have the same width S_2 = 1.27mm and length L_2 = 9.65mm.

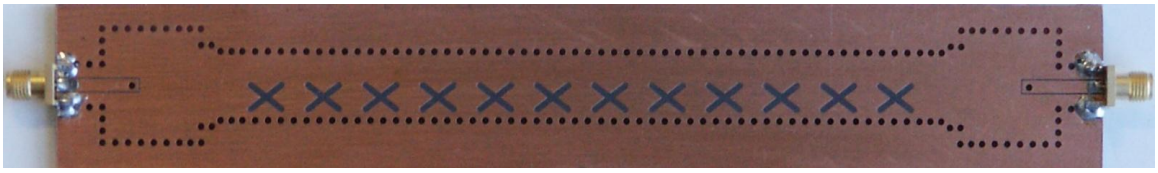

Figure 5.3 Fabricated slotted SIW (single radiating SIW)

All these parameters are chosen based on the SIW's equivalent dielectric filled waveguide dimensions and the design guidelines discussed in Chapter 3, optimized to maximize the gain of the main beam, while maintaining a good axial ratio at 45º degrees off broadside. As shown in Figure 5.4(b), excellent axial ratio has been predicted at the peak of the RHCP radiation, which is approximately an angle 45° off-broadside.

5.1.3 16 Radiating SIW Sub-array Development

A 1 to 16 binary power divider has been synthesized based on the SIW T- and Y-junctions to serve as a feed network for the 16 radiating SIW Sub-array design. According to the SIW loss analysis discussed in Chapter 4, both dielectric and conductor losses decrease when a wider SIW is used. However, based on the design curves of the SIW junctions (shown in Figure 4.12), the corresponding bandwidths of the junctions decrease as well. So a maximum "a_{eq}" = 13.5 mm is selected to minimize the feed network loss while ensuring the SIW junctions have adequate bandwidth to cover the 12.2-12.7 GHz DBS services. A sketch of the 1 to 16 even power divider is shown in Figure 5.5, where three stages of SIW T-junctions and one stage of SIW Y-junction is used. The use of symmetric T- and Y- junctions provides an even power and phase distribution at all 16 output ports over a the design frequency range.

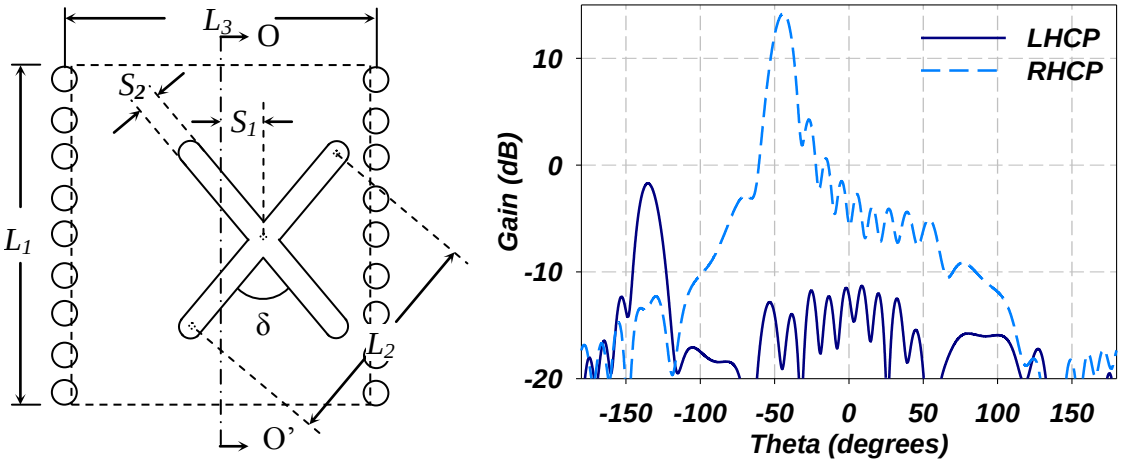

(a) Unit element dimensions (b) Predicted radiation pattern

Figure 5.4 Unit cell element dimensions and predicted single SIW slot array performance

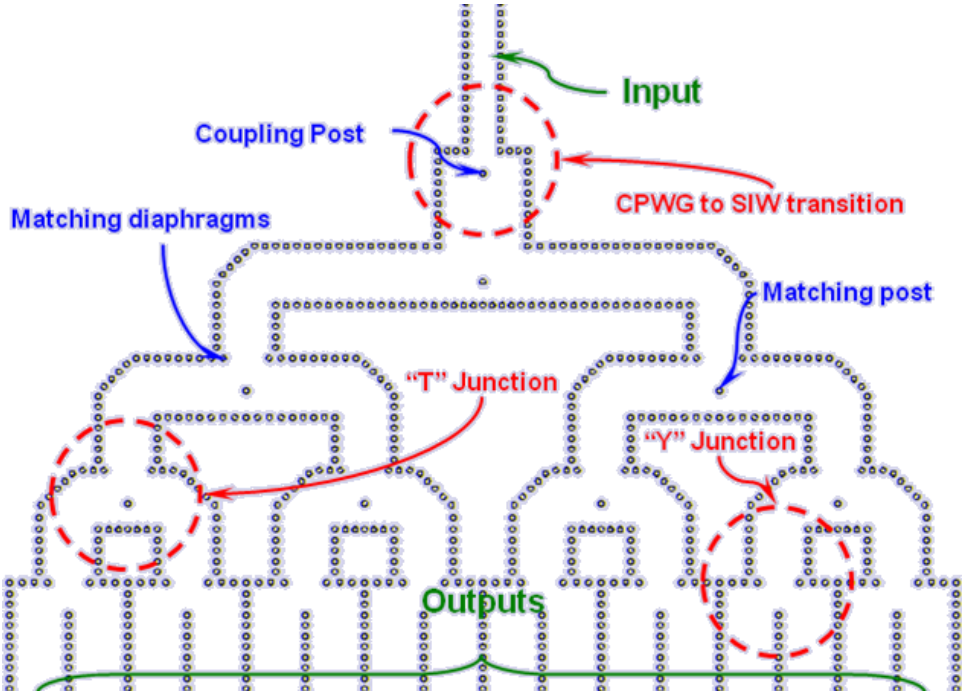

Figure 5.5 SIW 1 to 16 even power divider

However, this feed network takes lots of spaces such that it is almost the same size of the radiating SIWs, as shown in the picture of the fabricated 16 radiating SIW sub-array prototype (as shown in Figure 5.6)[29].

5.1.4 Metallic vs. SIW Sub-array Comparison

A comparison of the slotted waveguide array antennas fabricated using CNC machine, and the SIW implemented using standard PCB technology is shown in Table 5-1. Although both the metallic and the SIW solutions are designed to have the same main beam tilt angle, the directions of their main beams are opposite due to the dielectric loading as previously described. For both cases, the two circularly polarized beams from the same satellite still can be addressed one at a time by mechanically rotating the whole antenna a 180º in azimuth plane.

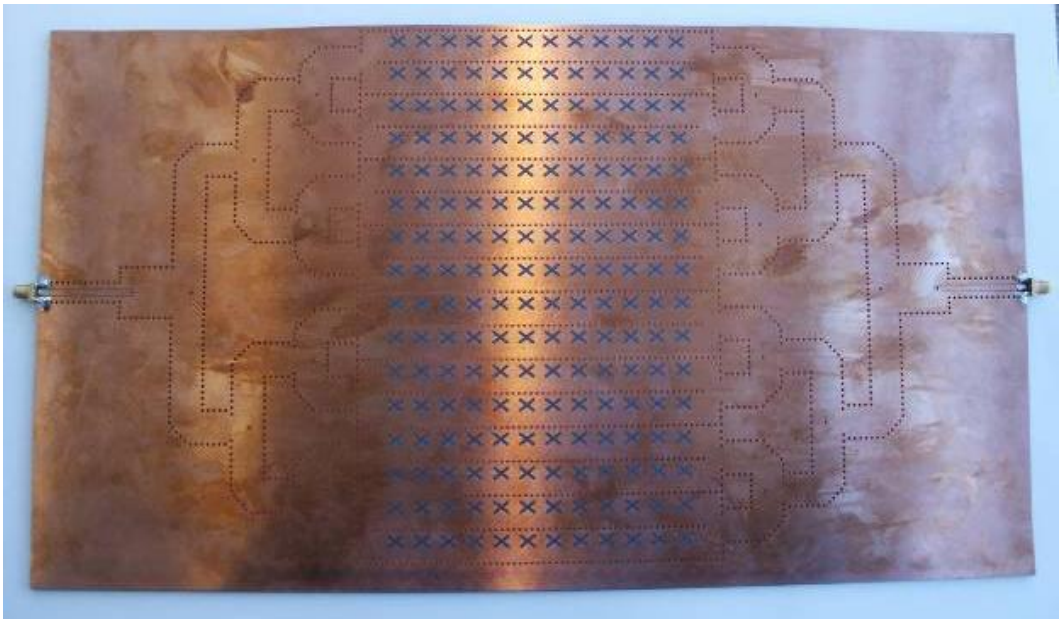

Figure 5.6 Fabricated 16 radiating SIW sub array prototype

Table 5-1 Comparison between Metallic Waveguide and SIW Slot Sub-arrays

	Metallic Waveguide Slot Array	SIW Slot Array
Cost	Very high, requires CNC machining, and high precision manufacturing	Low, slots are 1 mil accurate using conventional PCB technology
Loss	<0.025 dB/in for WR62 with a 0.280 in reduced height waveguide	<0.07 dB/in, for a 0.125in. thick Duroid 5880 substrate
Beam Tilt	Metallic waveguide travelling wave slot array radiates forward	SIW slot array radiates backward
Feed Network	Requires wider "a" dimensions, less area efficiency. Need multi-layer feed network for large arrays.	Feeds could be easily integrated with coplanar circuits. Less than 0.25 inch for two layer feeding networks
Weight	Bulky, heavy	Light, and low profile
Assembly	Many pieces, complicate to assemble	Standard PCB, no need to assemble

5.1.5 SIW Sub-array Measurement Results

We have carried out S-parameter measurements of the 16 radiating SIW sub-array using HP8510C network analyzer, and their results are shown in Figure 5.7. The measured return loss is better than -18 dB, and the transmission (termination) coefficient is less than -15 dB within the design operating frequency range of 12.2-12.7GHz.

The SIW sub-array's radiation patterns are evaluated using near field measurement setups [30]. As shown in Figure 5.8, the developed slotted SIW sub-array is vertically mounted in front of the probe antenna in the near field range. The antenna remains stationary during the test while the probe antenna scans the surface of the slot array and records the magnitude and phase data to form a 2-D near field grid. Then the far field radiating pattern can be obtained using a Fourier transform of the near field grid results. The sub-array is fed one port at a time to form two independent circularly polarized beams. For each polarization, two orthogonal cuts across the main beam are shown in Figure 5.9 and Figure 5.10 at 12.45 GHz for the LHCP and RHCP respectively.

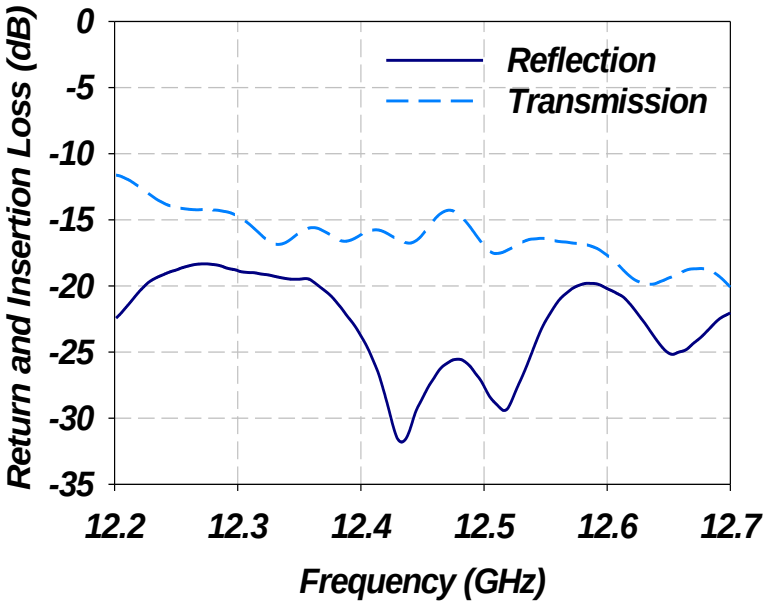

Figure 5.7 Measured S-parameters of 16 radiating SIWs sub-array

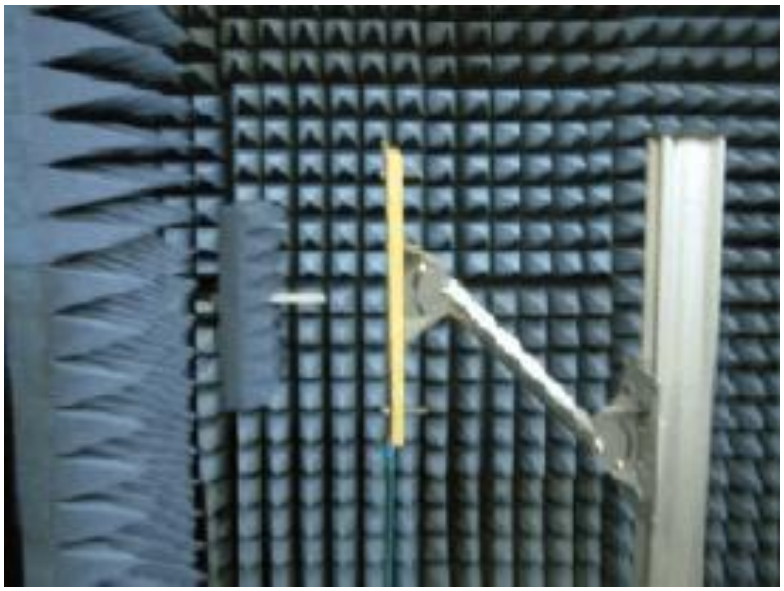

Figure 5.8 Near field measurement setup

The far field measurement results, including peak gain, beam tilt angle, sidelobe and cross polarization levels are summarized in Table 5-2. Note that over 24.7 dBi gain has been measured at the center frequency for both polarizations. This is equivalent to over a 65% efficiency (not including the projection loss). Furthermore, cross polarization levels were also measured, and were always better than 20dB down from the peak of the main beam at the center frequency, which indicates a good axial ratio. The measured radiation patterns match very well the simulated elevation cut radiating pattern of the single radiating SIW (Figure 5.4b). As shown in Table 5-2 Measured results for the 16 radiating SIW Sub-array, at the center frequency, the beam points exactly to 45°. However, it has a pronounced frequency dependent beam squint, and there is a 13° difference in the beam tilt angle between the lowest and highest frequencies. This beam squint also helps the higher end of the frequency band to have relatively higher gain as the projected area of the array is larger when the beam has less tilt angle. This effect produces a ~1dB gain improvement at 12.7GHz and but causes an equal gain drop at 12.2GHz as compared to the center frequency. This beam squint can be accounted for by introducing a look up table in the tracking system, and then the antenna tilt angle can be adjusted based on the selected channel number.

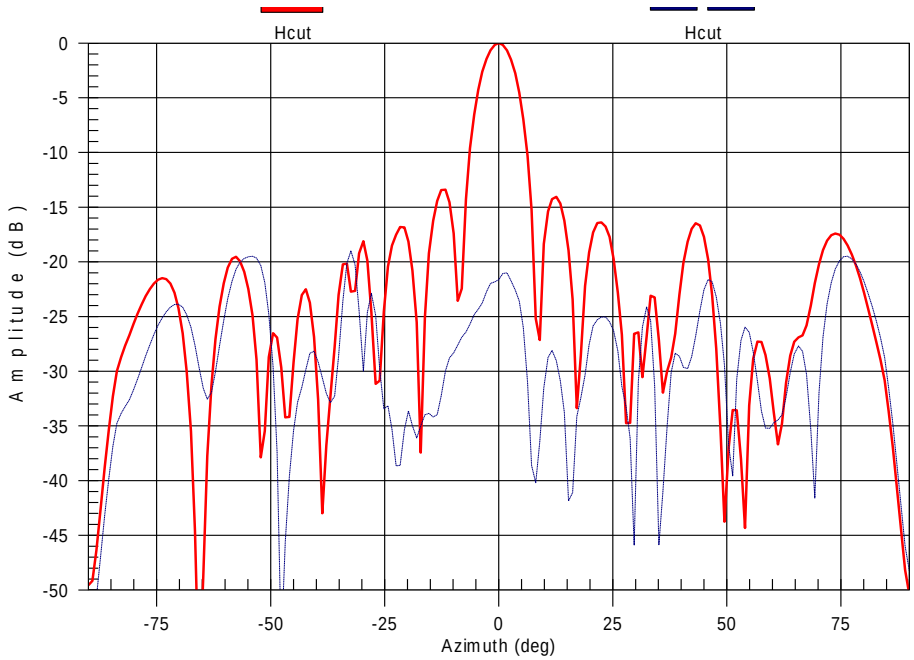

(a) Azimuth cut

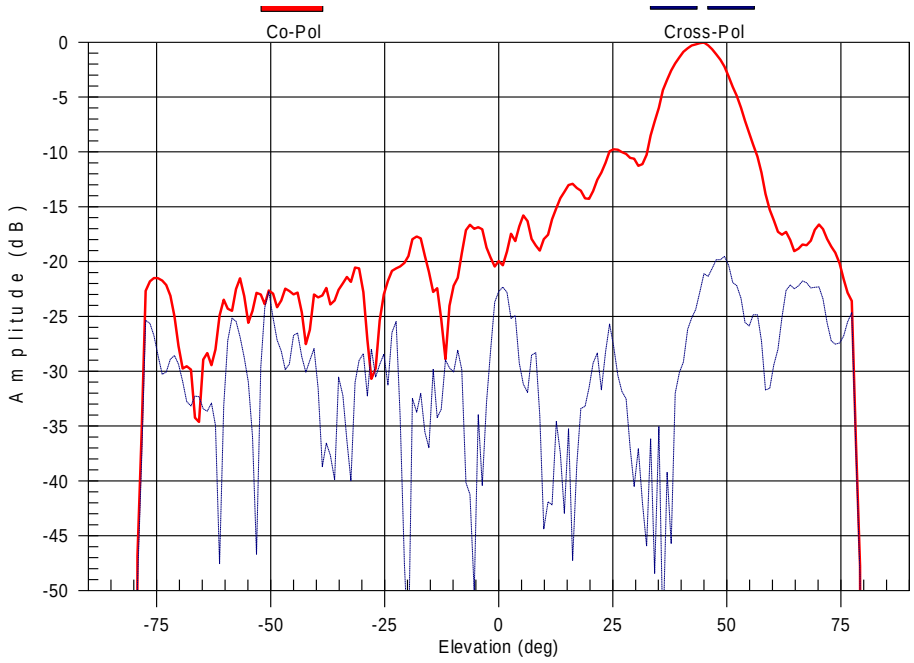

(b) Elevation cut

Figure 5.9 LHCP Radiation patterns of 16 radiating SIW sub-array at 12.45GHz

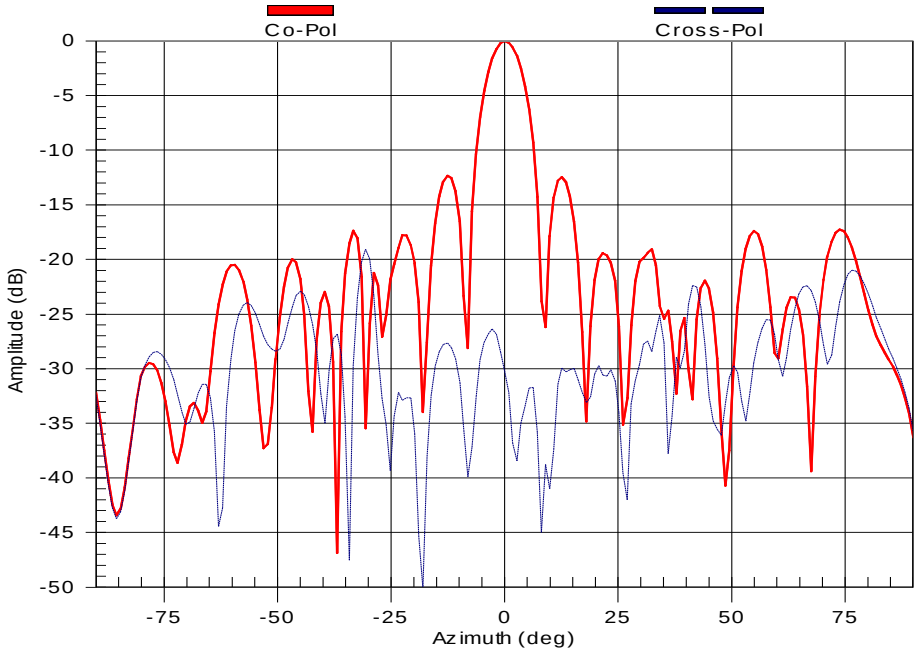

(a) Azimuth cut

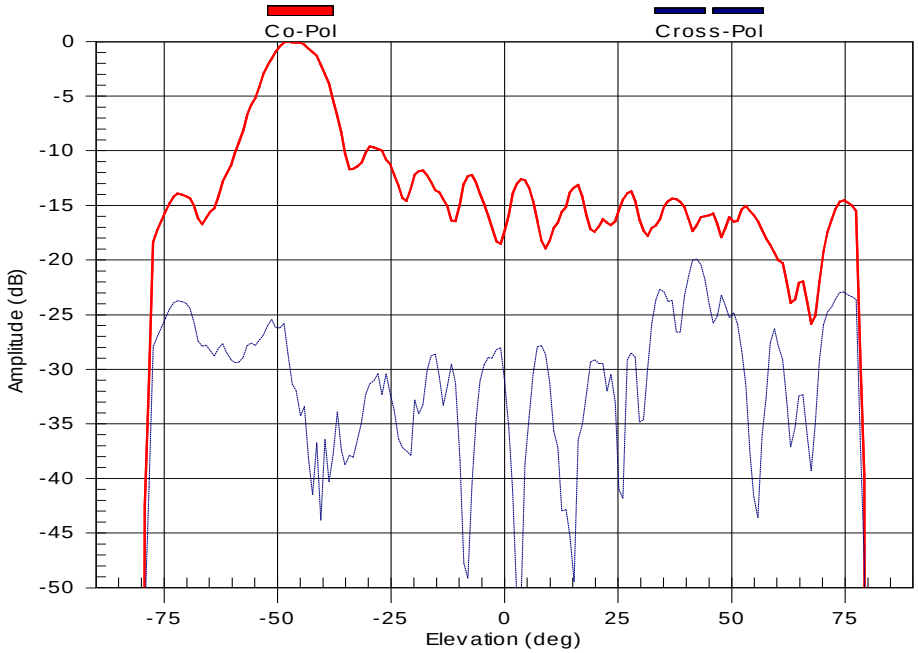

(b) Elevation cut

Figure 5.10 RHCP radiation patterns of 16 radiating SIW sub-array at 12.45GHz

Table 5-2 Measured results for the 16 radiating SIW Sub-array

Frequency	Polarization	Peak Gain (dBi)	Elevation Peak (deg)	Sidelobe level (dB)	Cross Pol level (dB)
12.2GHz	LHCP	23.29	50.2	-9	-17
12.45GHz	LHCP	24.72	44.7	-9.7	-21
12.7GHz	LHCP	25.51	36.9	-15	-20
12.2GHz	RHCP	23.79	-52.9	-9	-21
12.45GHz	RHCP	24.73	-45.4	-9.5	-26
12.7GHz	RHCP	25.71	-39.9	-14	-22

The measured sidelobe levels are relatively high, which is expected as all the radiating slots have the same length and no tapering is applied. This is a disadvantage especially when the sidelobe is located between the main beam tilt angle and zenith. This relatively high sidelobe levels will not only complicate the tracking of the satellite but also collects cosmic noise, such as that radiating from the sun. A non-uniform tapering of the radiating slots (as discussed in section 3.1.3) could be applied to achieve a relatively lower side lobe level. Antenna array designs with non-uniform slots will be discussed in Sections 5.3 and 5.4.

For this sub-array design, the feed network has been optimized for the lowest insertion loss, but still, the efficiency of the SIW is slightly lower than that of the all-metallic version due to the dielectric substrate material loss. However, the loss of the former is still relatively small, and would allow increasing the number of the radiating waveguides, which should result in an acceptable performance as will be discussed in detail in the following sections.

5.1.6 Summary

The previously developed metallic rectangular waveguide slot array antenna has been successfully converted into SIW slot array design. The 16 radiating element slotted SIW sub array is designed based on developing an equivalent dielectric filled waveguide structure based on SIW and SIW junctions. The SIW structure has been fabricated using a standard PCB technology, and its radiation pattern is evaluated using near field measurements. The measurement results of the SIW sub-array indicate accurate beam tilt angles and very good cross polarization performance. However, the SIW antenna efficiency is lower than the metallic waveguide sub-array due to the dielectric substrate loss, but the loss per unit length is still low enough to justify further expansion of the array size to include more radiating SIWs. The measured sidelobe levels are relatively high and a tapered slot distribution can be used to lower this unaccepted side lobe levels. A detailed "recipe" for the radiating elements design of the travelling wave slotted SIW arrays with an optimum gain and low sidelobe levels will be introduced in the next section, followed by two design examples.

5.2 Synthesis procedure

In this section, a design procedure for the radiating elements of the travelling wave slotted SIW array is outlined, where the slot length, spacing and distribution are determined based on the array size constraints. All these dimensions are synthesized to concurrently achieve maximum antenna gain at a desirable beam tilt angle with a low sidelobe level. An overview of the design flow is given in a flow chart and is shown in Figure 5.11. A design example following these design steps is developed by first selecting the array size in section 5.2.1. The design criterion for a particular beam tilt angle is discussed in 5.2.2, followed by the element dimension requirements for maximizing the gain in 5.2.3. In section 5.2.4, all the design considerations are fed together to determine the optimum slot length, spacing and number of radiating slots. In section 5.2.5, the tapering of the slots is implemented to achieve a low sidelobe level,

while maintaining the gain of the non-tapered distribution, followed by conclusions in section 5.2.6.

5.2.1 Size of the slot array

Previous slotted SIW sub-array implementation shows that the gain of the antenna array can be increased by adding more radiating waveguides in the lateral dimensions. However, adding more elements could increase the insertion loss of the feed network to the point that it becomes prohibitively high and makes the improvement marginal. So in the following design examples, the number of the radiating SIWs is doubled to 32, and then quadrupled to 64, i.e. the next numbers that are also suitable for binary feed network development. Given that the same 125 mil thick RT/Duroid 5880 material with a dielectric constant of 2.2 and loss tangent of 0.0009 is used here to minimize the overall feed loss. The width of these boards are standardized and they are either 18 or 36 inches but their usable widths are either 17 or 34 inches respectively after accounting for a minimum of 1~2 inches tooling margin. So the width of each radiating waveguide is chosen to be 530 mils to fit the proposed waveguide elements. According to the previous analysis in section 4.1.1, the equivalent dielectric filled rectangular waveguide width for the radiating SIWs with a 50 mil via diameter and 100 mil via spacing is 503 mils. Such SIW dimensions support a single TE_{10} mode operation over the entire 12.2-12.7 GHz frequency band. The length of the radiating SIWs is bounded by the height constraints during steering in the elevation plane. For example, for a maximum overall height of a 3 inch at ±25° mechanically steered angle, the maximum allowed radiating waveguide length is 7.1 inch. But, for a two layered array structure, at each end of the radiating waveguide, the transition to the bottom combining network layer extends over a 0.5 inch distance. Therefore, the radiating waveguides length needs to be extended only to 6 inches long to occupy the maximum allowable area and in turn achieves the highest achievable gain. The proper offset to achieve circular polarization can be directly calculated from Equation 3-2, upon replacing the unloaded waveguide wavelength by the wavelength in the dielectric media.

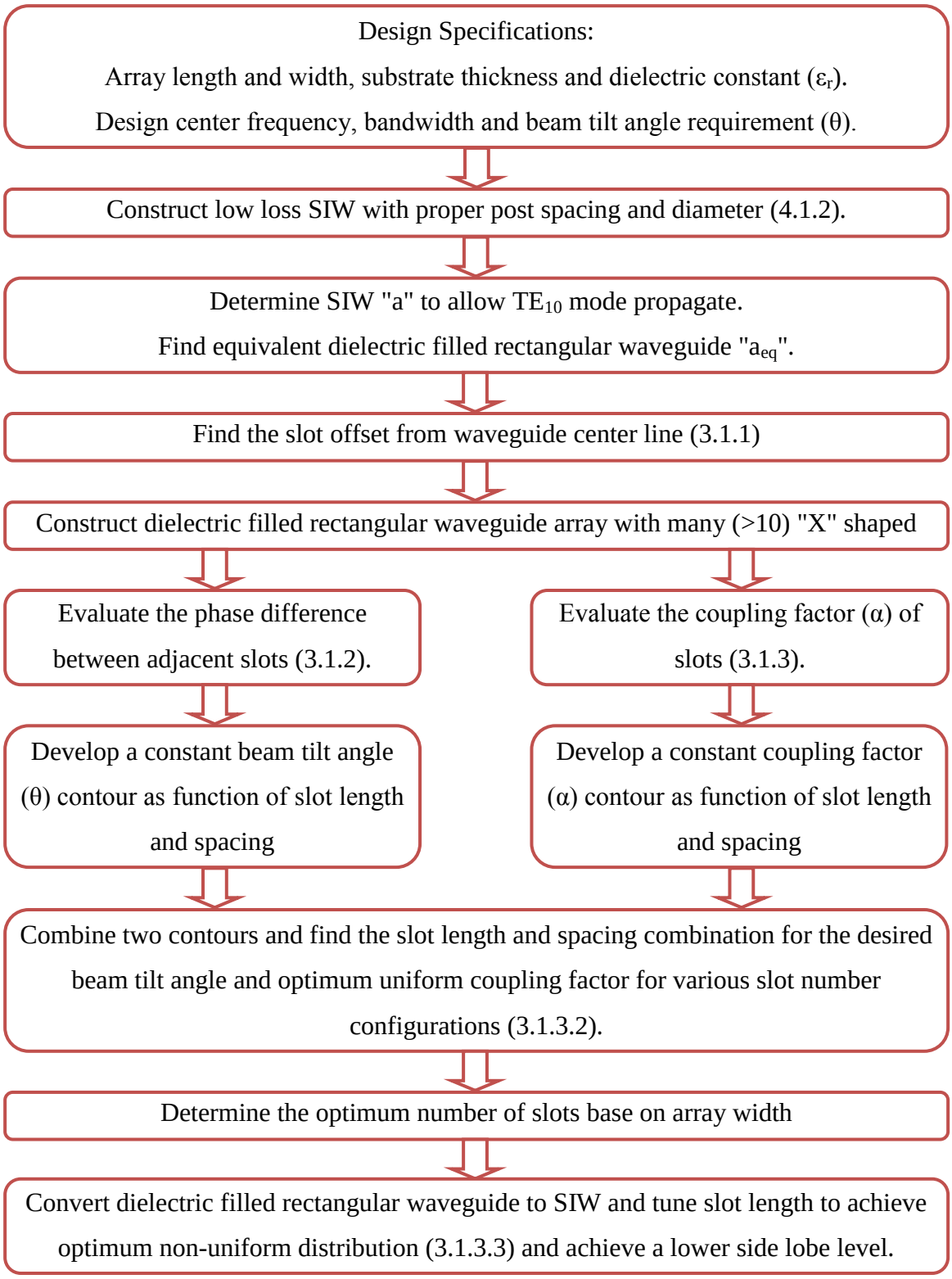

Figure 5.11 Design flow of slotted SIW array radiating elements

5.2.2 Tilt angle control

According to the previous analysis in section 5.1.1, for a backward radiating travelling wave array, the phase difference between the radiated fields from adjacent radiating elements is 2π. In this case, at the center frequency of 12.45GHz, the tilt angle relationship can be simplified as:

$$\sin\theta = \frac{\lambda}{L}\left(1-\frac{P_{t1}}{2\pi}\right)-\sqrt{\varepsilon_r-\left(\frac{\lambda}{2a}\right)^2} = \frac{949}{L}\left(1-\frac{P_{t1}}{2\pi}\right)-\sqrt{2.2-\left(\frac{949}{1006}\right)^2}$$

$$\theta = \arcsin\left[\frac{949}{L}\left(1-\frac{P_t\ \ L,l}{2\pi}\right)-1.145\right] \qquad \text{Equation 5-2}$$

where L is the spacing between the slots and l represents the length of slots. P_t, the change of phase in SIW due to the presence of the "X" shaped slots is a function of both slot spacing and slot length.

In this implementation, the phase change introduced by the slots is evaluated numerically using Ansoft HFSS, an EM simulation tool based on finite element method (FEM). As shown in Figure 5.12, the single radiating dielectric filled waveguide is modeled in HFSS with a plural of (>10) "X" shaped slots. The periodic boundary conditions are applied along both sides of the waveguide to emulate an infinite broadside array (in the azimuth plane). The dielectric filled rectangular waveguide model is used as an equivalent structure to the actual substrate integrated waveguide structure. All the "X" shaped slots have been kept the same size with a proper offset from the waveguide center line to obtain circular polarization . The slot array can be seen as a cascade of unit cells with a length L containing only one radiating element, i.e. linear array unit cell periodic length. The phase of the TE_{10} mode propagation is arbitrarily monitored before and after each unit cell by integrating the vertical component of the E field along a line located in the middle of the waveguide and between the unit cells. The change of this phase due to the

pair of slots, with certain length l and spacing L, can then be estimated approximately by calculating an average of the phase advances for each unit cell, that is:

$$\beta_{zl} \cdot L = P_t \ \ l, L \ \ + \beta_z \cdot L = \frac{1}{N} \sum_{n=1}^{N} \left[\arg\left(\int_{d_{n+1}} \vec{E} \cdot dy \right) - \arg\left(\int_{d_n} \vec{E} \cdot dy \right) \right] \qquad \text{Equation 5-3}$$

where β_{zl} is the loaded guided wave number and β_z is the unperturbed guided wave number in the equivalent dielectric filled rectangular waveguide.

The simulated results of the beam tilt angle θ of the slotted SIW array with the current design parameters are shown in Figure 5.13, where the contours of the constant beam tilt angle values are depicted against various elements spacing (L) and slot length (l). As can be seen, the beam tilt angle contours are very smooth, since the variation of the phase differences between the slots are very small.

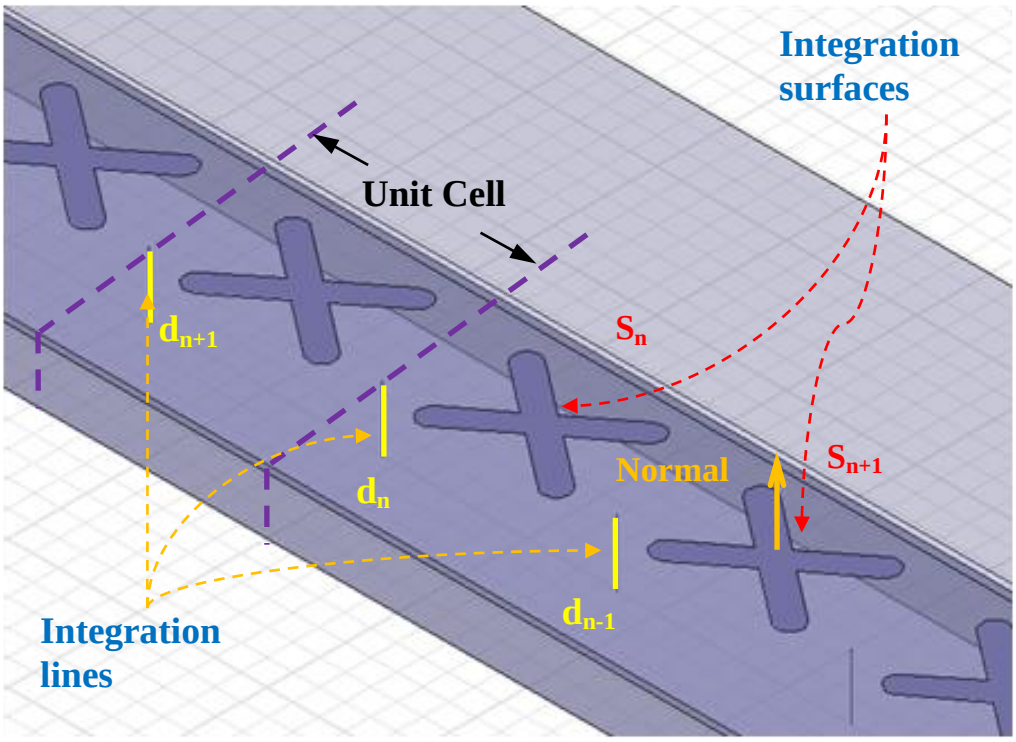

Figure 5.12 Simulation model and numeric integration setup of slot array in HFSS

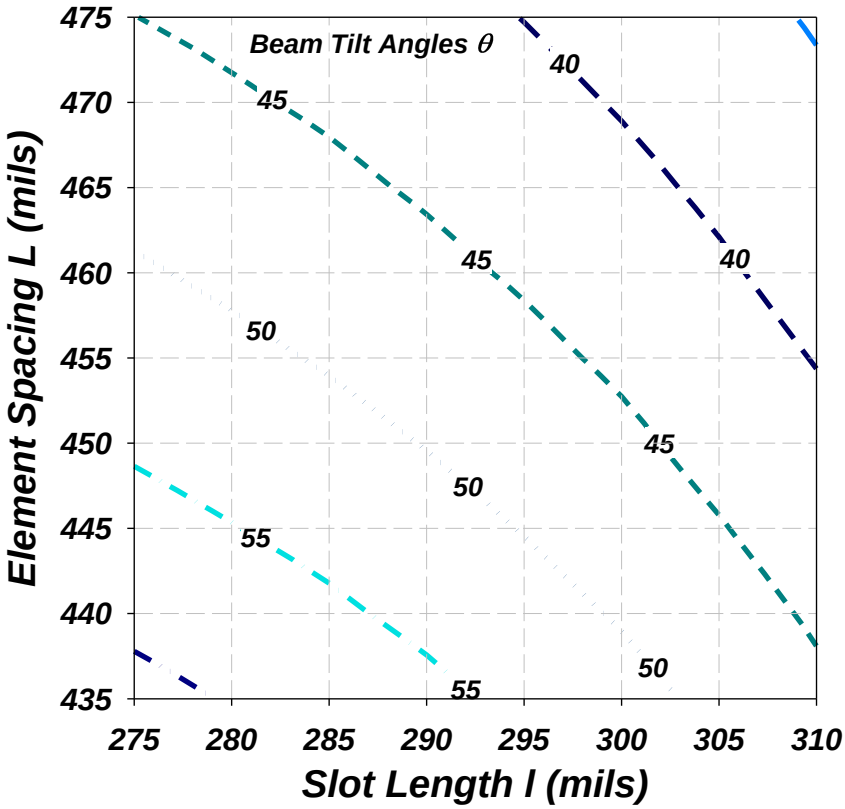

Figure 5.13 Constant beam tilt angle contours of travelling wave slotted SIW array with various slot length and spacing combinations

5.2.3 Evaluation of the coupling factor

Any uniform slot length array with combinations of l and L along the $\theta = 45°$ contour of Figure 5.13 gives a desirable beam tilt for the design. However, in order to achieve the maximum antenna efficiency, according to the previous analysis in section 3.1.3 and Table 3-1, only one specific coupling factor "α" is considered to be the optimum coupling for each element number configuration. So, the coupling factor of slots with certain length and spacing needs to be evaluated in order to determine an optimum L and l combination for each slot number configuration. The coupling factors are also calculated numerically using HFSS through the evaluation of the aperture field intensity. As shown

in Figure 5.12. the power leakage of each slot pair can be calculated as the surface integral of the real part of the Poynting vector normal to the surface, that is:

$$\left|E\ \ n\ \right|^2 \propto \hat{n}\cdot \iint_{S_n} \mathrm{Re}\ \ \vec{E}\times\vec{H}^*\ \ ds \qquad \text{Equation 5-4}$$

The coupling factor α(n) can in turn be calculated as:

$$\begin{aligned}
&\alpha\ \ 1\ = \left|E\ \ 1\ \right|^2 \Big/\ 1-\left|S_{11}\right|^2 \\
&\alpha\ \ 2\ = \left|E\ \ 2\ \right|^2 \Big/\ 1-\left|S_{11}\right|^2 - \left|E\ \ 1\ \right|^2 \\
&\vdots \\
&\alpha\ \ n\ = \left|E\ \ n\ \right|^2 \Big/ \left(1-\left|S_{11}\right|^2 - \sum_{m=1}^{n-1}\left|E\ \ m\ \right|^2\right)
\end{aligned} \qquad \text{Equation 5-5}$$

where S_{11} is the return loss at the input of the slotted waveguide. It is important to recognize here that the reflections from each slot are neglected here and only the overall reflection is taken into account. To have energy conservation, however, the following equation also holds true within an acceptable numerical error.

$$1-\left|S_{11}\right|^2 - \sum_{n=1}^{N}\left|E\ \ n\ \right|^2 \cong \left|S_{12}\right|^2 \qquad \text{Equation 5-6}$$

Where S_{12} is power lost to the dummy termination at the end of the slotted guide.

Due to the finite array edge effect, even when the radiating slots have the same length, the resulting coupling factor in a travelling array environment is not the same. A simulation result of the power coupling factor of a thirteen element travelling wave array is plotted in Figure 5.14 as an example.

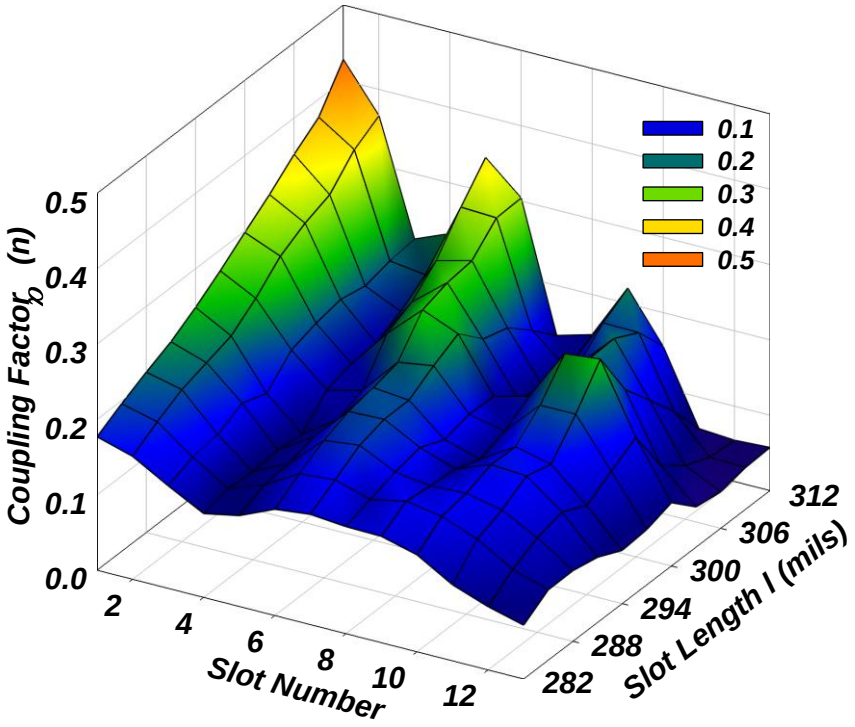

Figure 5.14 Variation of the calculated slot coupling factor for a traveling wave array with a uniform slot length

As can be seen, when the slots are short we are justified to neglect reflections from the various slots, and the calculated coupling factor for all slots are almost the same. However, the variation is more significant when the slots are long and both mutual coupling and reflections are relatively strong. Nevertheless, the average of the "oscillating" coupling factor should be a good approximation and such approximation can be used to assist in the array design.

Through an extensive EM simulation, the contour of the constant slot coupling factor is summarized in Figure 5.15, where the optimum coupling factor values from Table 3-1 are plotted. As a result, for a given array configuration of 11-16 "X" shaped slot elements, the element spacing and slot length combination can be selected anywhere along the corresponding optimum constant coupling factor contours.

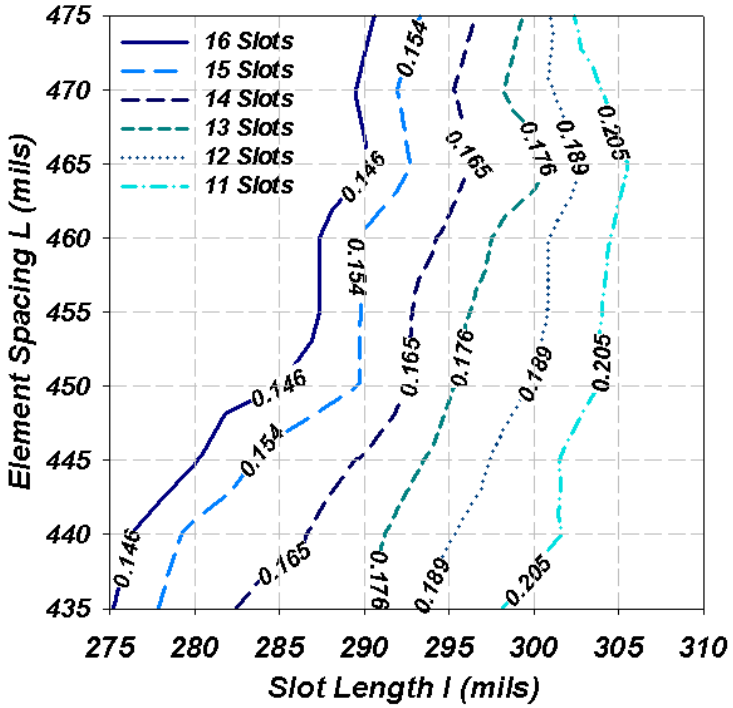

Figure 5.15 Contour of optimum constant slot coupling factor of each element number configurations for various slot length and spacing combinations

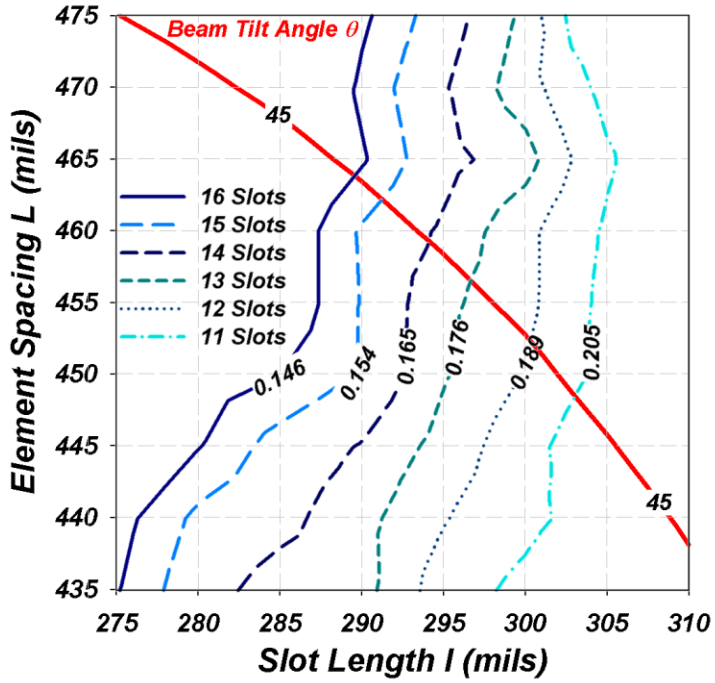

Figure 5.16 Overlay of constant beam tilt angle and constant slot coupling factor contours

5.2.4 Optimum slot length, element spacing and number of slots

For a travelling wave uniform slot array antenna design with a 45° beam tilt angle and maximum gain, the design parameters can be determined by overlaying Figure 5.13 and Figure 5.15, as shown in Figure 5.16. The optimum combination of the slot length and the element spacing can be found in the close neighborhood of the intersections between the constant 45° beam tilt contour and the constant coupling factor contours. The resulting combinations for each element number configuration are listed in Table 5-3.

The corresponding total radiating SIW length is also listed in Table 5-3, where the configuration with 13 radiating slots gives a total length closes to our design length goal of 6 inch. So for the folded feed design, a slotted SIW radiating element with 13 "X" shaped slots is selected. Meanwhile, for the unfolded array design, 12 "X" shaped slots are used in each radiating SIW to reduce the overall antenna length

Table 5-3 Optimum dimensions for various element number configurations

Number of Elements		11	12	13	14	15	16
Optimum Combination	Slot Length l (mil)	303	300	296	294	292	289
	Element Spacing L (mil)	448	453	456	460	462	464
Total Radiating Waveguide Length (in)		4.93	5.44	5.93	6.44	6.93	7.42

5.2.5 Slots Tapering

As discussed in section 3.1.3.3, the optimized non-uniform coupling factor distribution simultaneously offers a high gain and side lobe level suppression. However, in order to implement this optimized tapering (as shown in Table 3-2) in a finite array environment with a strong coupling between the radiating elements, an extensive EM simulation and manual tuning of various parameters are not dispensable. For the design with 13 "X" shaped radiating slots for example, the tuning procedure starts with the uniform slot length and spacing selected in the last step and only the slot lengths are adjusted. Since in the optimum aperture field distribution model, progressively less and less power is radiated by each slot as the wave travels down the waveguide. As a result, each slot has less influence over the previous slot than the next one and so on. Hence, a lot of computational efforts can be saved by optimizing the slot lengths one by one in succession along the direction of wave propagation. The optimized slot lengths are listed in

Table 5-4. The coupling factor and the apertures power distributions of the original uniform length and tapered length slot arrays are shown in Figure 5.17, together with their optimum distribution values (as listed in Table 3-2). In addition to the change in the coupling factor, the tapering of the slot lengths also changes slightly the phase advance between the adjacent slots. Such a change in the phase distribution breaks the periodicity of the slot array and results in a much lower side lobe level. A comparison of the simulated radiation patterns of the original uniform and tapered slot arrays is shown in Figure 5.18. Both arrays demonstrate very good axial ratio at the main beam, and the calculated gain is almost the same before and after tapering the slots. More importantly, the side lobe level of the tapered slot array is about 8 dB below that of the original uniform slot array. This improved side lobe level is very important for DBS signal reception as it is less likely for the antenna to collect noise from the sky (i.e. Sun).

Table 5-4 Optimized slot length distribution for 13 slots radiating SIW design

Slot Numbers	1,13	2,12	3,11	4,10	5,9	6,8	7
Slot Length (mil)	276	279.5	287.5	298	302.5	299.5	297

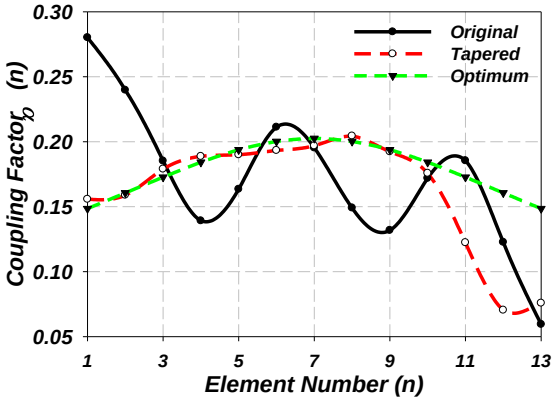

(a) Coupling factor

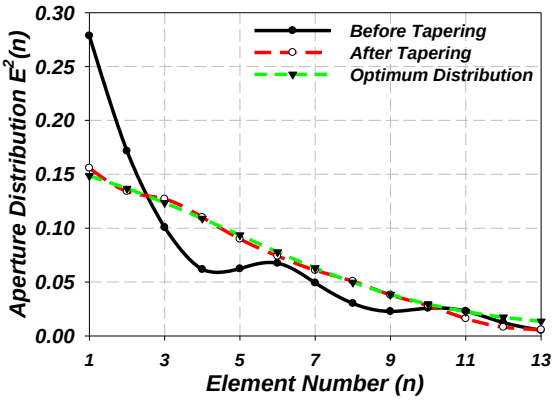

(b) Aperture excitation

Figure 5.17 Distribution of coupling factor and aperture excitation of 13 element travelling wave antenna array before and after tapering process with optimum distribution

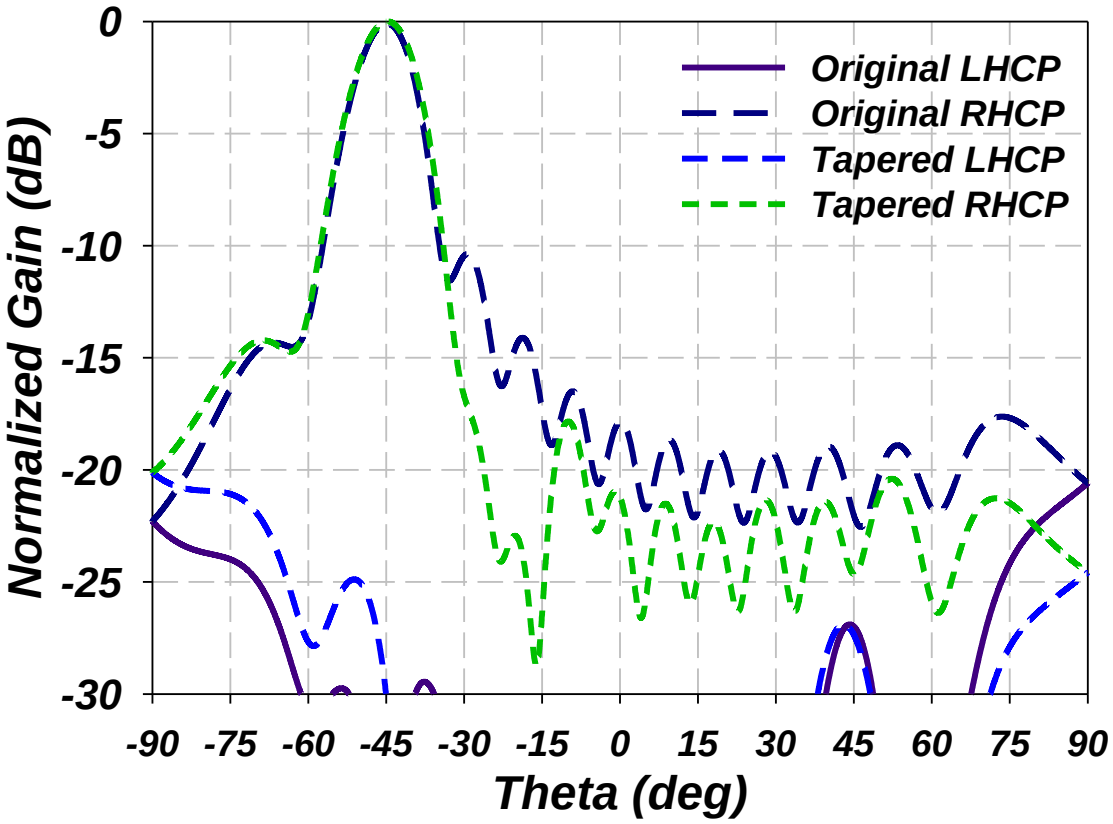

Figure 5.18 Simulated radiation pattern of the uniform and tapered slot array

5.2.6 Synthesis Procedure Summary

A synthesis procedure for the radiating SIW design is introduced, where both the phase change due to the slots and power radiated through the slots are evaluated numerically using EM simulation software. This procedure even though is approximate but had rendered very good experimental results and would be represented here as a recipe, in this synthesis procedure. Contours of constant beam tilt angle and constant coupling factor can be generated as a function of both element spacing and slot length, and the optimum slot parameter combination and number of slots per radiating SIW can be derived accordingly and should provide a good starting point for the slot tapering process. Slot lengths tapered with optimum distribution can provide almost the same gain and significant improvement in the side lobe levels as compared to uniform slot array. Two radiating SIW configurations with 12 and 13 "X" shaped slots have been designed for both single layer and folded slotted SIW arrays, the design of which will be discussed in the following sections.

5.3 Single Layer 64 Radiating SIWs Array

Radiating SIW designs were discussed in the previous section, where the slot lengths and spacing are optimized for a high gain beam at 45° tilt angle with a reduced side lobe level. In this section, a slot array with four times the radiating SIW number of the previously developed SIW sub-array described in section 5.1.3 is developed. This 64 radiating SIW full array is based on the previously described12 "X" shaped slots radiating SIW synthesized in previous 5.2 and a compact 1 to 64 binary power divider. The design of the compact feed network is shown in section 5.3.1, followed by the measurement results of the full array -- in section 5.3.2.

5.3.1 Compact Feed Network Development

Similar to the SIW sub-array design, a binary feed network has been used to implement the SIW full array in order to achieve a good match, wide bandwidth, and a balanced output phases for all slots. Regular SIW T and Y junctions were used in the SIW sub-array design to achieve a feed network with a very low insertion loss and uniform amplitude and phase distribution over the operating frequency band. However, in the full array design, the feed networks need to be smaller than the size of the radiating elements to allow multi-layer developments (i.e. their folding under the radiating aperture) as will be detailed in the next section. So, compact SIW t and π junction designs that were previously discussed in section 4.2.4 are implemented here to minimize the size of the feed network. For instance, a 1:8 power divider design based on compact SIW junctions, shown in Figure 5.19, is noticeably compact. Eight of the compact 1 to 8 power dividers are combined with the newly developed compact SIW t-junctions to form the feed network for one polarization, hence six combining stages per polarization are required.

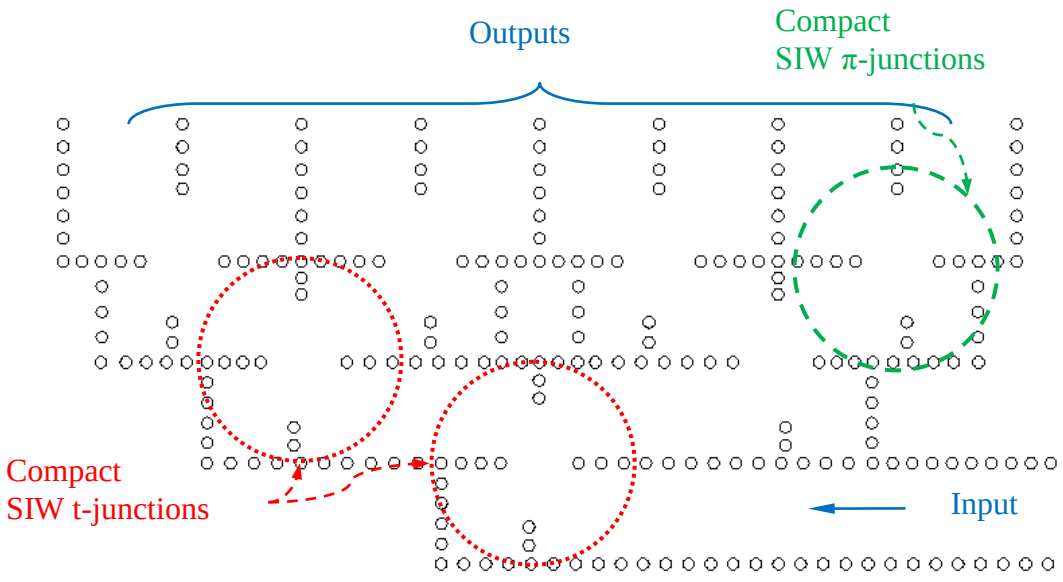

Figure 5.19 1 to 8 binary power divider structure based on compact SIW junction designs

This feed network will be eventually folded to the back of the radiating elements to provide further size reduction. Hence the width of the feed SIW guides has been reduced to about 11.2 mm. According to the design guide lines given in section 4.1.5, both conductor loss and dielectric loss increase upon reducing the width of the SIW guide. Therefore, it is anticipated to incur extra loss by as much as 0.45dB/m for this size reduction, which will account for a total of 2.95dB/m. In addition, when adding two more combining stages to feed the 64 radiating SIWs, the overall feed lines' length will approach 1m, and hence will cause noticeable antenna efficiency degradation.

Finally, a 64 radiating SIW slot array structure has been fabricated [31], as shown in Figure 5.20, and when compared to the 16 radiating SIW sub array design (shown in Figure 5.6), the number of the radiating elements are four times more. But in this case, the size of the feed network is greatly reduced due to the utilization of compact junctions and relatively narrower SIWs. However, after increasing the number of radiating SIWs to 64, the loss of the feed network has significantly increased to a point that further lateral expansion of the array size will give marginal gain increments; i.e. we reach the point of no return. In order to compensate for the feed loss and to establish an adequate receiver noise figure, it is required to add LNAs before combining more of these SIW slot sub-arrays.

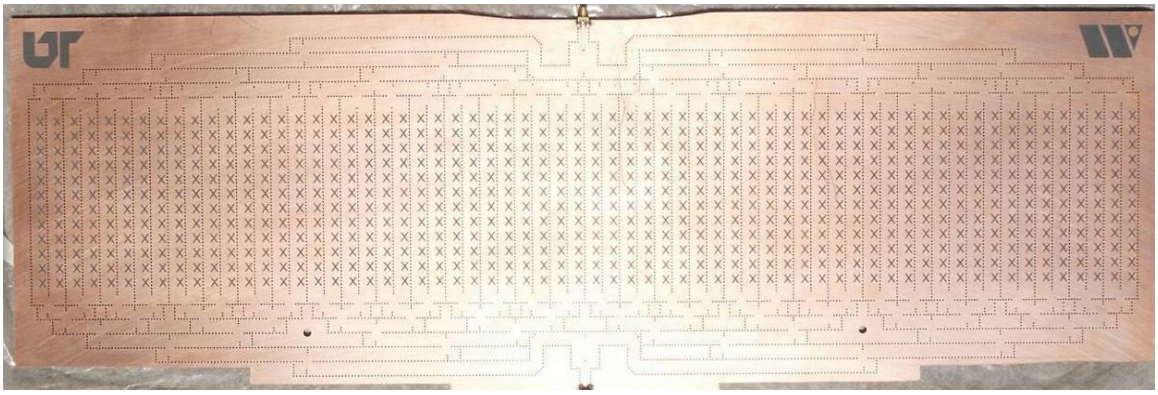

Figure 5.20 Fabricated 64 radiating SIWs slot array antenna prototype

5.3.2 Full Array Measurement Results

The measured return and termination losses are shown in Figure 5.21, and they indicate that a wider bandwidth has been achieved upon using the SIW junctions with the narrower "a" dimensions. In addition, the radiation patterns of these fabricated full arrays have been measured using near-field measurement set up and the measured LHCP radiation patterns at 12.2, 12.45 and 12.7GHz are shown in Figure 5.22, Figure 5.23 and Figure 5.24 respectively.

It is important to recognize here that the array has a size of 34 inches by 11 inches, which is too large for our PCB manufacturer to build in one step. So, the images had to be flashed twice, which may have caused slight misalignment between the left and right halves of the slot array. Unexpected side lobes (as seen in Figure 5.22(a)~Figure 5.24(a)) are spotted in all the measured azimuth cuts, which are most likely caused by this misalignment. The full SIW array is two large for the near field range to measure as well, and the antenna has to be physically bore-sighted to conduct these measurement, which is the reason why all the elevation plots have the peak radiation at 0° rather than 45 °.

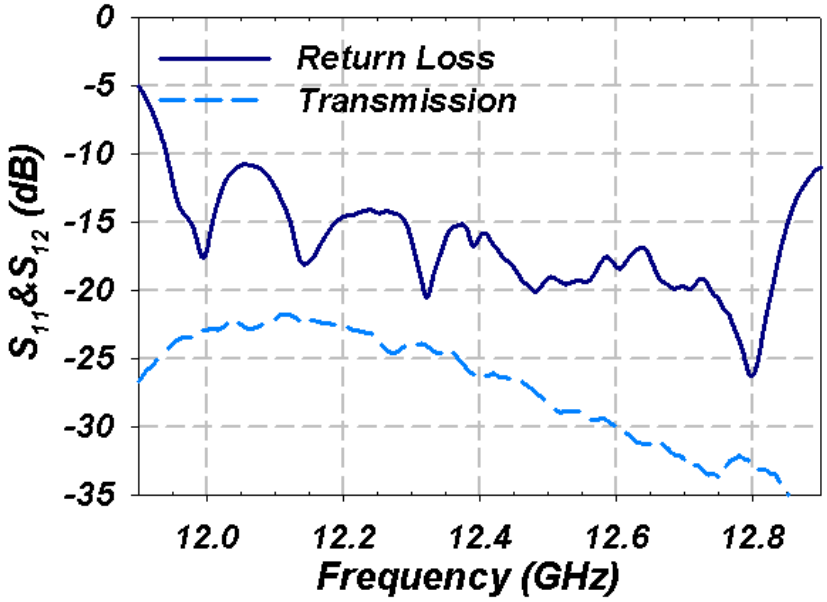

Figure 5.21 Measured return and termination losses of the 64 radiating SIW full array

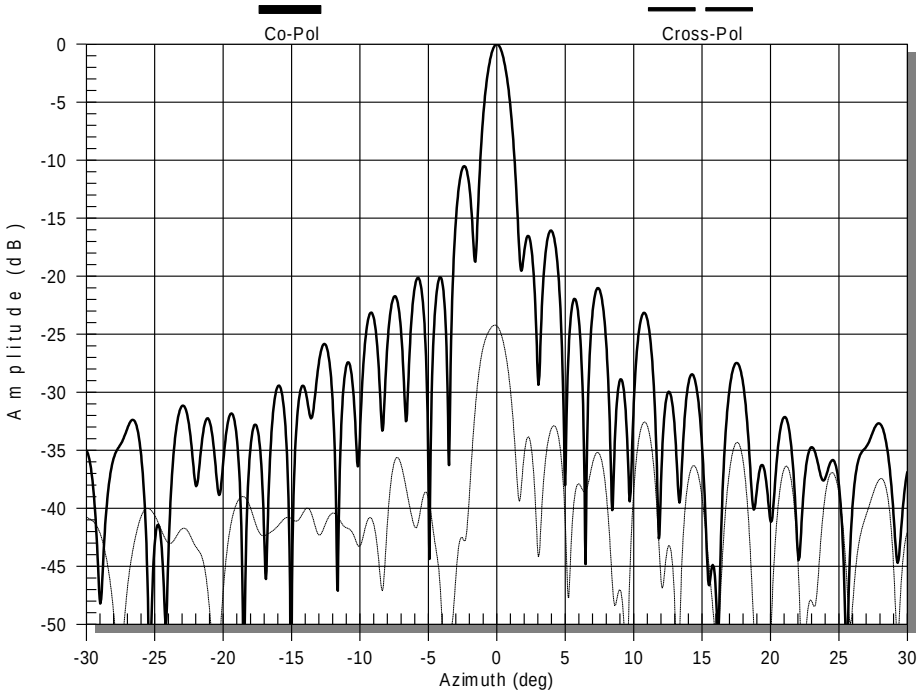

(a) Azimuth cut

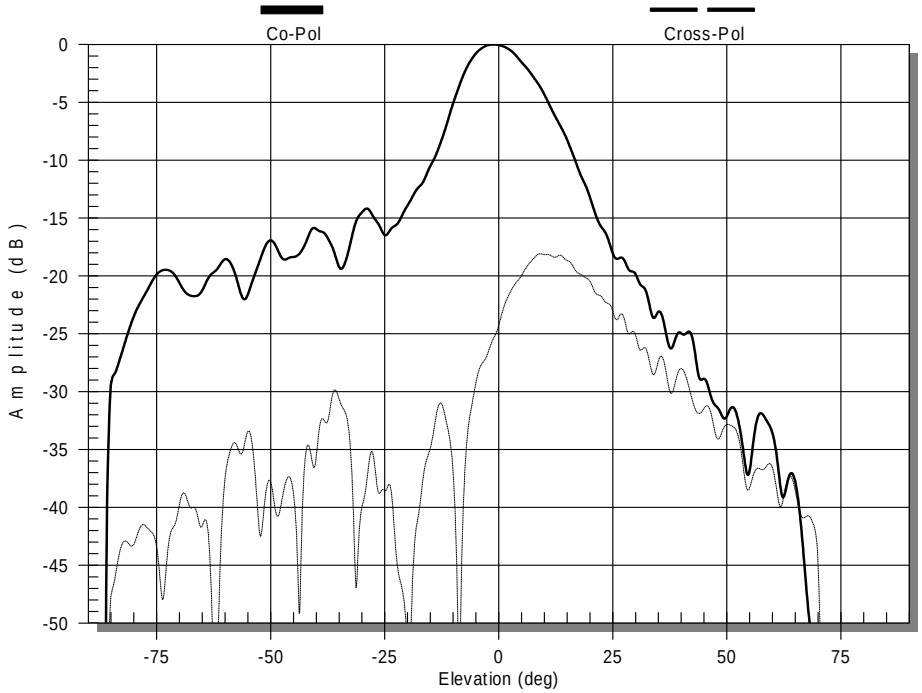

(b) Elevation cut

Figure 5.22 Radiation patterns of the 64 radiating SIW full array at 12.2GHz

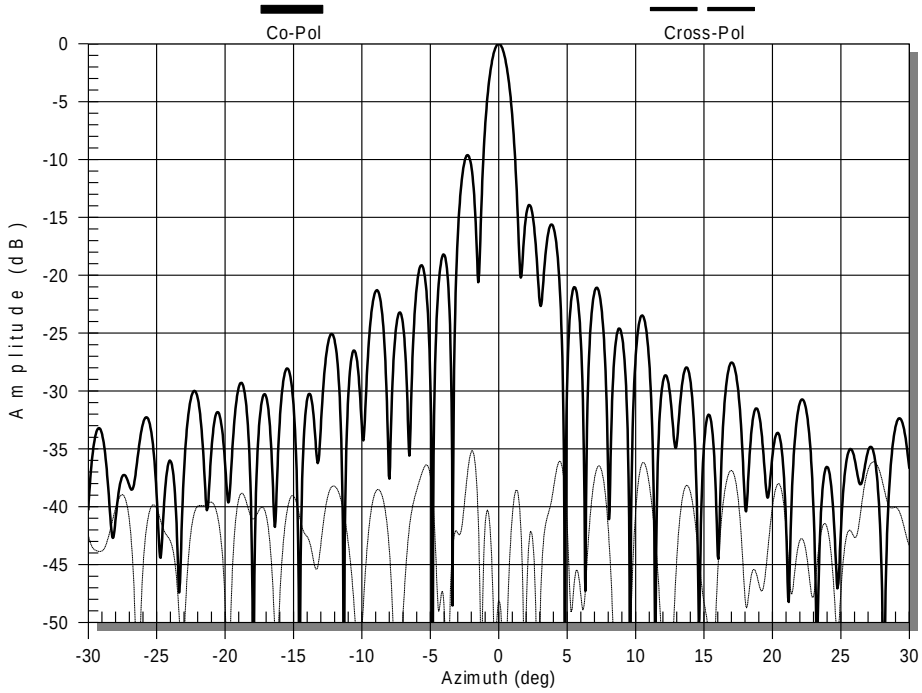

(a) Azimuth cut

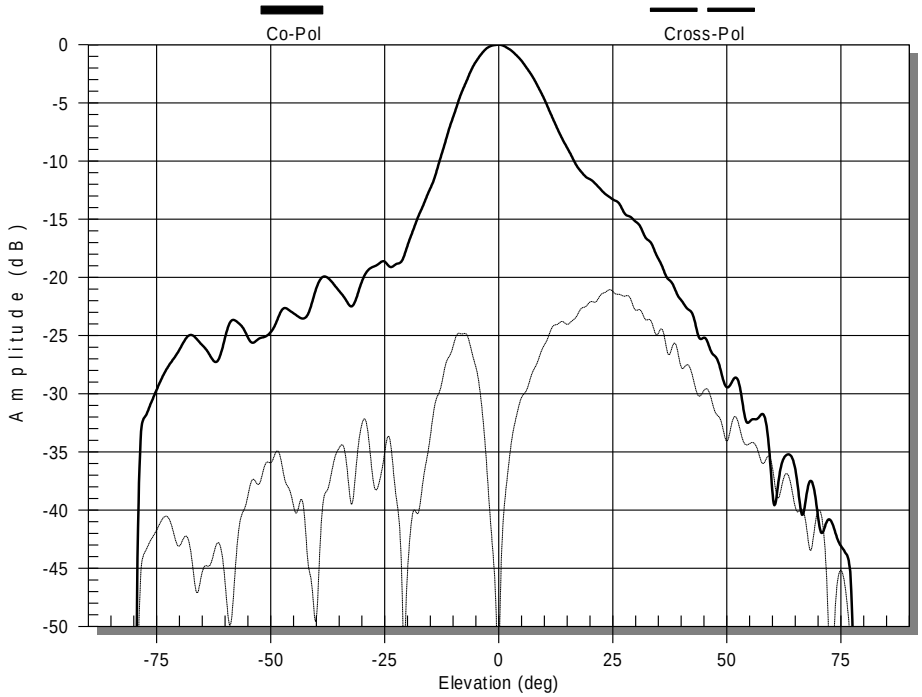

(b) Elevation cut

Figure 5.23 Radiation patterns of the 64 radiating SIW full array at 12.45GHz

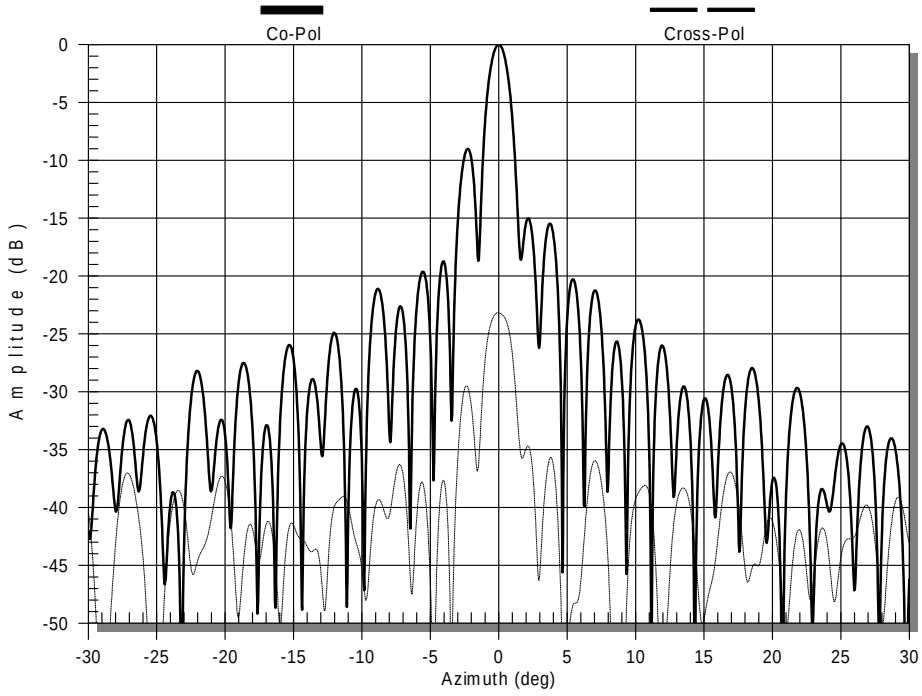

(a) Azimuth cut

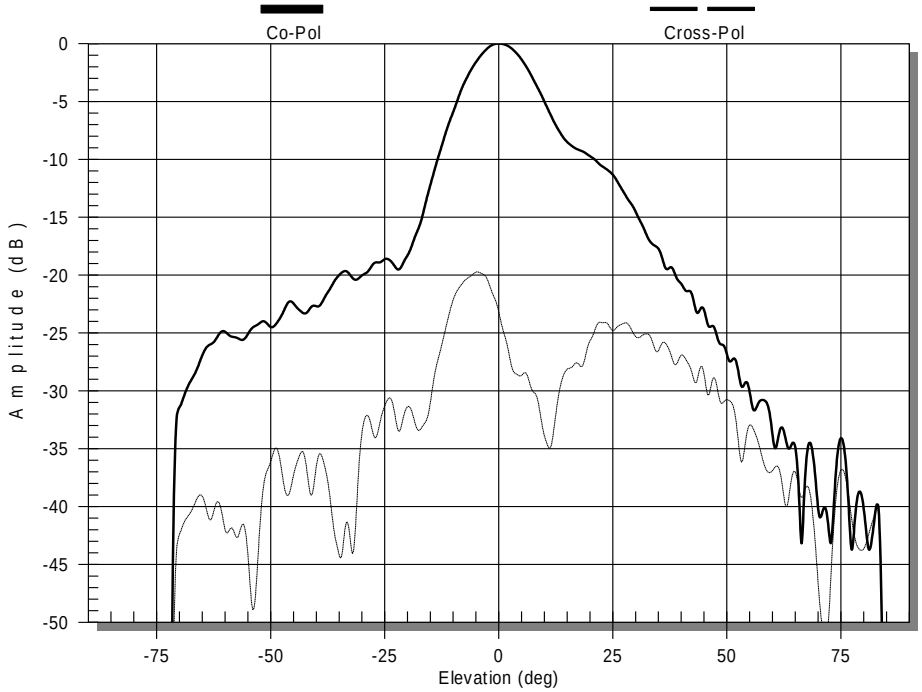

(b) Elevation cut

Figure 5.24 Radiation patterns of the 64 radiating SIW full array at 12.7GHz

In the azimuth cut, a very narrow beam is measured while in the elevation cut a wider beam has been measured, since fewer elements are used and as expected. The measured radiation performance of the full array is listed in

Table 5-5, where an excellent axial ratio performance at the center frequency is demonstrated. The side lobe levels are significantly reduced by the tapering of the slot lengths when compared to the uniform slot length SIW sub-array design. At the center frequency, the beam tilt angle is slightly off the 45° designed value. Similar to the measured results of the sub-array, a frequency dependent beam squint has been observed here as well for the full array. Approximately a 28 dBi gain has been achieved. The loss of the feed network is around 3dB, which is very close to the predicted insertion loss values according to the design charts detailed in section 4.1.5. Similar results were measured too for the RHCP case as well. Comparing the gain of the SIW sub-array and

this SIW full array, a gain improvement of roughly 3 dB is achieved for approximately 4 times the size, which indicates that a significant drop in the antenna efficiency is due to the accumulative feed network insertion loss. So, for the next design example, the main focus is to improve the efficiency of the feed network.

5.4 Double Layer Folded Feed 32 Radiating SIWs Array

Previous array implementation shows that increasing the array gain by expanding it laterally to 64 radiating SIWs has improved the gain but also has caused significant drop in antenna efficiency due to the increasing effective length and loss per unit length of the feeding network. So in this folded feed array design, the number of radiating SIW elements has been reduced to 32 again, which eliminates one stage of the binary feed network.

Table 5-5 Measured Radiation Performances of the 64 radiating SIW full array

Frequency	Polarization	Peak Gain (dBi)	Elevation Peak (deg)	Sidelobe level (dB)	Cross Pol level (dB)
12.2GHz	LHCP	27.27	49.1	-14	-24
12.45GHz	LHCP	27.98	43.7	-18	-56
12.7GHz	LHCP	28.13	36.6	-18	-24

The length of each radiating SIW is also increased to 7 inches (1 inch for transitions and 6 inches for the radiating slots), to allow wider and less loss SIWs to be used in the folded feed network. As described in section 5.2, the optimum number of "X" shaped slots is 13 in this case, and the synthesized values for optimum slot distribution are used here as well.

As described earlier, a five stage binary feed network consists of compact SIW junctions has been implement for the development of the 32 radiating SIWs folded feed array design. The fabricated combining network is shown in Figure 5.25. Where the insertion loss of the feed network has been reduced upon tapering, the widths of the SIWs at each combining stage such that the stage with the longest transmission line has the widest SIW

"a" dimension, which in turn gives the lowest insertion loss per unit length according to section 4.1.5.

5.4.1 Folded feed network development

The developed combining network is connected back to back as shown in Figure 5.25, and its measured results are shown in Figure 5.26, where a good return loss is achieved and the measured back to back insertion loss is less than 1.5 dB across the DBS band. The feed network is folded to the back of the radiating elements to provide significant size reduction (about 50%). At the end of each output SIW, a transition between the two SIW layers, as discussed in section 4.3.4, is used to couple the feed network to the radiating waveguides.

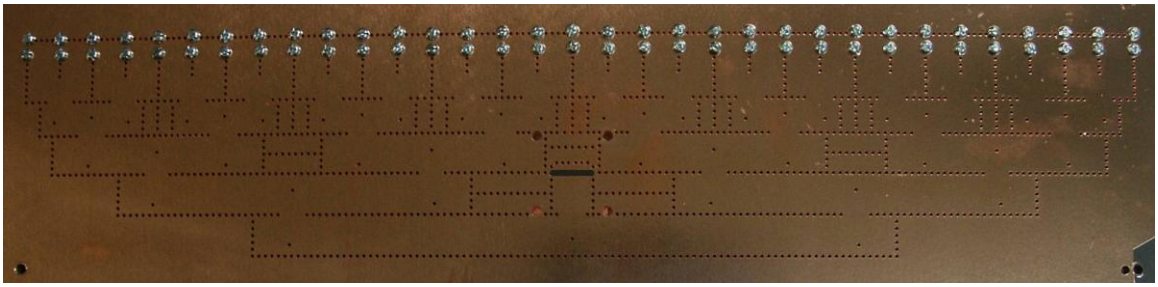

Figure 5.25 Back to back connected feed network of SIW 1 to 32 feed networks

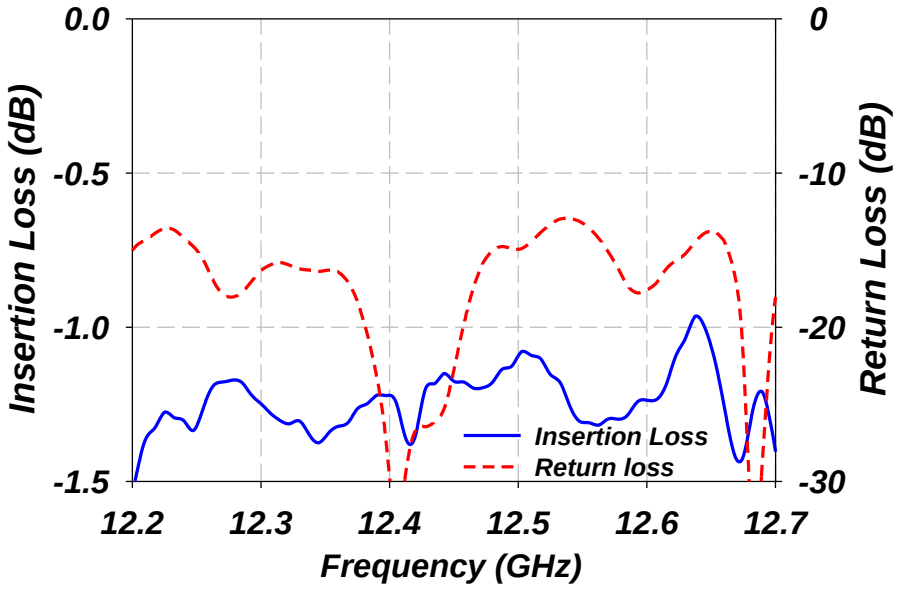

Figure 5.26 Measured return & insertion loss of back to back 1 to 32 feed networks

5.4.2 Measurement Results

The fabricated array with the folded feed network is shown in Figure 5.27 [32] with its measured return and termination losses are shown in Figure 5.28. The radiation patterns of the fabricated arrays have been evaluated over the 12.2 GHz to 12.7 GHz frequency range using near-field measurements and are shown in Figure 5.29 through Figure 5.34. A summary of the measured radiation characteristics are listed in Table 5-6. The sidelobe levels in the elevation cuts have been maintained at levels better than 17dB down from the peak radiation, which is a result of the slot length tapering. Due to the relatively highly efficient feed network, and although this folded array has only half the radiating area or a quarter of the surface area of the 64 radiating SIW full array, the gain is on the average only 1.5dB lower than that of the 64 element array. The average gain of the LHCP radiation is more than 26.3 dBi and the RHCP gains are slightly lower, which is most likely caused by misalignment between the radiating SIWs and the feed network during assembly. However, these gain levels should be high enough to lock the DBS signal and obtain a decent reception of the satellite TV programs in Knoxville area. Field tests of the folded feed slot array will be discussed in the next section.

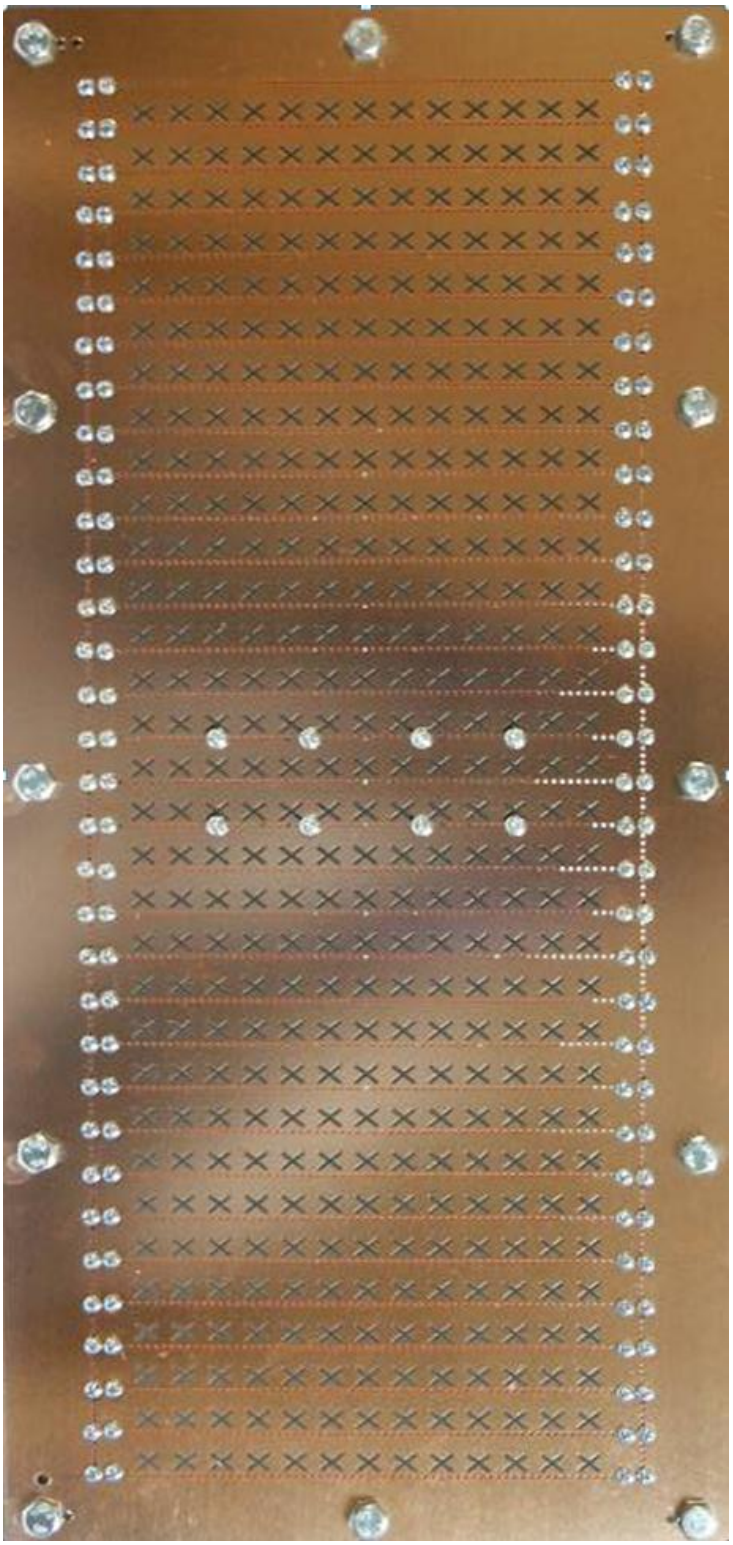

Figure 5.27 Fabricated 32 radiating SIWs slot array with folded feed networks

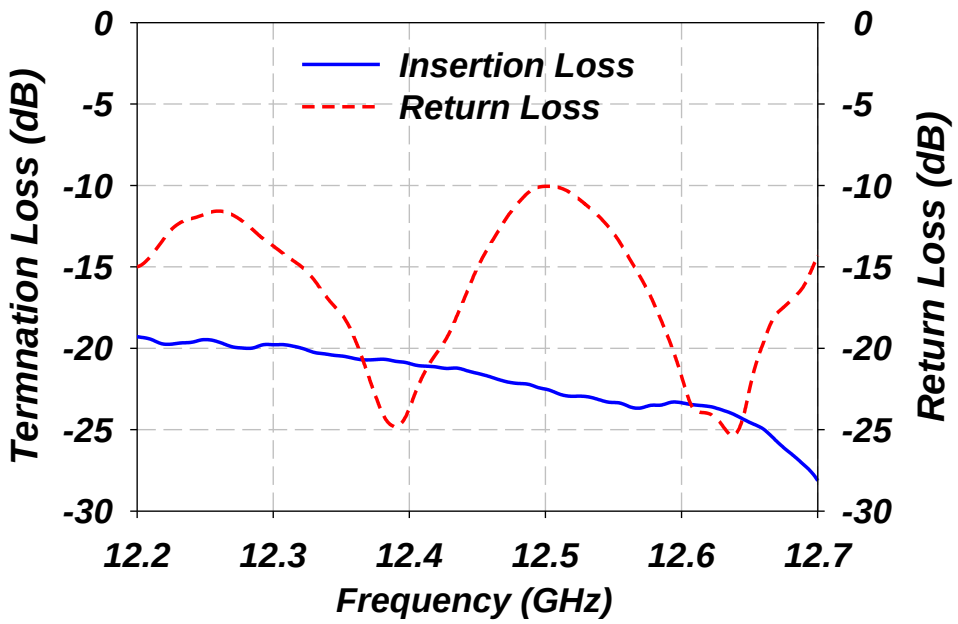

Figure 5.28 Measured results of the slot array with folded feed networks

Table 5-6 Measured results for the 32 radiating SIWs array with folded feed network

Frequency	Polarization	Peak Gain (dBi)	Elevation Peak (deg)	Sidelobe level (dB)	Cross Pol level (dB)
12.2GHz	LHCP	26.07	49.9	-17	-18
12.45GHz	LHCP	26.52	42.3	-18	-33
12.7GHz	LHCP	26.43	34.7	-18	-27
12.2GHz	RHCP	25.87	-50.2	-17	-14
12.45GHz	RHCP	26.17	-43.9	-18	-19
12.7GHz	RHCP	26.14	-36.5	-19	-20

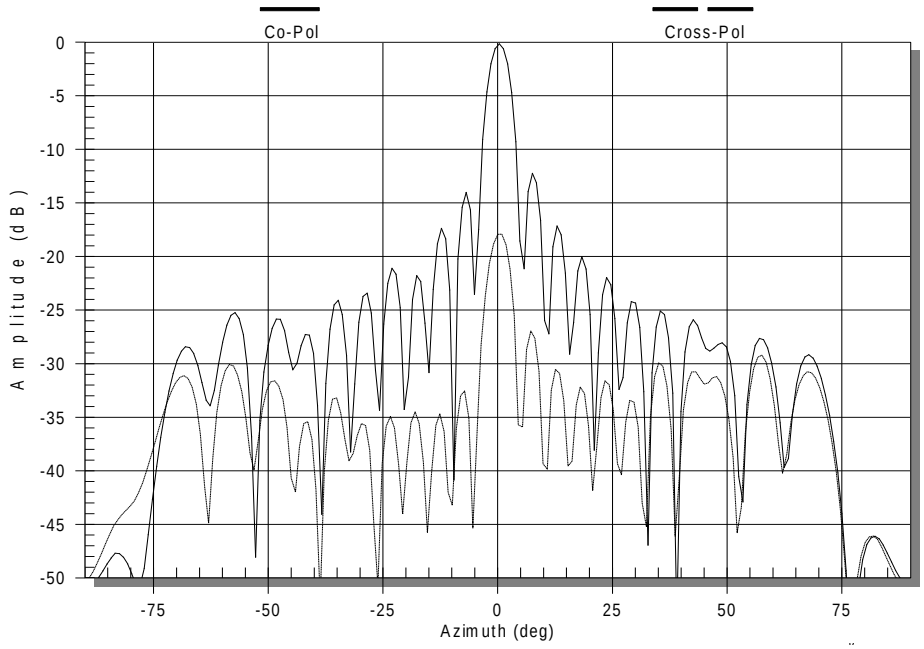

(a) Azimuth Cut

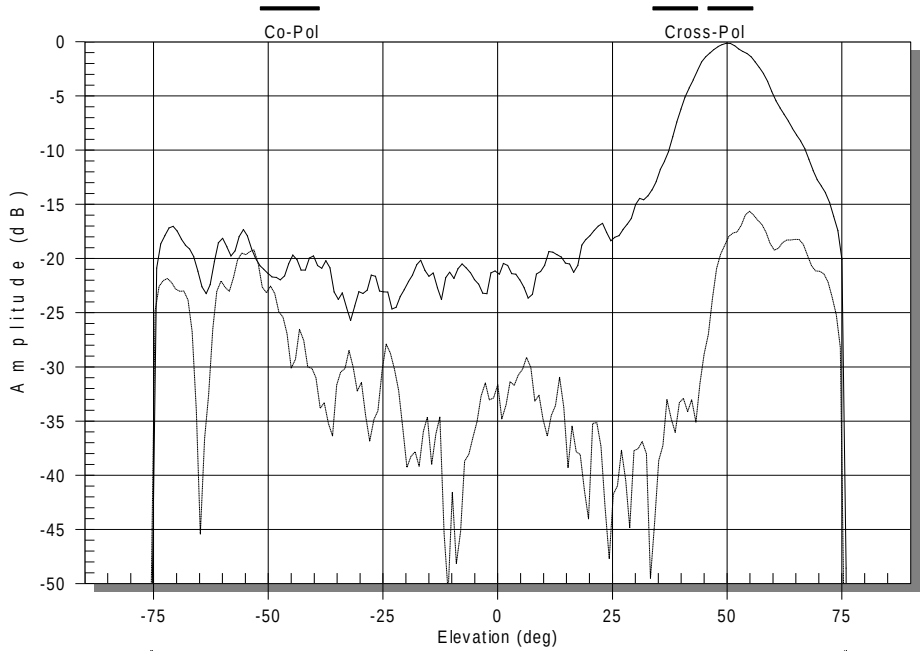

(b) Elevation Cut

Figure 5.29 LHCP Radiation patterns of the 32 radiating SIWs slot array with folded feed networks at 12.2GHz

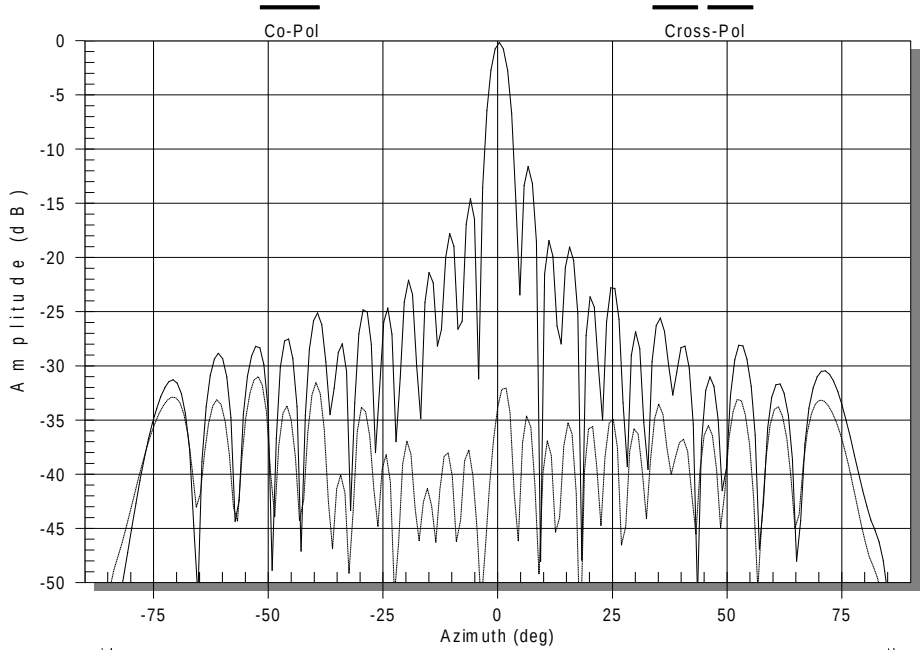

(a) Azimuth Cut

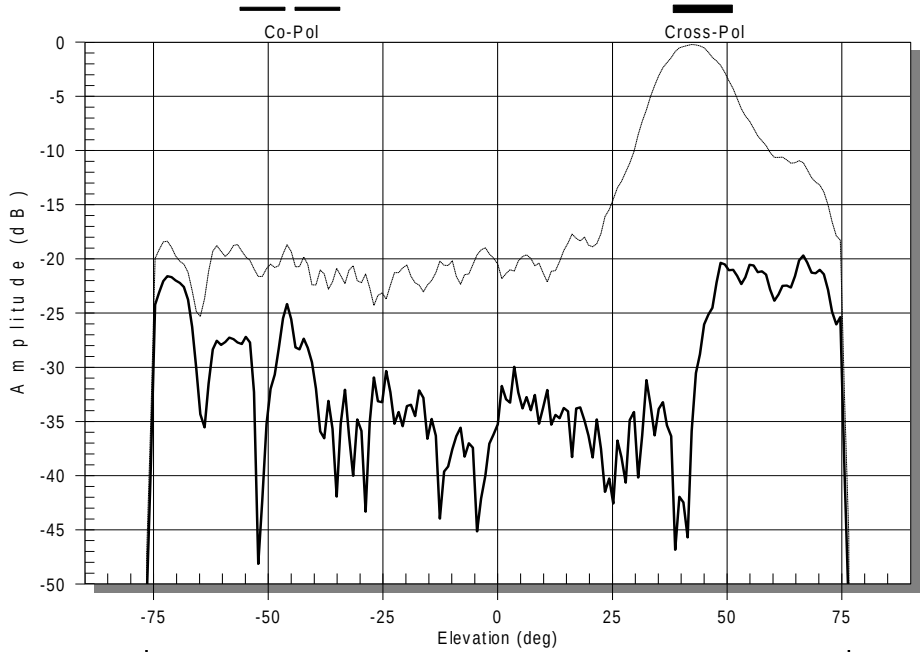

(b) Elevation Cut

Figure 5.30 LHCP Radiation patterns of the 32 radiating SIWs slot array with folded feed networks at 12.45GHz

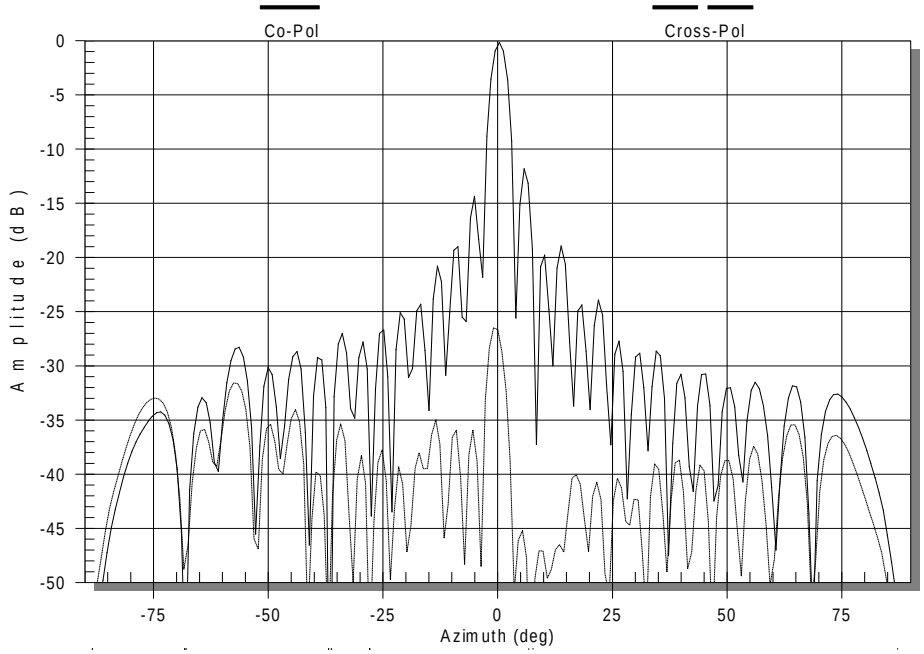

(a) Azimuth Cut

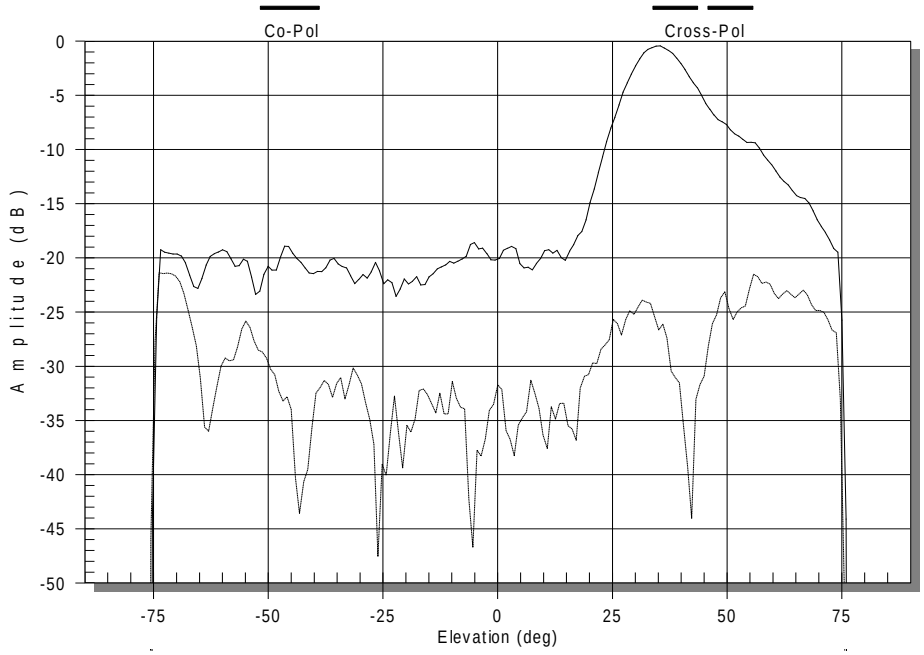

(b) Elevation Cut

Figure 5.31 LHCP Radiation patterns of the 32 radiating SIWs slot array with folded feed networks at 12.7GHz

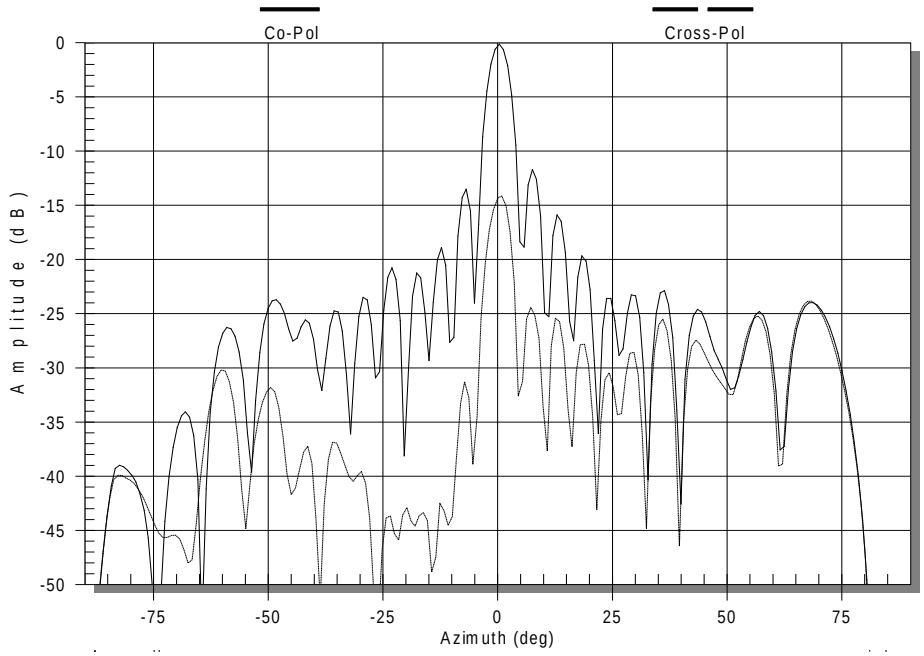

(a) Azimuth Cut

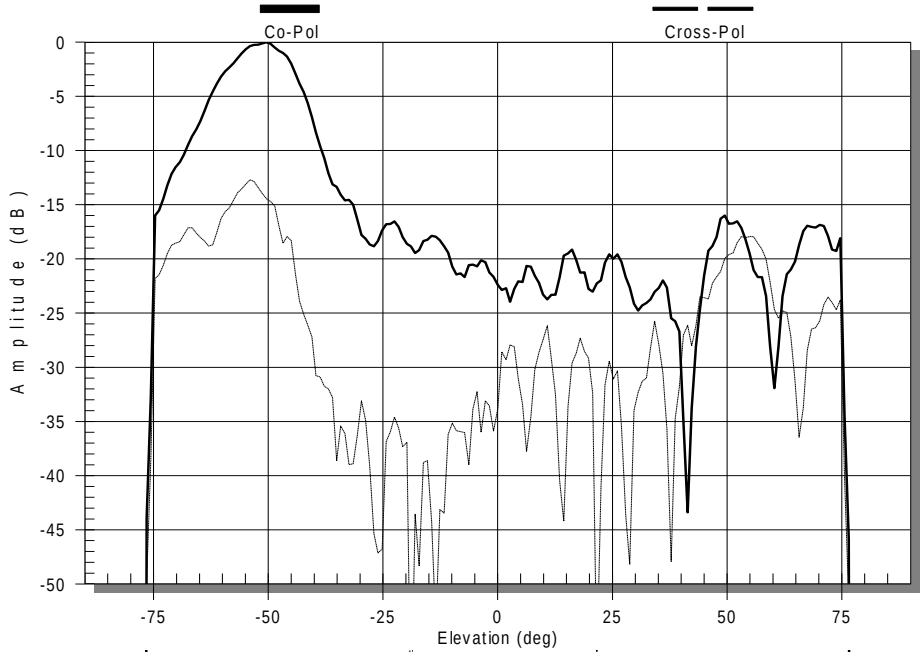

(b) Elevation Cut

Figure 5.32 RHCP Radiation patterns of the 32 radiating SIWs slot array with folded feed networks at 12.2GHz

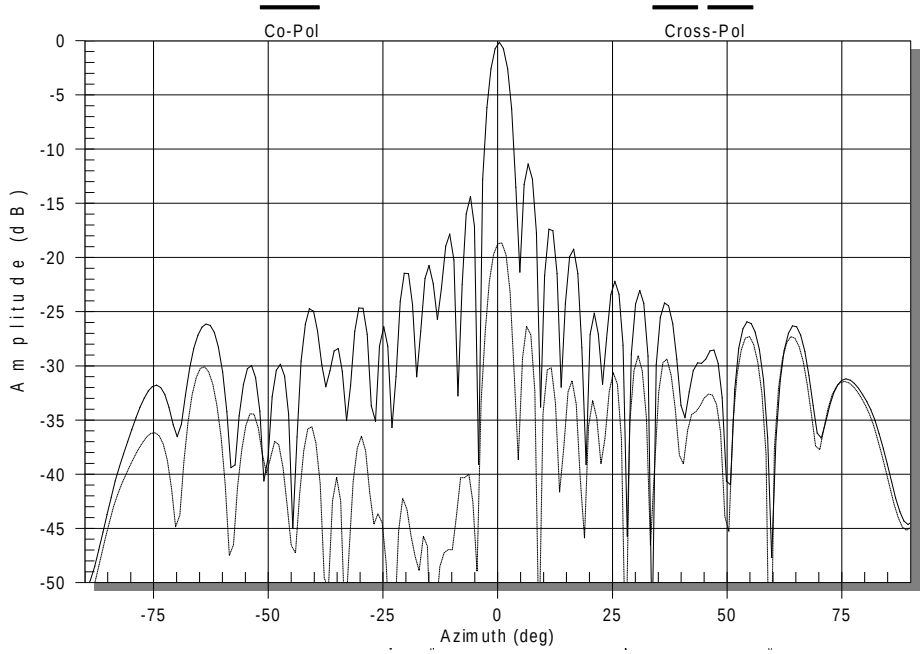

(a) Azimuth Cut

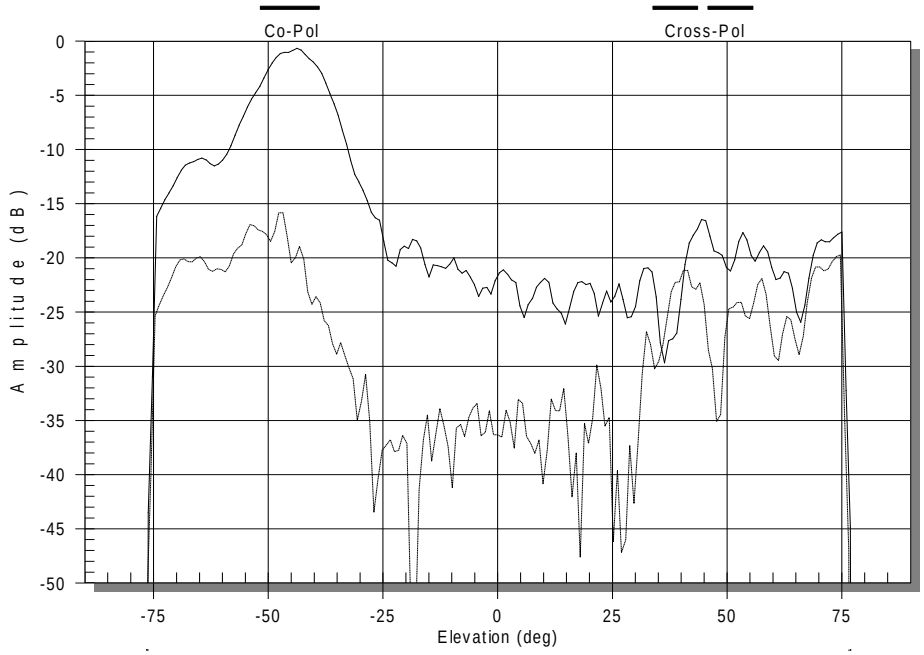

(b) Elevation Cut

Figure 5.33 RHCP Radiation patterns of the 32 radiating SIWs slot array with folded feed networks at 12.45GHz

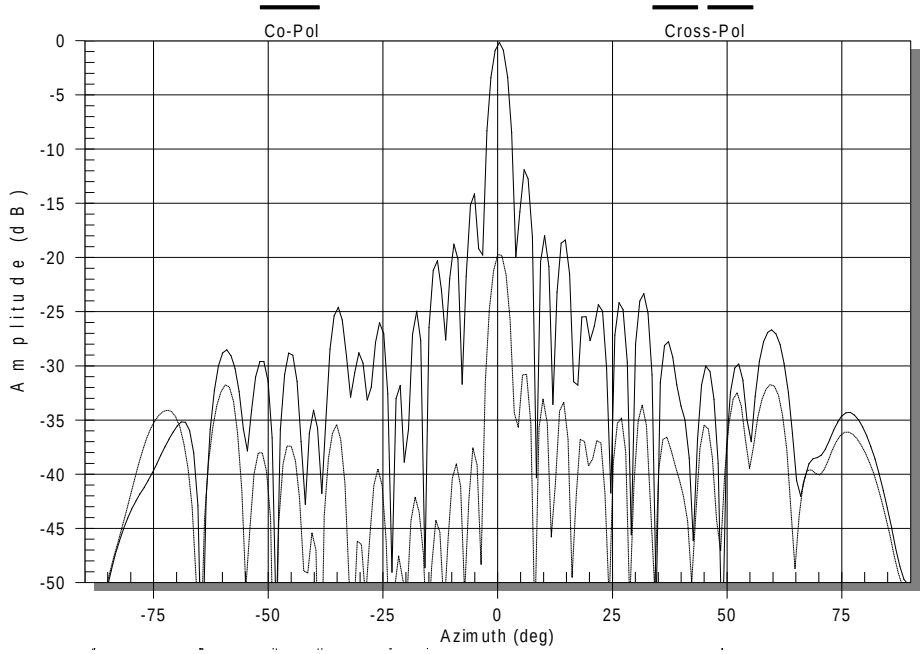

(a) Azimuth Cut

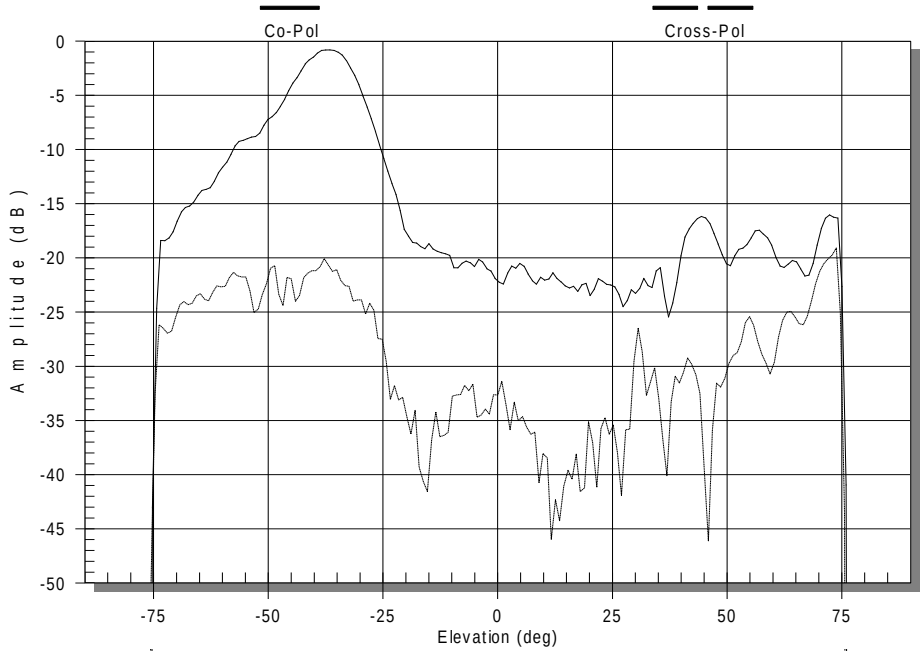

(b) Elevation Cut

Figure 5.34 RHCP Radiation patterns of the 32 radiating SIWs slot array with folded feed networks at 12.7GHz

5.4.3 Field Tests

Field tests were carried out using the 32 radiating SIWs slot array antenna with a folded feed network in Knoxville area. The reception quality of the DBS signal from three major satellites including: Direct TV 101°W, Echo Star 110°W and 119°W, were tested under various weather conditions. The slot array antenna prototype was always able to lock the satellite signal under sunny, cloudy and even slightly rain conditions. One typical set of signal strength measurement result is shown in Figure 5.35.

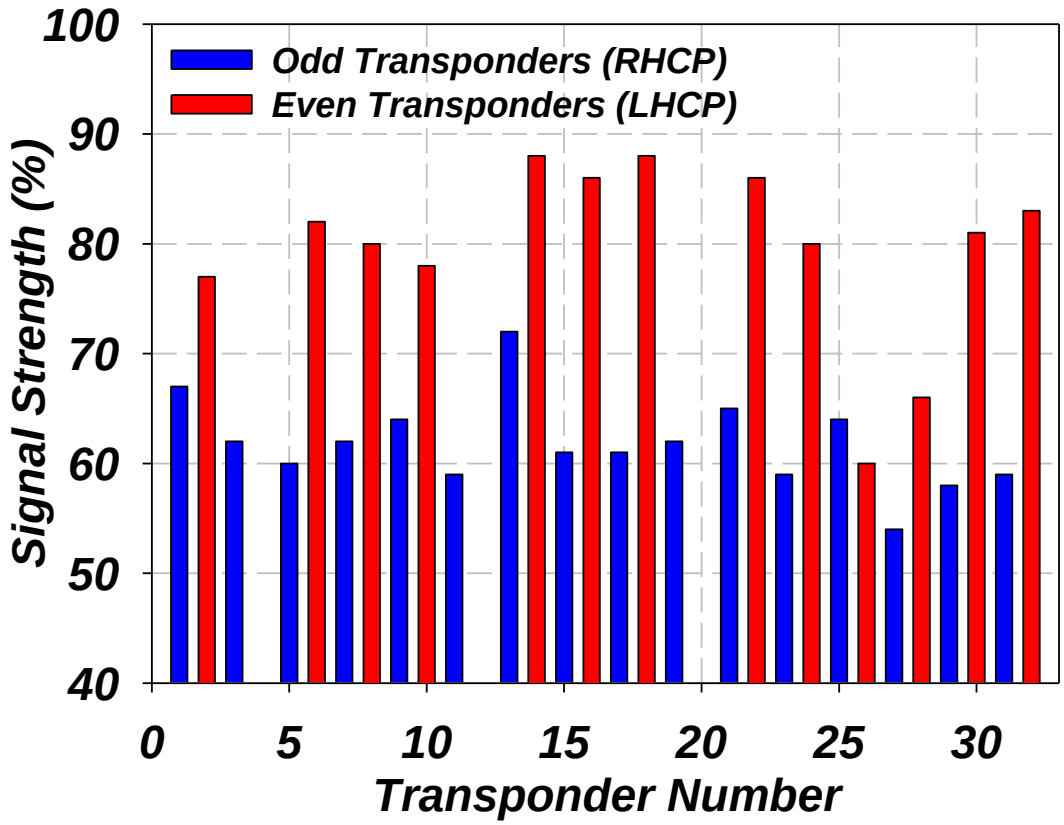

Figure 5.35 Received signal strength from satellite with slot array prototype.

This set of results is measured one early afternoon on a sunny summer day. While, an LNB with WR75 interface was first attached to the output of the slot array prototype with the folded feed. Then the antenna was manually pointed to the 101°W satellite and the signal strength readings from a Direct TV receiver box (connecting to the LNB output) has been recorded. The receiver box is usually able to lock the satellite signal if the signal strength is over 40%. In our case, TV programs from all the available transponders can be successfully decoded. The information in the even transponders id carried by the LHCP signals and the odd transponders uses the RHCP signals. The field test results also indicate that the LHCP gain of the slot array prototype is usually higher than the RHCP gain. This is consistent with the near field measurement results. However, the measured results with an 18 inch reflector antenna always has a signal strength closer to a 100%, which indicates that the gain of the developed slot array prototype is far from being able to offer the same Quality of Service or rain margin as the traditional 18 inch satellite dish. Therefore, 2-4 of these 32 radiating SIWs slot sub-arrays need to be combined in phase after LNA stages, in order to achieve a higher reliability and an acceptable C/N ratio in more reception areas.

5.5 Conclusion

Slotted SIW array antennas utilizing emulated waveguide feed structures should have lower insertion loss when compared to planar printed antennas. They are easy to manufacture, have light weight, and their use should lead to a lower cost product as well. While their alternative, the metallic rectangular waveguide, requires high manufacturing tolerances, bulky, heavy in weight, and is expensive to build. SIW slot array antennas can be fabricated using standard printed circuit board processing. Even though, the developed slotted SIW sub-array antenna has a slight lower efficiency as compared to its metallic waveguide counterpart, but has demonstrated significant improvement in terms of fabrication cost, weight and design flexibility.

A synthesis procedure for the radiating SIW design is introduced, where the optimum slot parameter combination and number of slots per radiating SIW can be derived by evaluating the beam tilt angle and slot coupling factors numerically using a very approximate step-by-step approximate recipe. Slot lengths tapered with optimum distribution can provide almost the same gain and significant improvement in side lobe levels as compared to the uniform slot array. Two radiating SIW configurations with 12 and 13 "X" shaped slots have been designed for both single layer and folded slotted SIW arrays.

The developed full array prototype with the 64 radiating SIWs and 12 "X" shaped slots has demonstrated the highest gain among all developed prototypes. But its efficiency is much lower due to the long lossy feed networks. A 25% size reduction of the full array can be achieved by reducing the radiating SIWs to half and fold the feed network to the back of the radiating slots. The feed networks of this multi-layer slot array with a 32 radiating SIW can be strategically tapered to maximize the antenna efficiency. As the array with the optimum gain and efficiency combination among the developed prototypes, the 32 radiating SIW folded feed array is capable of receiving DBS TV broadcasting in Knoxville area, however, with low gain margin. The DBS antenna reliability can be improved by combining two or more parallel apertures and embed LNAs after each sub-array to assure high C/N levels. Hence, the reported slotted SIW array design could lead to a low profile antenna (< 3in height) upon folding the feed structure, and will surmount to over 30 dB gain when combining parallel apertures as discussed in [33].

Chapter 6

Antenna Design Challenges of Multi-Radio Mobile Devices

In an effort to increase the functionality of the current wireless terminals and improve their quality of service, we have investigated alternative concepts of multi-band antennas as well as the merits of using reconfigurable antennas or extending these multi-band antennas to be reconfigurable as well, i.e. a hybrid. The study included the analysis of various reconfigurable and multi-band structures such as loop, monopole, PIFA, and combinations. Developed reconfigurable structures have been aimed at serving one band at a time. However, their use has always been hindered by the need for a large number of switches and complicated DC bias lines. A hybrid reconfigurable multi-band antenna is a new concept that has recently evolved and should become a viable alternative to the currently popular multi-band antenna.

In this chapter, reconfigurable antenna concept will be introduced. Antenna design challenges of multi-radio wireless devices will be discussed, followed by a comparison between various antenna options. In following chapters, we will describe various reconfigurable antenna designs including a reconfigurable "Maze" (fractal loop) and "mini-Maze" (bent monopole) antennas in Chapter 7 and reconfigurable multiband antennas for both mobile handsets and laptops in Chapter 8.

6.1 Introduction

Wireless services are significantly increasing at a remarkably speedy pace with services allocated at a wide range of operating frequency bands. Moreover, these services have sharply different specifications/standards while the types of service-band numbers are vastly increasing. However, current mobile devices are designed to address more than one band/service at a time. Unquestionably, using individual antennas to receive all these services is not feasible because of the devices' size constraints -- albeit dedicated individual antennas could provide the best performance. Meanwhile, multi-band antennas are currently the most practical and affordable solution. They are compact, easy to design, and offer better performance than Ultra Wide Band (UWB) antennas due to their signal selectivity and out-of-band noise rejection capabilities. Nevertheless, some of these operational frequency bands are not constantly utilized, therefore, it can be appropriate to investigate the feasibility of dynamically turning off some of these services, i.e. reconfiguring the antenna structure to improve their unwanted signal rejection. Additionally, multi-band antennas are generally followed by a bank of filters, which are required to reject all unwanted bands. These filters are expensive, and bulky as a result of their very stringent specifications and high Q requirements. The use of reconfigurable antennas here can help in augmenting these two functions, by acting as an antenna as well as a filter, or at least helping to relax their stringent specifications.

Reconfigurable antennas, in the meantime, have been extensively investigated for various sorts of applications, yet they are still not widely used. Their cost, reliability, and DC power consumption are still major factors that prevent a wide usage. Reconfigurable concepts have great potential, can be extremely valuable, and can comprise a significant impact by improving a system’s performance, reducing its cost, and addressing related size constraints by reducing any redundancy and integrating various functionalities.

In searching for plausible implementation, we have extensively pursued various topologies that led to various alternative solutions. Recently, a new concept has evolved

that could have great impact. The hybrid approach based on reconfiguring the multi-band structures, which requires a small number of switches, simpler filter requirements, and could simultaneously provide both fixed and switchable services.

In the following chapters we shall outline our efforts of (1) separating the resonances of various potential multi-band antennas structures to form switchable single band antennas, and (2) combining several single band structures to construct an antenna that can be switched between several multi-band states. The goal is to dynamically control the antenna topology, to make it solely dedicated to one frequency band at a time, in order to achieve better performance. Subsequently, we shall provide reconfiguration capabilities to these multi-band structures and construct reconfigurable multiband antennas where advantages of both the single band reconfigurable antenna and the multi-band antennas are combined and enhanced.

6.2 Design challenges of Multi-band Antenna

Along the development of multi-radio mobile platforms, such as laptops, smart phones, etc., there is a need to address several wireless services over a wide frequency range using several wireless modules on the same device. This can be achieved by using many individual antennas, multi-band antennas, or -- as we are proposing here -- reconfigurable antennas. All of these approaches have their advantages and disadvantages which are summarized in Table 6-1.

Although the multi-band antennas are mostly used in current mobile device, they face serious challenge as more and more wireless services are packed into ever smaller devices. Take the laptop computers for example, as shown in Figure 6.1, radios are being added to the system as a wireless module. Due to the fast proliferation of radios in mobile platforms, it is expected to have more than 6 radios by 2009. On the antenna side, each one of these wireless module may support more than one frequency band of the same service (as shown in Table 6-2), and most of the modules require 2 antennas for diversity

and some need as much as 3 antennas for Multi-Input-Multi-Output (MIMO) operation. So, even for multi-band antennas, the laptop computer will soon run out of space for antennas, not even to mention devices with smaller form factors such as smart phones.

As a result, the antennas from different wireless modules will need to be packed next to each other, which causes very poor isolation between radios, and could lead to a failed connection when multiple radios are operating simultaneously. This is primarily caused by the close spacing and the low out of band rejection of multi-band antennas. On the contrary, the isolation between radios will be greatly improved if reconfigurable antennas are used, due to the high out of band rejection in the single band reconfigurable antenna case or the loosened spacing in the reconfigurable multiband antenna case.

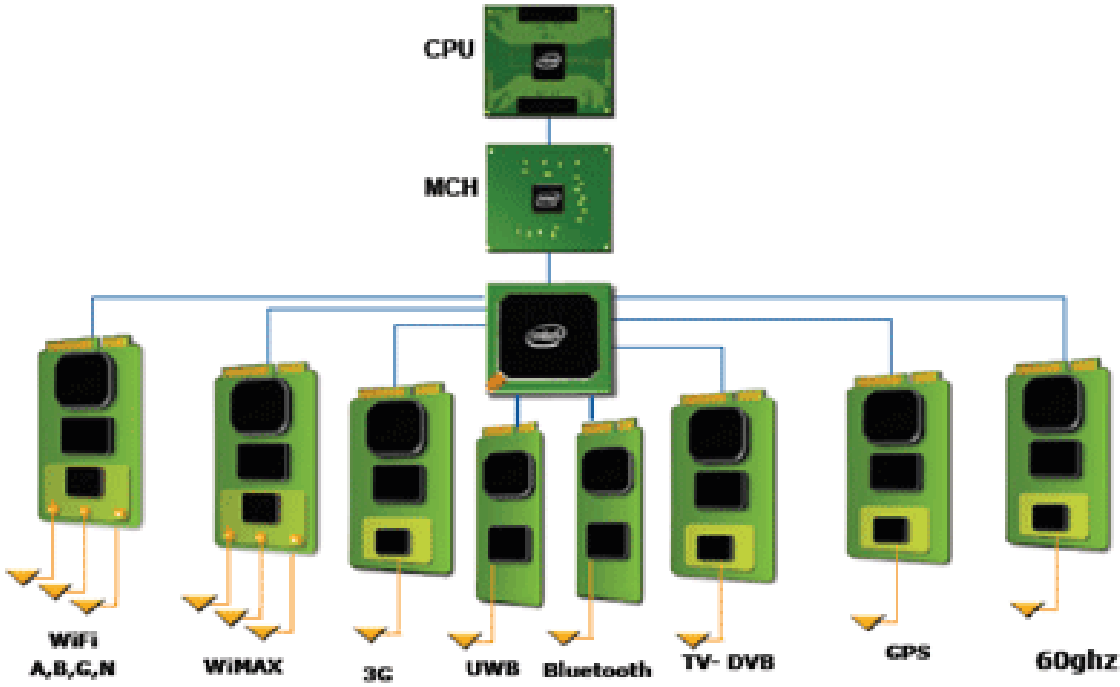

Figure 6.1 System diagram of Multi-Radio laptop. (Source: Intel Developer Forum, 2007)

Table 6-1 Comparison of Antenna Solutions for Wireless Mobile Platforms

	Multiple Antennas	Multi-band/Wide-Band Antennas	Reconfigurable Antennas
Usage Model	Single band antenna supports one frequency band of a wireless service	One antenna supports all frequency bands of a wireless service/module	One antenna supports may wireless standards
Number of Antennas	Frequency bands * Services * Diversities	Wireless Modules * Diversities	Diversities (such as main/aux or MIMO)
Space Requirement	Lots of antennas require lots of spaces	Reduced space requirement but wide bandwidth requirements contradicts miniaturization efforts	Minimal space requirement
Front-end Complexity	Loose filter specs, simple front-end	Many stringent filters required, introduces high insertion loss	Released filter specs, require reconfigurable front-ends
Individual Radio Performance	Excellent	Good, lower receiver sensitivity due to insertion loss of front-end, i.e. diplexer	Acceptable performance, additional loss introduced by switches
Radio Coexistence	Little spacing between antennas, strong coupling between radios	Poor out of band rejection, suffer from noise jamming caused by transmitted signal of other radio(s)	Degraded simultaneous operation performances as antenna support one service at a time
Cost	Increased number of cables contributes to most of the cost	High cost stringent filters required in the front-end	The cost of low loss, low power consumption switch (MEMS) is high

Table 6-2 Frequency bands for wireless services

Wireless Services	Frequency Bands
Wi-Fi	IEEE 802.11b/g/n : 2.4GHz~2.48GHz IEEE 802.11a/n : 5.15GHz~5.85GHz
WiMax	IEEE 802.16: 2.3-2.4GHz, 2.5-2.7GHz, 3.2-3.8GHz, 5.15-5.85GHz
3G	GSM 850 :0.824~0.894GHz, GSM 900 : 0.88~0.96GHz DCS 1800 : 1.71~1.88GHz, PCS 1900 : 1.85~1.99GHz UMTS : 1.92~2.17GHz
Bluetooth	IEEE 802.15.1 : 2.4GHz~2.48GHz
GPS	1.575GHz
UWB	3-10GHz

In an effort to demonstrate the advantages of reconfigurable antennas relative to multi-band antennas, we have exposed a GPS receiver to a jamming signal. The first set-up had the receiver connected to a multi-band antenna while the second set-up had the receiver connected to a reconfigurable antenna. The utilized multi-band antenna operates at both the GPS and the 2.4GHz WLAN band, while the reconfigurable antenna supports either the GPS or the WLAN services upon reconfiguration. Both antennas have identical gain and their received signals are subjected to the same stringent filtering of GPS front-end, ergo, the resulting carrier to noise ratios (C/N) of the received GPS signals should be the same. A 20 dBm signal at 2.4 GHz, emulating a transmitted signal from WLAN radio, was then directed towards both systems. While no pronounced degradation was noticed when using the reconfigurable antenna, an over 8 dB C/N ratio drop was measured for the multi-band antenna (as shown in Figure 6.2), and likewise, the location-lock was lost. Therefore, it is evident that the multi-band antenna has poor out-of-band rejection when compared to the reconfigurable antenna, hence additional filtering is required for the antenna to attain a better noise rejection. For other radios such as Wi-Fi, WiMax and 3G, where wider bandwidths and less stringent filtering are usually required, the scenarios are even worse.

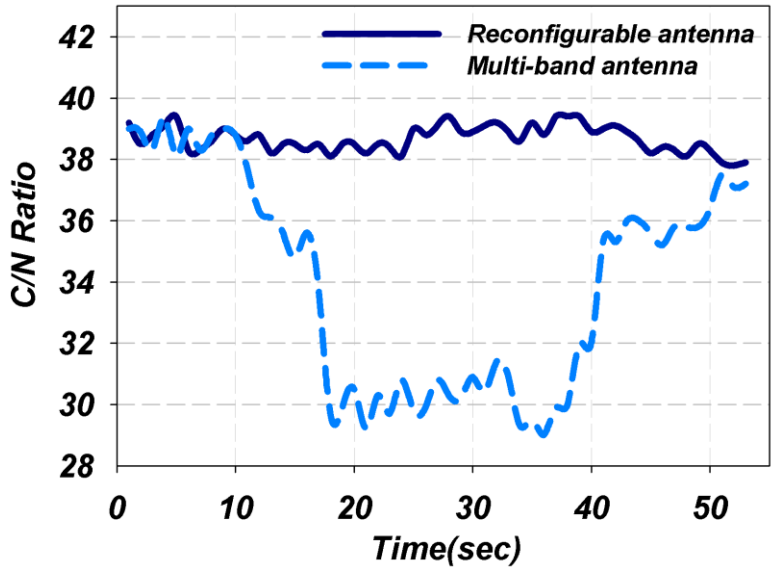

Figure 6.2 C/N Ratio of GPS module using reconfigurable and Multi-band antenna with injected 2.4GHz jamming Signal (between 10 seconds and 40 seconds)

Most multi-band antenna solutions require stringent filters that are very expensive to improve their out-of-band rejection. Reconfigurable antennas, on the other hand, have inherent band pass characteristics and generally have excellent out-of-band rejection without the use of filters. They can also have higher order resonances for such structures, but they are far away from the operating band and therefore can be easily removed with much less selective filters at an undeniably lower cost. It is essential that a fair cost comparison of these two alternatives to see the whole picture to include the cost of any required filter for both antennas.

Our effort towards developing these reconfigurable antennas will be presented in the following chapters. Initial efforts focused on modifying potential multi-band structures and turning on/off their resonances by introducing switching devices. This developed reconfigurable antennas work for one service at a time. We have also introduced a hybrid reconfigurable antenna designs approach that can combine both reconfigurable and multi-band antenna structures, examples of such hybrid reconfigurable multi-band antennas will be discussed in the following chapters.

Chapter 7

Single Band Reconfigurable Antennas for Mobile Platforms

Single band reconfigurable antennas can be controlled by switches to support one frequency at a time. As discussed in Chapter 6, they offer great flexibility and out of band noise rejection. Many concepts for designing reconfigurable antennas have been developed and their uses have been extended to include the wireless frequency bands. However, developed concepts should require the least number of switches to reduce cost, and the most compact real estate for various space constraints. Other concerns include minimal DC power consumption, where DC power is a prime concern for these mobile devices. RF Micro-Electro-Mechanical-Systems (MEMS) are the preferred switching devices due to their low DC power dissipation. However, PIN diodes and CMOS transistors are still popular and currently are used in reconfigurable antenna implementations but eventually will be replaced by MEMS whenever their prices, process compatibility, and operating voltages go significantly lower.

In this chapter, a single band reconfigurable "Maze" antenna based on fractal loop structures is first introduced in section 7.1, where switches are used to control the circumference of the fractal loop structure to render a reconfigurable resonant frequency. In section 7.2, a bent monopole antenna (Mini-"Maze") based on the reconfigurable "Maze" antenna concept is introduced. It offers a 75% size reduction when compared to

the original "Maze" and can be reconfigured between 3 single band configurations up on using only 2 switches. The implementation of MEMS switches and related modeling considerations in an antenna environment is discussed in section 7.3, followed by conclusions in section 7.4.

7.1 Reconfigurable "Maze" (Fractal Loop) Antenna

Fractal antennas [34], have pre-determined operating frequencies (i.e. the fractional resonant frequencies). These frequencies might not be commensurate with the specific operating frequencies of the different wireless services. Our developed "maze" antenna concept was conceived based on fractal ideas [35], but also utilizes switches to control the interconnectivity of the fractal structure to achieve desirable resonant frequencies. In this section, the design concept of this newly developed maze antenna is presented and it's predicted and measured radiation performances are shown in detail.

7.1.1 Design concept

With the loop antenna, we can construct very appealing reconfigurable structures by controlling its overall perimeter length for a given area: the edges of a rectangular loop could be indented to form a larger circumference, which results in a lower resonance frequency. The indentation process can be repeated at various levels, as shown in Figure 7.1(a) ~ Figure 7.4(a), to operate at relatively lower frequencies. In addition, the selected circumference loop length can be dynamically controlled by changing the various segments' interconnectivity. This control would require using multiple switches and the various loop segment dimensions could be designed to provide multiple-resonances at a well-prescribed set of frequencies. Meanwhile, their input impedances at these resonances should be effectively very similar, which is easier to match over all the supported frequency bands. Their radiation patterns should be almost the same, which is quite alluring to wireless services too.

7.1.2 Antenna Design

A 62mil thickness FR4 substrate is used in this design with a dielectric constant $\varepsilon_r = 4.4$ and relatively high loss tangent of 0.02. A reconfigurable antenna that can be configured to work at 4 bands (including PCS/DCS, UMTS, IEEE 802.11 a, b, and g) is designed. Twenty switching devices are required for the reconfiguration, while prototypes with hard-wired connections (direct metal connections) are fabricated and tested. The antenna structure and its corresponding measurement results are shown in the following sections.

A square loop resonating at 2.4GHz for IEEE 802.11b/g WLAN application is formed by connecting all outer metallic stripe-segments together, as shown in Figure 7.1(a). This loop defines the maximum area of the whole antenna. A fractal loop for 2GHz is created by indenting the edges of the square loop structure, as shown in Figure 7.2(a). A lower frequency is achieved since a longer path is formed. With the same idea as the 2 GHz fractal, by applying more indents in two edges, circumference of the loop can be elongated further to form a structure resonating at 1.8GHz (Figure 7.3). By connecting all inner stripes, a loop working at 5.2 GHz, the 802.11a band, is formed. Same as other configurations, a good match and similar radiation pattern is measured. The measured return loss and radiating performances of the fabricated 2.4GHz, 2.0GHz 1.8 GHz and 5.2 GHz loop configurations are shown in Figure 7.1, Figure 7.2, Figure 7.3 and Figure 7.4 respectively. For all these 4 configurations, the feeding coplanar strip parts were kept the same to provide the same input impedance. The measured reflection coefficient for all these configurations were always better than -14dB. This indicates that the radiation impedance of these loop antenna and its fractals are close -- another key feature of these fractal loop antennas.

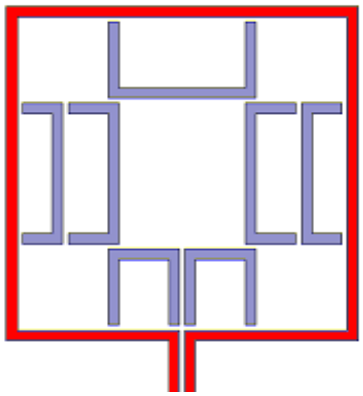

(a) Antenna structure

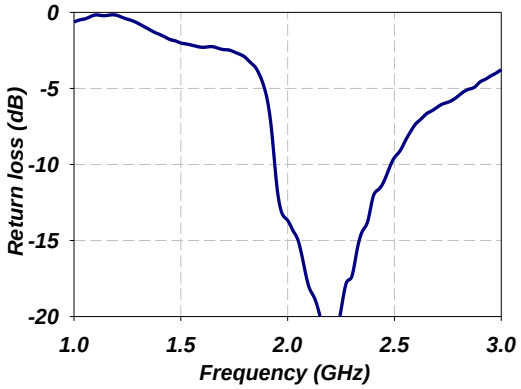

(b) Measured return loss

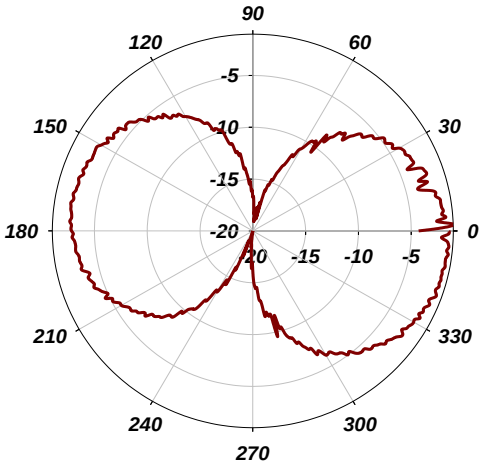

(c) Horizontal cut

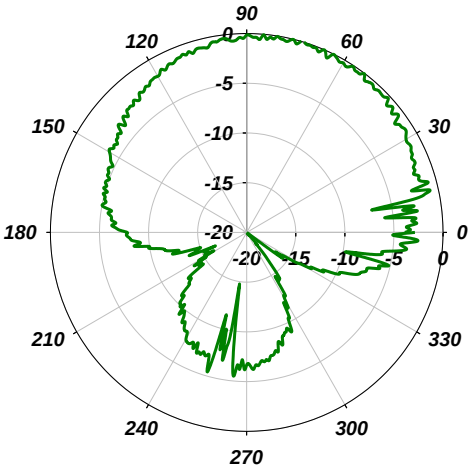

(d) Vertical cut

Figure 7.1 Structure and measured performances of 2.4GHz configuration.

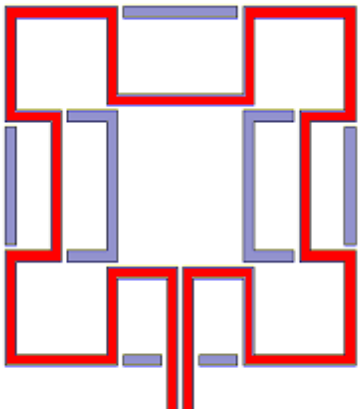

(a) Antenna structure

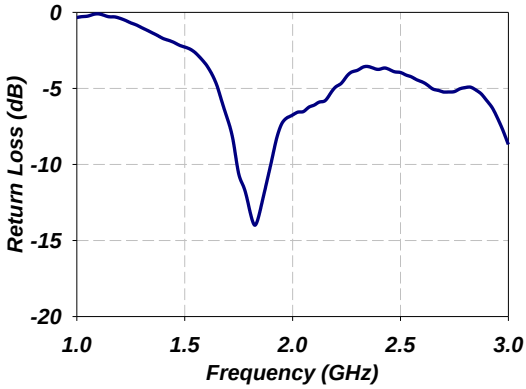

(b) Measured return loss

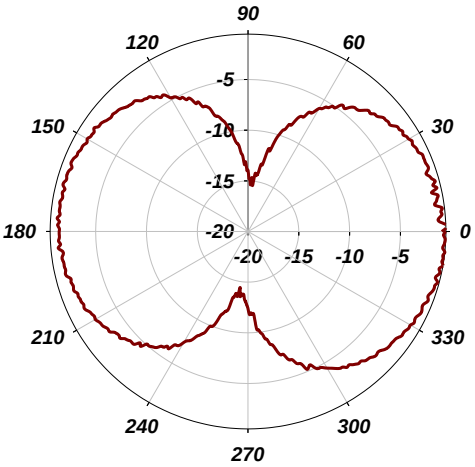

(c) Horizontal cut

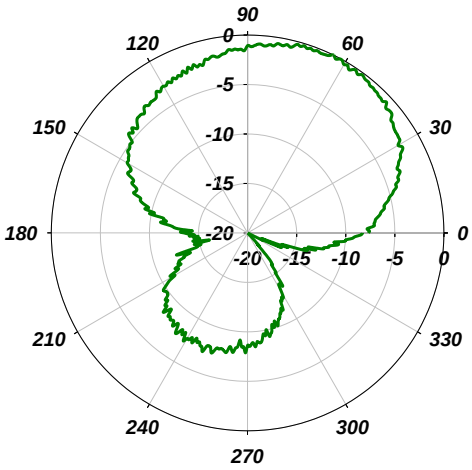

(d) Vertical cut

Figure 7.2 Structure and measured performances of 2 GHz configuration.

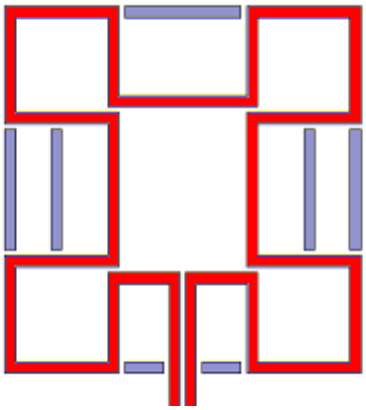

(a) Antenna structure

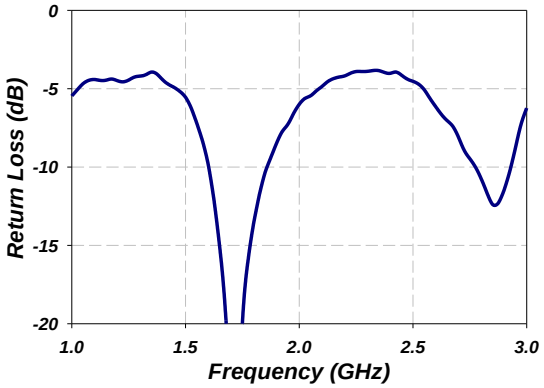

(b) Measured return loss

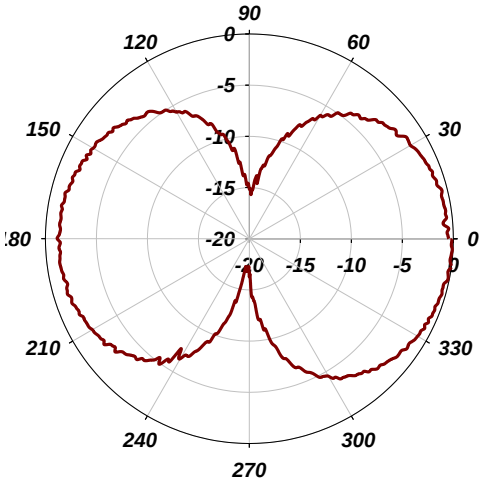

(c) Horizontal cut

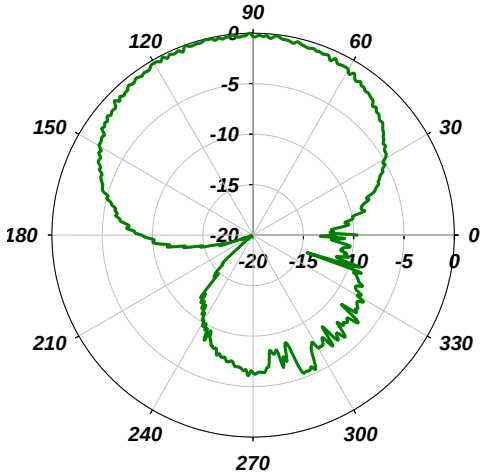

(d) Vertical cut

Figure 7.3 Structure and measured performances of 1.8 GHz configuration.

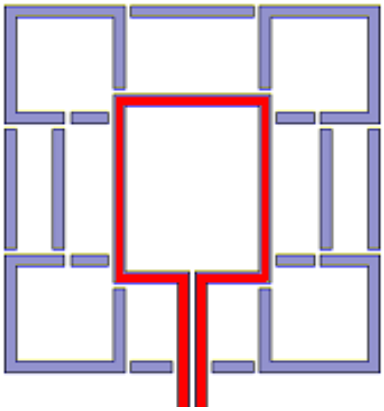

(a) Antenna structure

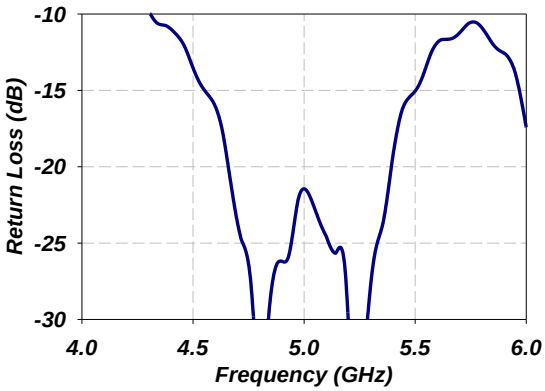

(b) Measured return loss

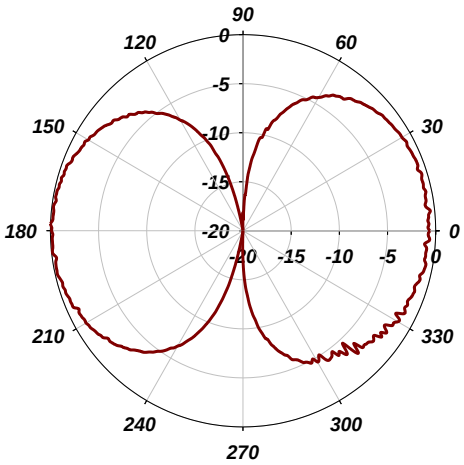

(c) Horizontal cut

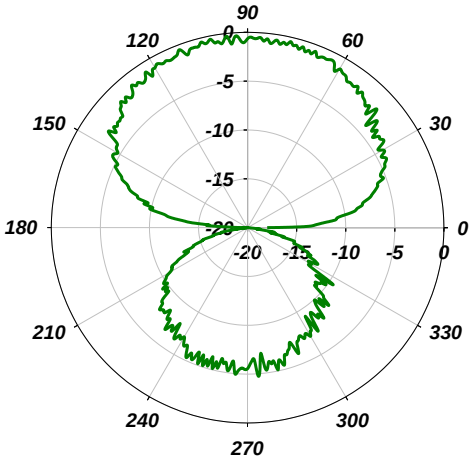

(d) Vertical cut

Figure 7.4 Structure and measured performances of 5 GHz configuration.

7.1.3 Wide Band Balun Design

A balance-unbalance transformer (balun) was designed to feed the maze loop structure over a wideband from 1.8 to 5.2GHz as shown in Figure 7.5. The balun is comprised of two radial stubs, one open radial wideband stub is on the top trace layer, and the second a short-circuited wideband slotline radial stub on the bottom ground layer. Quarter wavelength impedance transformers were used to convert both the high impedance slot and the coplanar strip line to a 50 ohm microstrip input.

By judicious choice of the length of the transformer, an additional passband at the 5.2GHz band can be introduced in addition to the wide passband designed from 1.8 to 2.4GHz. The return loss of the balun is shown in Figure 7.5. The developed balun will pass all the bands of interest and help in blocking all others including higher order resonant modes at higher frequencies of our fractal antenna structure. For a proof of concept, we manufactured hard-wired reconfigurable "Maze" antennas and is shown in Figure 7.6. All the tiny black rectangles in Figure 7.6(b) indicates the locations of the require switchs here. The switch number requirements need to be greatly reduced before this concept can be implemented, as will be discussed in the next section.

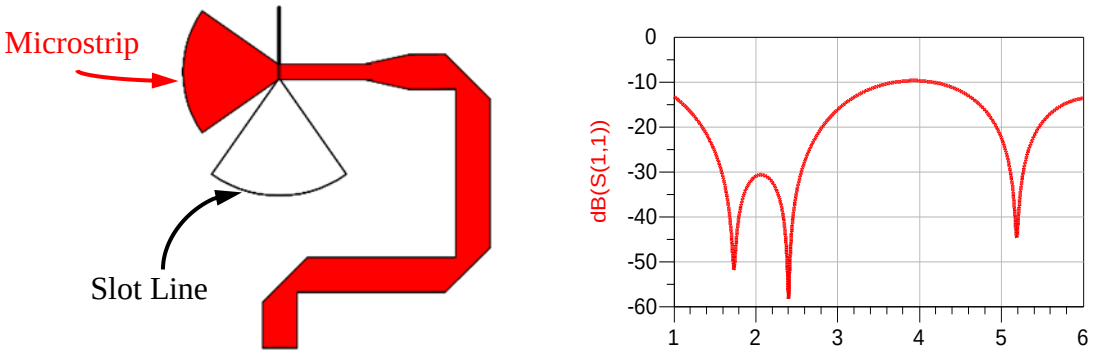

(a) Balun structure (b) Simulated return loss

Figure 7.5 Structure and simulated return loss performance of the balun design.

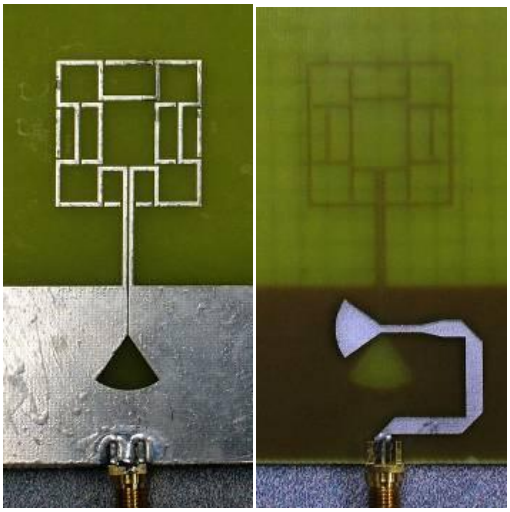

(a) Hard-wired connection

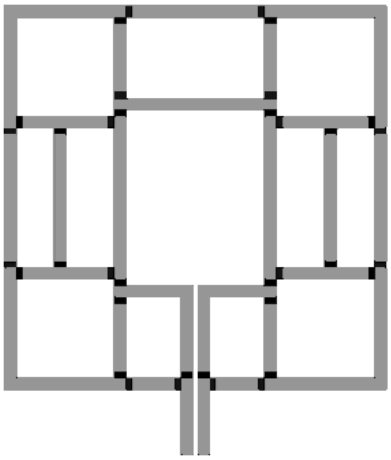

(b) Locations for switches

Figure 7.6 Reconfigurable "Maze" antenna prototype and switch locations

7.2 Reconfigurable "Mini-Maze" (Bent Monopole) Antenna

In an effort to develop a universal wireless receiver, a new antenna concept, "the maze antenna", has been introduced in order to cover different wireless bands through geometry reconfiguration [36]. Due to its fractal structure, the maze antenna offers almost constant input impedance and radiation pattern characteristics over all of the operating frequency ranges. However, it requires a multitude of MEMS switches to hop from one frequency to another. Use of many switches would render relatively expensive antennas when compared to alternative competing conventional multi-band antenna designs.

In this section, the maze antenna design concept is extended to a much simpler structure, which significantly reduces the required number of MEMS switches for reconfiguration. The newly developed mini-maze antenna is based on symmetry plan theorems, and it occupies only one fourth of the original area. It requires the use of only two SPST MEMS switches or one SPDT switch to hop between 3 frequencies. This new design is aimed at eliminating the DC feed complexity and any undesirable feed line radiation effects.

In the following sections the mini-maze antenna concept is presented, followed by a discussion on the utilization of the packaged MEMS switches, including their impact on the design, and effects of the presence of the DC biasing lines.

7.2.1 Design concept of the mini-maze antenna

At the resonant frequencies of the maze antenna for each configuration, the current distribution on the antenna has a null along the vertical centerline of the loop structure, i.e. open boundary condition, as shown in Figure 7.7. Therefore, half of the loop can be cut without disturbing the field distribution. The distinct structure resonances are kept the same, while the radiation resistances drop from about 150Ω for the loop antenna to less than 100Ω for this new configuration of a rather bent dipole antenna structure.

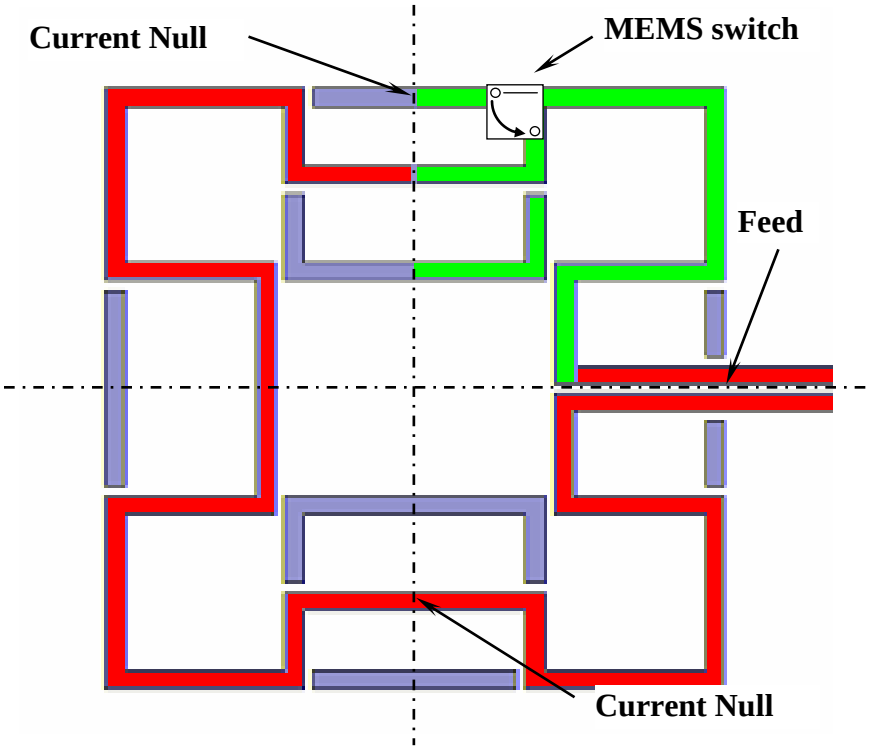

Figure 7.7 Size reduction of "Maze" antenna using symmetry planes

Even symmetry along the horizontal centerline has been also utilized to further reduce the original loop's size, and a ground plane is added along their symmetry plane to form a bent monopole (mini maze) as shown in Figure 7.7. Again, the resonant frequencies are kept the same for each configuration, but the input impedances at resonance are further reduced to less than 50Ω. However, the monopole antennas do not require baluns and are fed by a simple microstrip line. The size of the mini maze antenna is only one fourth the size of the original maze, and more importantly, the total number of switches required is significantly reduced to tow Single Pole Single Through (SPST) switches or only one Single Pole Double Through (SPDT) switch.

7.2.2 Hard wired designs

A series of reconfigurable mini maze antenna designs were fabricated and tested using hard-wired connections. Three wireless services including GPS (1.57 GHz), DCS/PCS (1.8 GHz), and WCDMA (2 GHz) are addressed. Diagram of three configurations and one of the built antennas are shown in Figure 7.8. The overall monopole length is inversely proportional to the operating frequency. Two lower frequencies are achieved by closing the two SPST switches individually, and when both switches are opened, the antenna works at the highest frequency.

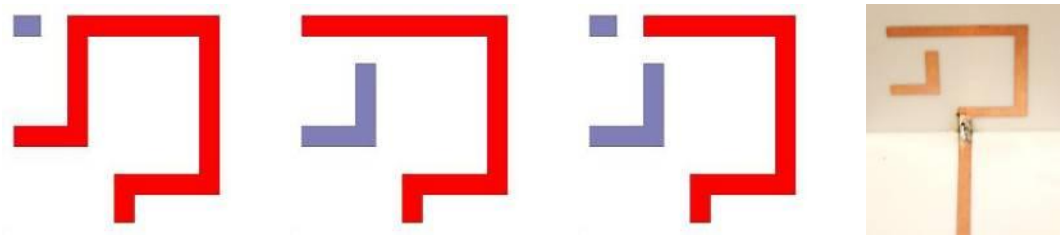

(a) 1.57GHz (b) 1.8GHz (c) 2GHz (d) Prototype

Figure 7.8 Hard wired reconfigurable mini-maze antennas designs and prototype

These antennas are simulated using Ansoft HFSS and built on Rogers RO4003C high frequency laminate materials. Simulated and measured return losses are shown in Figure 7.9, where the measured resonance frequencies of all three configurations are very close to the simulated results. The measured radiation patterns are shown in Figure 7.9. Even with a reduced size, the measured gain is nearly the same as the original maze antenna due to the addition of a ground plane.

7.3 Implementing MEMS Switches

In most reconfigurable antenna designs, MEMs switches and antenna structures are fabricated together on the same wafer [37]. However, these techniques are more suitable for very high frequencies. In the wireless frequency range, designers currently tend to place a packaged MEMS switch directly on the antenna structure. The major difficulties of integrating switching devices into antenna structures are the DC feeding method as well as the accurate device modeling. In this sense, patch antennas [38] and microstrip line antennas [39] are mostly used for reconfigurable structures, because it is easier to feed and precisely model these devices with a large ground plane behind the circuit.

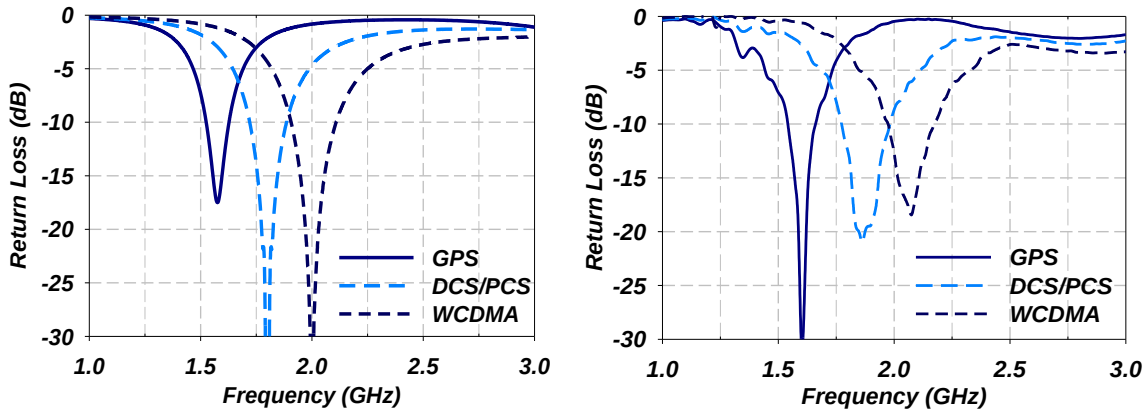

(a) Simulated (b) Measured

Figure 7.9 Simulated and measured return loss performances of the hard wired reconfigurable mini-maze antenna

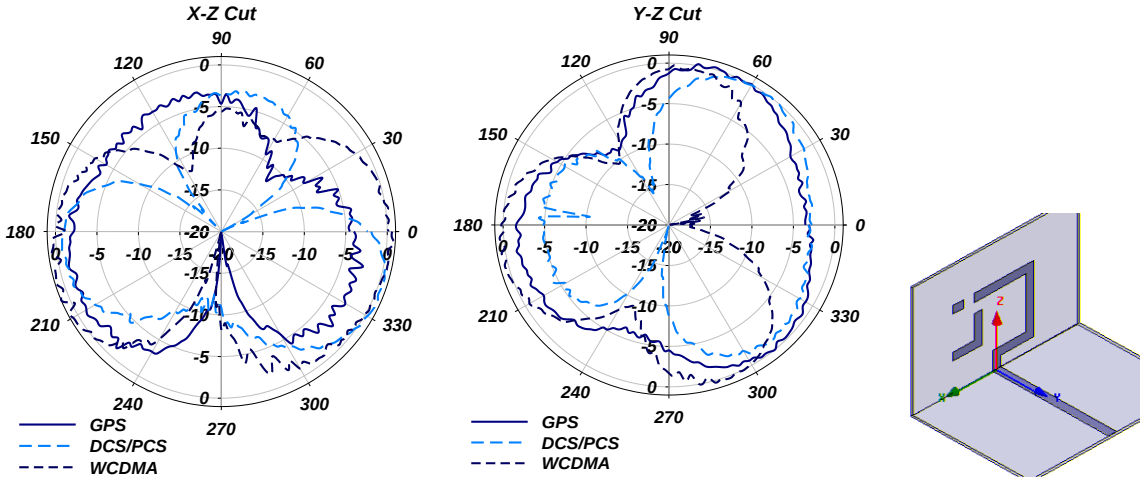

(a) x-z cut (b) y-z cut (c) coordinate systems

Figure 7.10 Measured radiation patterns of the three hard wired configurations

7.3.1 MEMS switches

In our design, hybrid MEMS switches have been successfully integrated into the printed antenna structure after addressing some practical and modeling issues. The utilized commercial MEMS switches are cantilever type SPST switches, as shown in Figure 7.11, each has a very small package size of 1.5mm by 1.5mm. The mechanism of this MEMS switch is very similar to a FET switch. A DC voltage is applied between the Gate and Ground or Source to control the connection between the source and drain of the device. A ground plane in the back of the device is required for the appropriate DC and RF operation. However, for antenna applications, any metal piece in the vicinity of the radiating elements would affect its radiating characteristics being 'parasitic'. DC feed-line effects could be significant too. Their layout and connection to ground plane are more critical in antenna designs. Usage of quarter wavelength short-circuited stubs is not acceptable here, and inductors with ferrite cores are perfect RF chokes but bulky. Therefore, the use of very large resistances is an acceptable alternative given that they will have minimal RF insertion loss.

The fabricated mini-maze antenna with hybrid MEMS switches is shown in Figure 7.(a). The MEMS switches' terminals are connected to the antenna with bond wires. As can be seen from the simulated field distribution on the antenna in Figure 7. (b) &(c), the introduction of a ground pad and DC feed lines of the MEMS switch causes dramatic change in the field distribution. These effects should be taken into account during the MEMS switch integration.

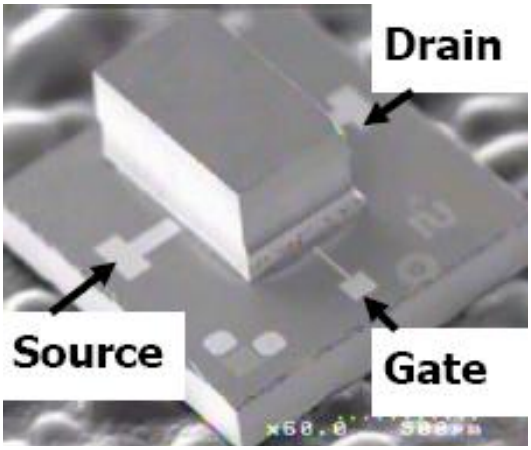

(a) Perspective View

(b)

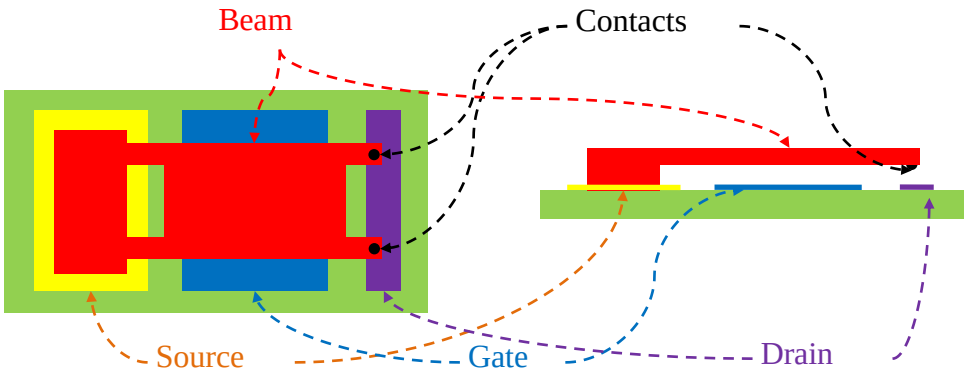

(b) Top View (c) Side View

Figure 7.11 Cantilever MEMS switch structure

7.3.2 Device Modeling

The equivalent lumped element circuit model of the switch is generated based on the Radant SPST 12GHz MEMS S-parameters. As shown in Figure 7.13, two PI networks are used to represent open and short circuited cases of the MEMS switch. S-parameters of equivalent circuits are compared with measured results in Figure 7.14, our model gives very similar results as the measured ones from 1 to 8GHz.

Due to the limited size of the ground plane for MEMS switch, the modeled values for shunt capacitance to ground should be reduced as well. In this design, half of the shunt capacitance values shown in Figure 7.13 (a) are used as an estimate. As shown in Figure 7.13 (b), the equivalent circuit model is used in a full wave simulater as a lumped element boundary conditions.

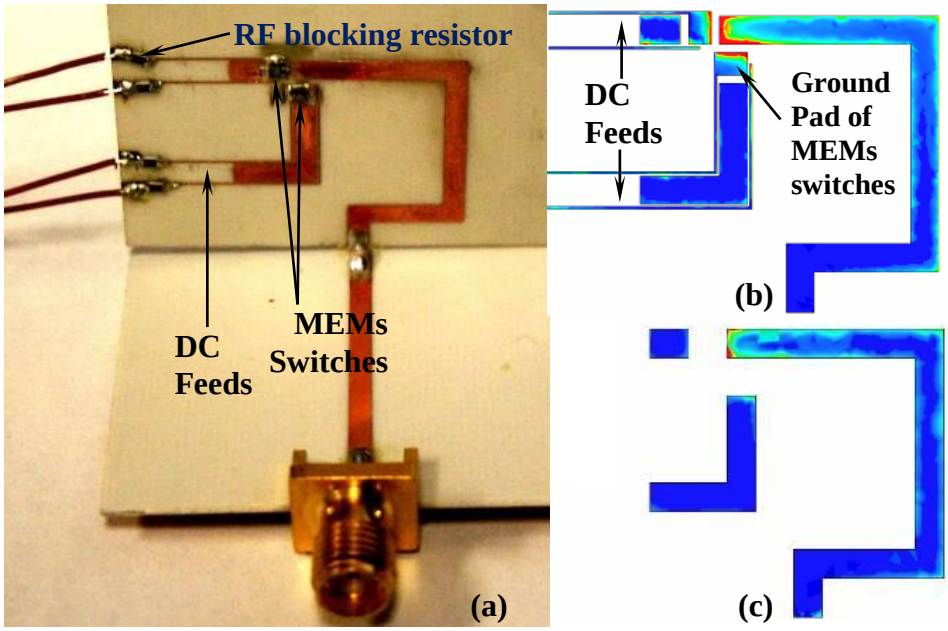

Figure 7.12 Reconfigurable mini-maze antennas built with hybrid MEMs switches (a), Simulated E-field distribution at resonance of antenna structure (b) with and (c) without MEMs ground pad and DC feed lines

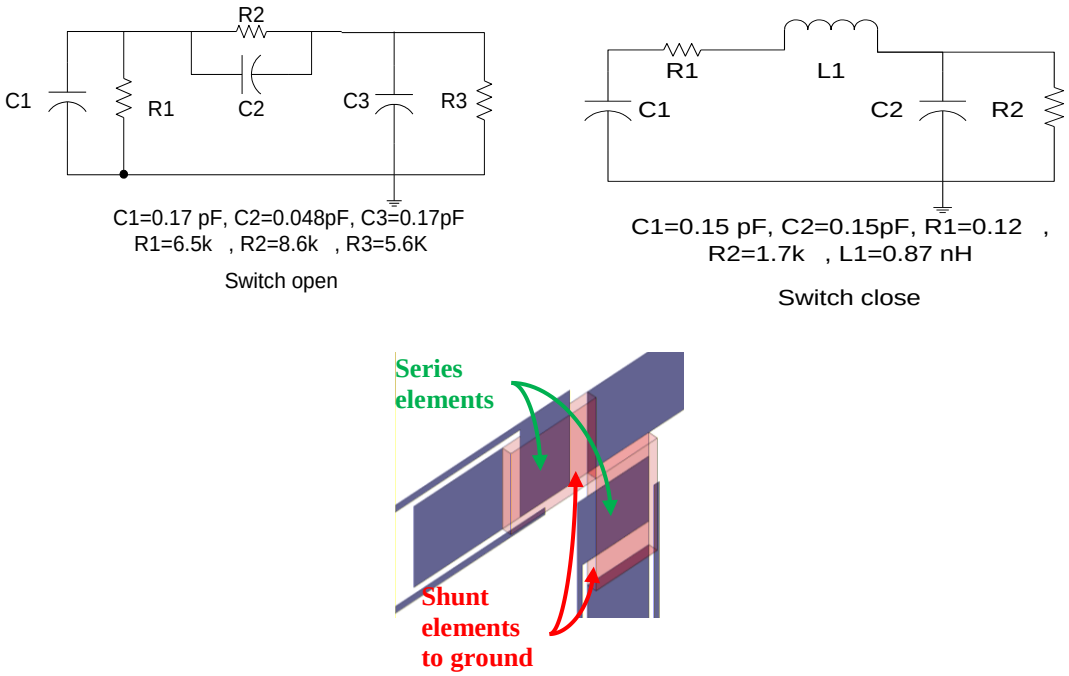

(a) Equivalent circuit model (b) Simulation Model

Figure 7.13 Equivalent circuit model and simulation model for short and open states

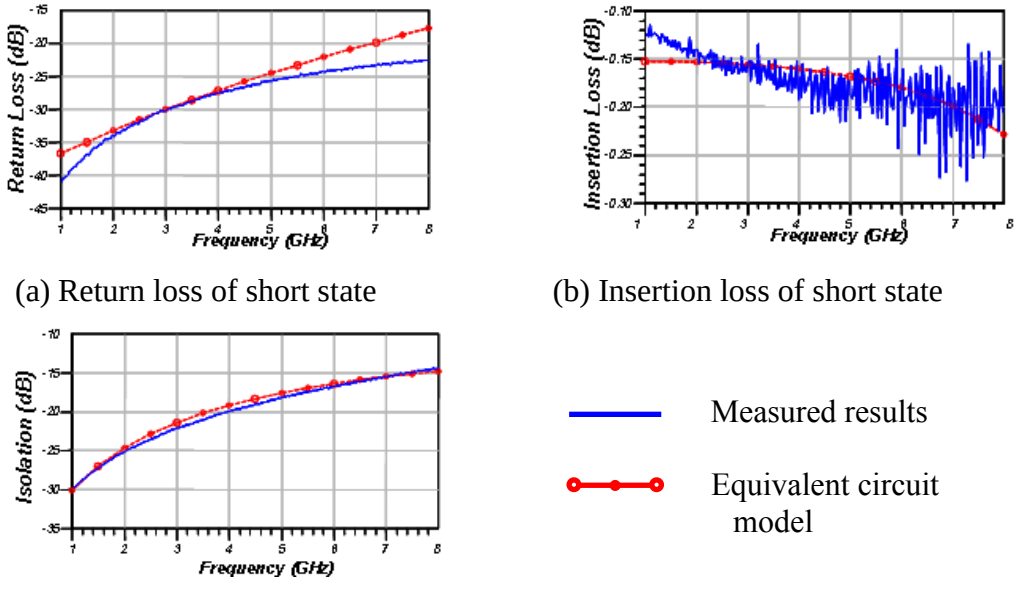

(a) Return loss of short state (b) Insertion loss of short state

(c) Isolation of open state

Figure 7.14 Performance of equivalent circuit model

7.3.3 Measured Results:

The measured results of the mini maze antenna with hybrid MEMS switches, shown in Figure 7.(a), are demonstrated in Figure 7.15. As can be seen, the simulated and measured resonance frequencies of all the three configurations are very close. Apparently, for the limited size ground plane, an equivalent capacitance with half its values should suffice and generate results that are close practice.

Radiation patterns of the developed mini maze antenna are also evaluated and shown in Figure 7.16, and due to the effect of the feeding lines, the results are slightly different from Figure 7.10. However, a gain drop of less than half a dB is observed due to the insertion loss of the MEMS switches.

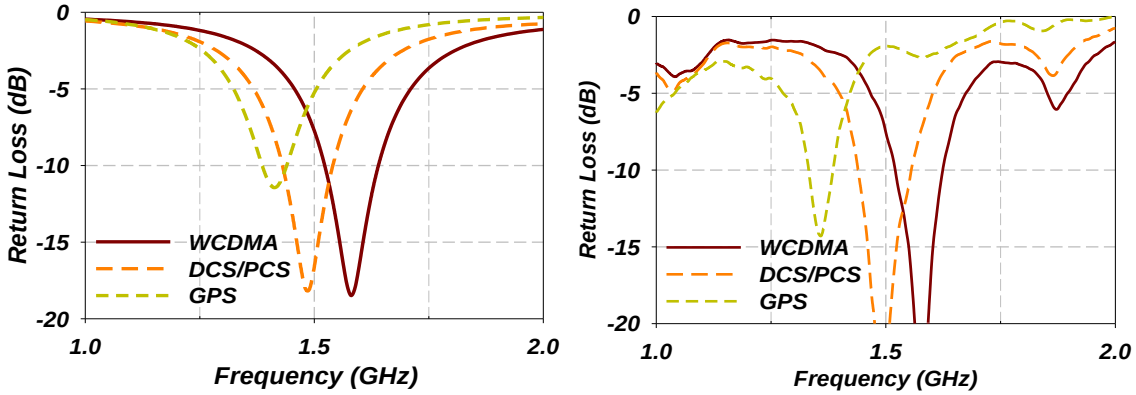

(a) Simulated (b) Measured

Figure 7.15 Simulated and measured return loss of mini-maze antenna with MEMS

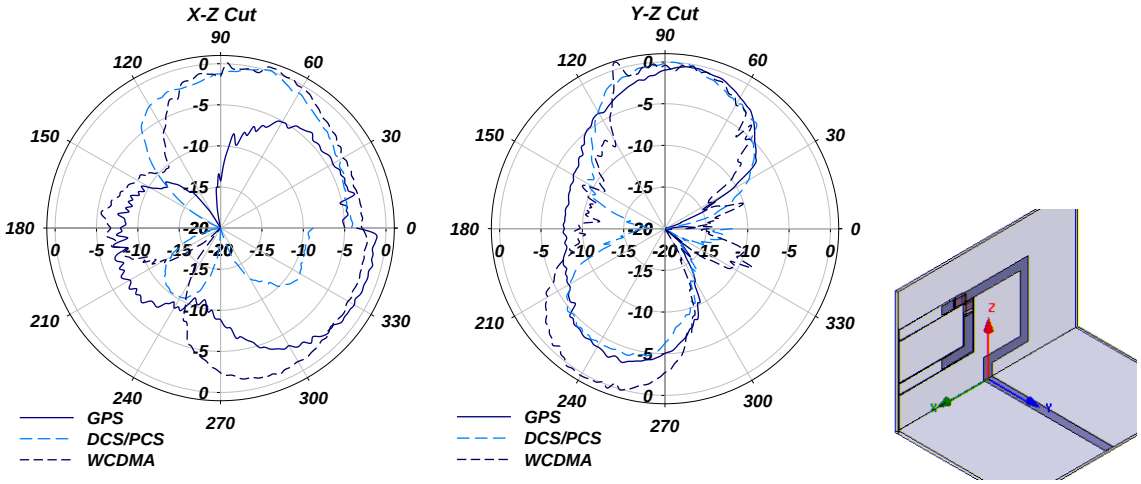

(a) x-z cut (b) y-z cut (c) coordinate systems

Figure 7.16 Measured radiation patterns of the developed mini maze antenna with hybrid MEMS switches.

7.4 Summary and Conclusions

A reconfigurable maze antenna using RF MEMS was proposed to address the multiple needs of the wireless market. Three major difficulties including (1) RF signal leaks to the DC feed lines, (2) precise modeling of MEMS switches in an antenna environment, and (3) reduction of total switching devices needed, have made the implementation of real MEMS switches a challenge. In this chapter, many design techniques are discussed to solve these three problems, and a modified mini maze antenna with only two RF MEMS switches was fabricated and tested. Measured results are good. DC feeding techniques have been summarized, and a modified equivalent circuit model of the MEMS switch used in the antenna structure is proposed for a full wave simulation of antennas with hybrid MEMS switches.

Chapter 8

Reconfigurable Multiband Antenna for Multi-Radio Platforms

Combined reconfigurable and multi-band design concepts have been utilized to design antennas for mobile multi-radio platforms. Two concepts are introduced in this chapter. One is based on meandering branch-line monopoles for mobile handsets, and the other on planar inverted-F antennas (PIFA) for laptop applications. Both have unique structures to comply with both space and service requirements, and utilize switches to provide two operating reconfigurable multi-band states. Each state is capable of covering specific service group to simplify service switching, and minimize out-of-band input noise.

8.1 Introduction

Multi-band antennas are widely used for many multi-radio platforms, where either one service could have multiple standards utilized at different countries, or many services need to be simultaneously supported at the same country, but should be received through the same antenna. Single band reconfigurable antennas, on the other hand, are designed to switch to a desired service and to be solely dedicated to one service to achieve maximum out-of-band noise rejection performance. As the number of services increases, the development of either of these antennas becomes more and more challenging due to the

space limitations of the mobile platform and antenna isolation requirements for multiple radio working together for the former, while for the latter, its design becomes more complicated and suffer from high loss and unacceptable DC power consumption when using multiple switching devices.

We propose here two novel hybrid reconfigurable multi-band antenna structures that are based on these two concepts. In other words, reconfiguring the multi-band antenna, where multitudes of switching devices are used to hop between several multi-band configurations. Through judicious grouping of frequency bands for each configuration, advantages of both the multi-band and the reconfigurable antenna structures can be simultaneously achieved while supporting more services.

Our developed design for handsets is comprised of a compact reconfigurable meandered monopole antenna, and covers almost all WWAN and WLAN standards with only two configurations, one serving all the cellular bands and the other covering all wireless frequencies. Similarly for laptops, alike concept is realized by a novel reconfigurable multi-band PIFA structure, which supports all US cellular and indoor WLAN frequencies. Both these designs have been optimized to minimize the number of switches, where only two are required. The multi-band construction strategy, switch integration schemes, and simulated and measured results of these novel designs will be presented here in detail.

Table 8-1 Frequency Grouping of Handset and Laptop Antenna Configuration (WWAN)

Unit: GHz		WWAN Configuration				
Grouped Bands	Handset	0.824-0.96 (15%)			1.71-2.17 (23.7%)	
	Laptop	(8.3%)	N/A		(7.3%)	N/A
Service		GSM850	GSM900	DCS	PCS	IMT2000
Frequency		0.824-0.894	0.88-0.96	1.71-1.88	1.85-1.99	1.92-2.17
Country		U.S.	Europe/Asia		U.S.	

Table 8-2 Frequency Grouping of Handset and Laptop Antenna Configuration (WLAN)

Unit: GHz		WLAN Configuration			
Grouped Bands	Handset	(3.5%)	4.9-5.85 (16.8%)		
	Laptop	(3.5%)	4.9-5.35 (8.8%)		N/A
Service		802.11 b/g/n	802.11 a		
Frequency		2.4-2.484	4.9-5.25	5.15-5.35	5.725-5.85
Country		Universal	Japan/ U.S. Indoor		Outdoor

8.2 Reconfigurable Multi-band Antenna Design

In order to support the required wireless services for different mobile multi-radio platforms listed in both Table 8-1 and Table 8-2, the frequency bands need to be strategically grouped to minimize the number of switchable configurations while still covering the required services. The guidelines for this selective grouping include:

1). Different standards of the same services can be grouped together, since only one frequency band will only be used at a certain time in a certain country. For instance, the GSM850 and GSM900 bands can be grouped into one configuration.

2). Different services with close frequency bands need to be allocated at different configurations to improve out-of-band noise rejection. For example, 2.4GHz WLAN services need to be separated from the cellular ones that are around 2GHz (PCS/DCS/IMT2000) to avoid their interference and simplify out-of-band noise filtering.

According to our grouping criterions, the required services are separated into two distinct application groups as shown Table 8-1 and Table 8-2. For instance, in the handset case, all cellular services including GSM850, GSM900, DCS, PCS, and IMT2000

(WCDMA/HSDPA) frequency bands are grouped together and classified as WWAN configuration (Table 8-10. On the other hand, all internet services including 802.11.a, b, g, and n are consolidated in the other configuration, which is utilized for WLAN services (Table 8-2). For each configuration, a multi-band antenna is required. It is given here that any two services from these grouped configurations will not be required to operate at the same time. Similar grouping is applied for laptop antennas with fewer services supported.

8.2.1 Meandered Monopoles for Mobile Handset

Basic antenna structures need to be selected according to the form factor of the designated mobile platform. For mobile handsets, antennas are always placed at either end of the handset and its size is limited by the width of the PCB. Therefore meandered monopole antennas are suitable for mobile handset applications for its compact size and ease of reconfiguring the resonance frequency by altering the monopole's length. For each configuration, a multi-band response can be achieved by having two meandered branches resonating at the lower and upper bands respectively. As shown in Figure 8.1, (highlighted parts are metal). The developed antenna consists of two bent monopole branches with different length. Two switches are utilized, one in each branch to control the physical length of the monopole. According to the previous grouping, when both switches are turned on (the gaps in the monopoles are hard-wired for now), the antenna works at the WWAN configuration, receiving the lower frequency cellular services. When switches are off (as shown in Figure 8.1), the antenna operates in the WLAN configuration. Since a shorter length is utilized, it would result in higher resonant frequencies.

The major challenge of this proposed frequency grouping is its relatively wide bandwidth requirements, especially for the higher band (DCS/PCS/IMT2000) in the WWAN configuration, where a 23.7% bandwidth is required. In our design, we have extended the branch line monopole antennas described by [40] to cover all five cellular bands by utilizing the monopoles higher order resonances as well.

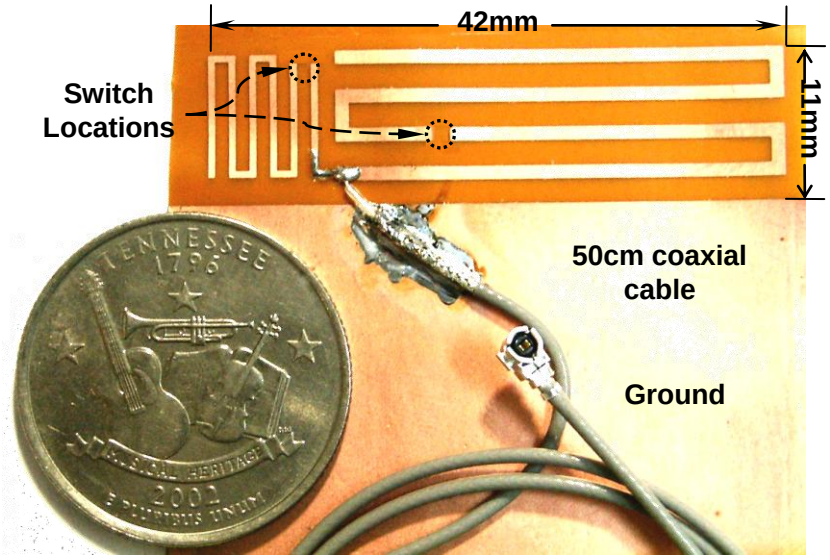

Figure 8.1 Fabricated reconfigurable meandered monopole antenna

We started with a straight monopole main branch covering the GSM850 and GSM900 bands with a length of 0.25 λ_1 at f_1 = 892 MHz. It also has a third order resonance at $f_3 = 3f_1$ and fifth order resonance at $f_3 = 5f_1$. The structure is meandered to be compact. Because of the coupling between the meandered lines, the total length needs to be extended to maintain the same f_0. However, due to weaker coupling effects at higher frequencies, the third and fifth order resonances are significantly shifted lower when the total length is increased. As shown in Figure 8.2, we can control the number of turns and the spacing of the meander line to alter the coupling factor such that with the same fundamental resonance (f_1 = 892 MHz) the higher WWAN band lies between the third and fifth resonances, that is f_3 < 1.71GHz < 2.17GHz < f_5. Then a second meandered monopole with a fundamental resonance within the higher WWAN band is constructed. The meandering orientations of those two monopoles are orthogonal to each other to reduce their coupling, such that each branch can be designed separately. In the final step, these two branches are placed together in shunt, where the fast varying radiation impedance of the main branch is compensated by the slow varying counterpart of the second branch as shown in Figure 8.3. The overall radiation impedance is depicted in Figure 8.4, where a much wider impedance bandwidth is achieved by combining these two branches in shunt.

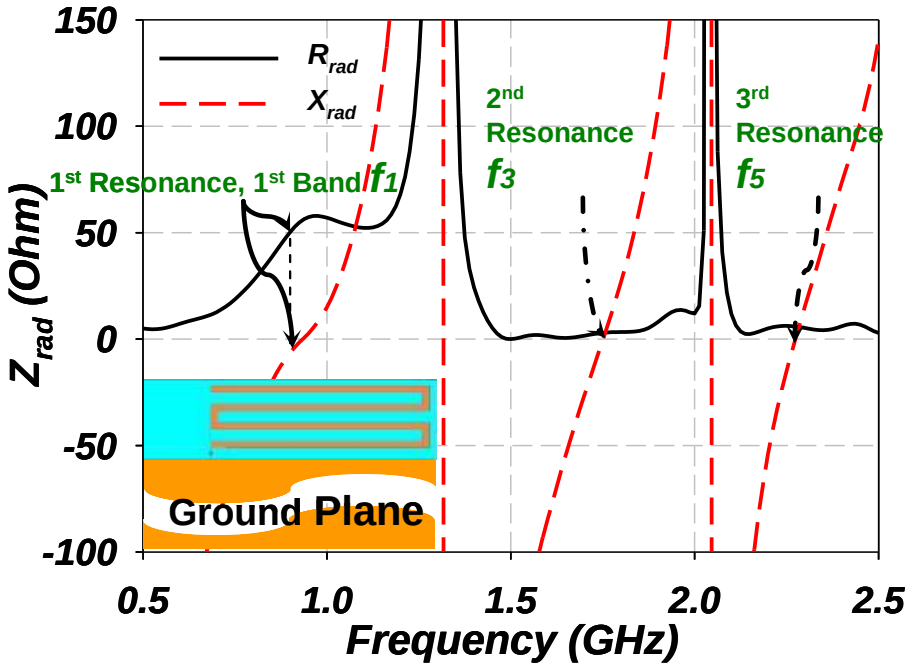

Figure 8.2 Radiation impedance of horizontally meandered main branch

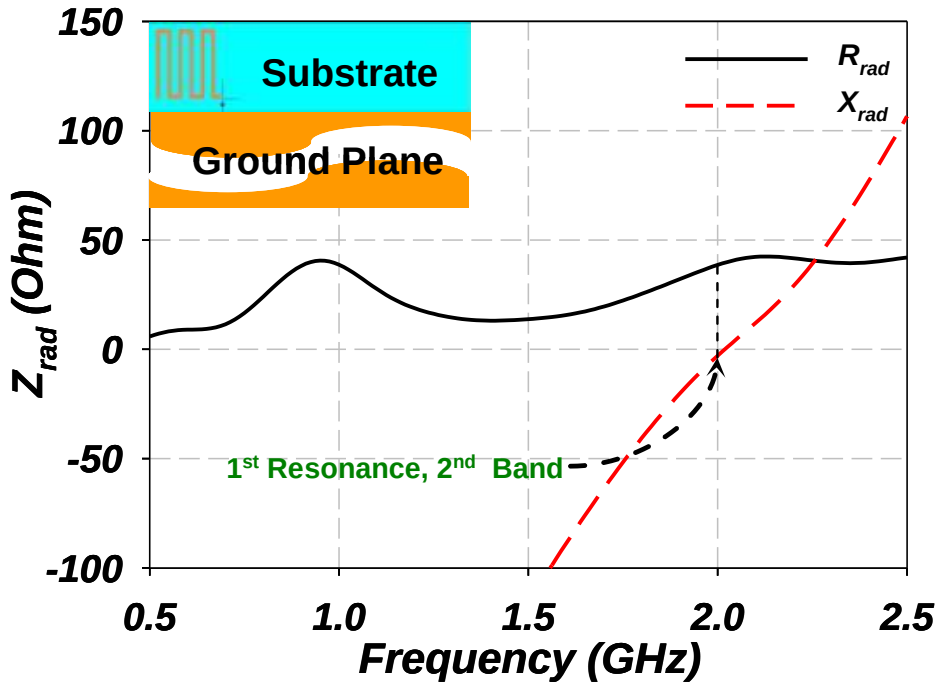

Figure 8.3 Radiation impedance of vertically meandered secondary branch

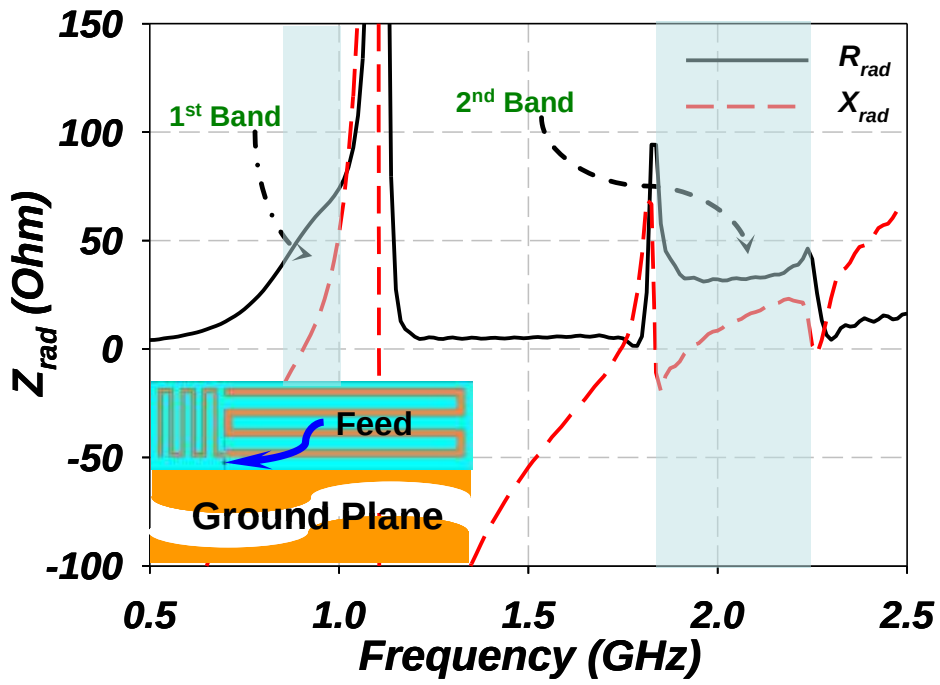

Figure 8.4 Radiation impedance of two branches in shunt.

More importantly, the third and fifth order resonances of the main branch provides strong cut offs of the return loss response at the higher WWAN bands. This filter-like response will help in reducing the requirements of the subsequent front-end filtering stages. Similarly, two switches can be strategically placed along the two branches to shorten their lengths and reconfigure them to operate at higher frequencies, i.e. providing a multi-band configuration to serve the WLAN bands.

8.2.2 Twin PIFA Antennas for Laptops

Monopole antennas are generally not suitable for laptop applications since when placed close to a large ground plane (e.g. laptop lids) they exhibit very low radiation resistances. Meanwhile, PIFA antennas could achieve a good match to 50 Ohm feeds even if they are placed only few millimeters from the ground plane. However, due to the fundamental limitations of the achievable bandwidth, a tradeoff is required between the height of the antennas (i.e. width of LCD rims) and the number of services supported. As a result,

service coverage is usually compromised to support only local standards, where in our laptop antenna design, four essential services for laptop application including GSM850, PCS WWAN services and 2.4GHz and 5GHz indoor WLAN services are selected as listed in Table 8-1 and Table 8-2. Using the same frequency grouping, two WWAN frequencies are supported by one configuration while the WLAN standards by another.

In our design, two PIFA structures are placed back to back sharing the same feed point (Figure 8.5(a)). Two switches are used to switch the shorting pin location in order to toggle between the WWAN and WLAN configurations. As shown in Figure 8.5(b), when switch1 is "ON" and switch2 is "OFF", it forms a dual band PIFA structure [41] operating at the WWAN mode. The length of the top inverted-F structure is about $0.25\lambda_0$ of f_0 = 859GHz and it covers the GSM850 band. Beneath the "F" structure, a grounded "L" shaped structure is also placed close to the feed. This parasitic element can be tuned to resonate at a higher frequency, in our case, PCS band. Similarly, when switch1 is "OFF" and switch2 is "ON", the "F" and "L" shaped structures of the WWAN configuration is shorted to form a shorting pin for another pair of "F" and "L" antennas designed to cover the WLAN frequencies (as show in Figure 8.5(c)). A wedge shape is used instead of the "L" in the fabricated design (as shown in Figure 8.6.) to extend the bandwidth of parasitic element.

A novel switch integration and DC feed scheme is implemented to the twin-PIFA antenna, where only two PIN diode switches are required. As shown in Figure 8.6, the two switches are strategically placed across the gap between the two "F" and "L" shape pairs with opposite orientations. The control voltage signal is carried by the feeding coaxial cable and applied between the feed and ground. Since the two "L" shapes provides a return path for DC current, no additional control lines are required. Each switch can be addressed individually by reversing the polarity of the DC signal, which toggles the operating configuration. This approach completely eliminates the DC feed lines and their parasitic effects to the antenna structures.

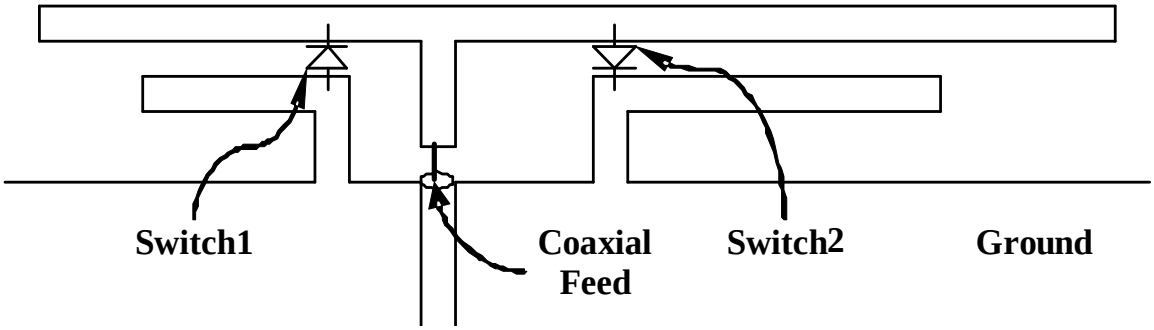

(a) Twin PIFA reconfigurable antenna

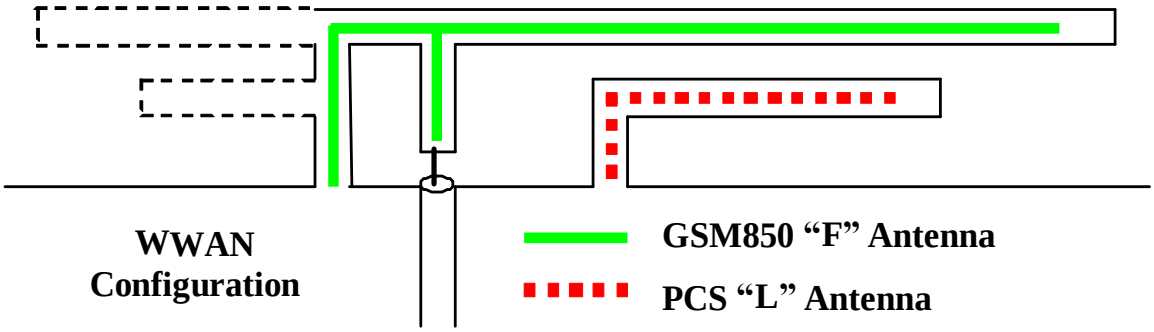

(b) WWAN Configurations

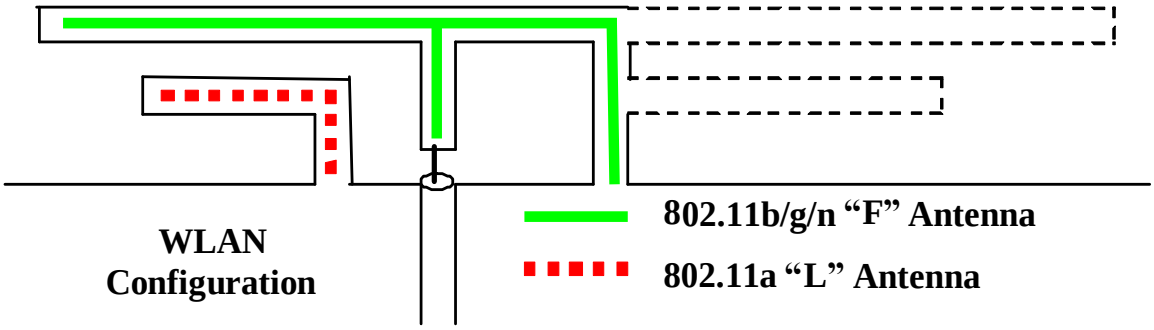

(c) WLAN Configuration

Figure 8.5 Twin PIFA reconfigurable antenna with P-I-N diode switches

8.3 Measured Results

For validating our concepts, both antennas are fabricated on DuPont Kapton flexible circuit material, as indicated in Figure 8.1 and Figure 8.6. The hard-wired version of the meandered monopole is used for measurements while the twin-PIFA structure is fully integrated with p-i-n diode switches.

8.3.1 Meandered Monopoles for Mobile Handset

The simulated and measured return losses of the reconfigurable meandered monopole antenna in WWAN and WLAN configurations are shown in Figure 8.7 and Figure 8.8 respectively, where excellent agreements have been achieved. Their radiation patterns are measured at the center of each frequency-band, and the summary of the measured results of the primary cuts is given in Table 8-3.

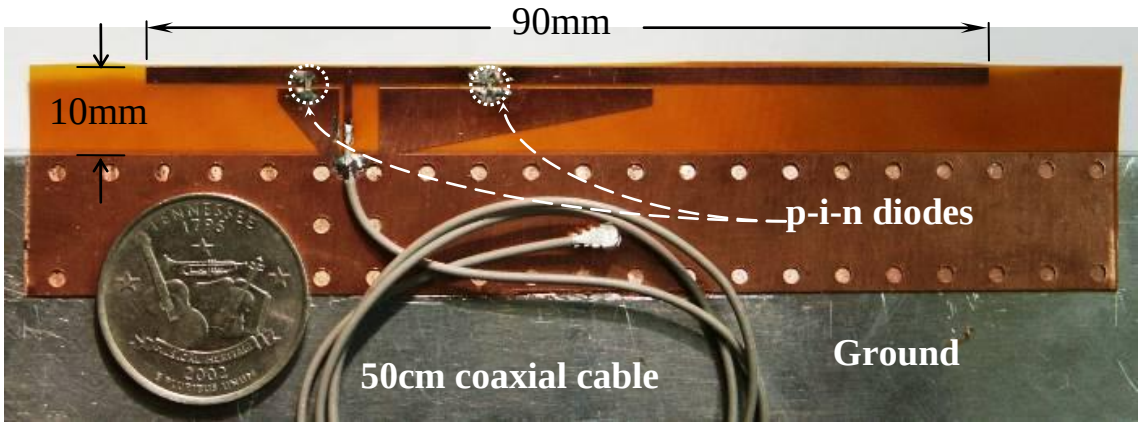

Figure 8.6 Fabricated reconfigurable twin-PIFA antenna for laptops

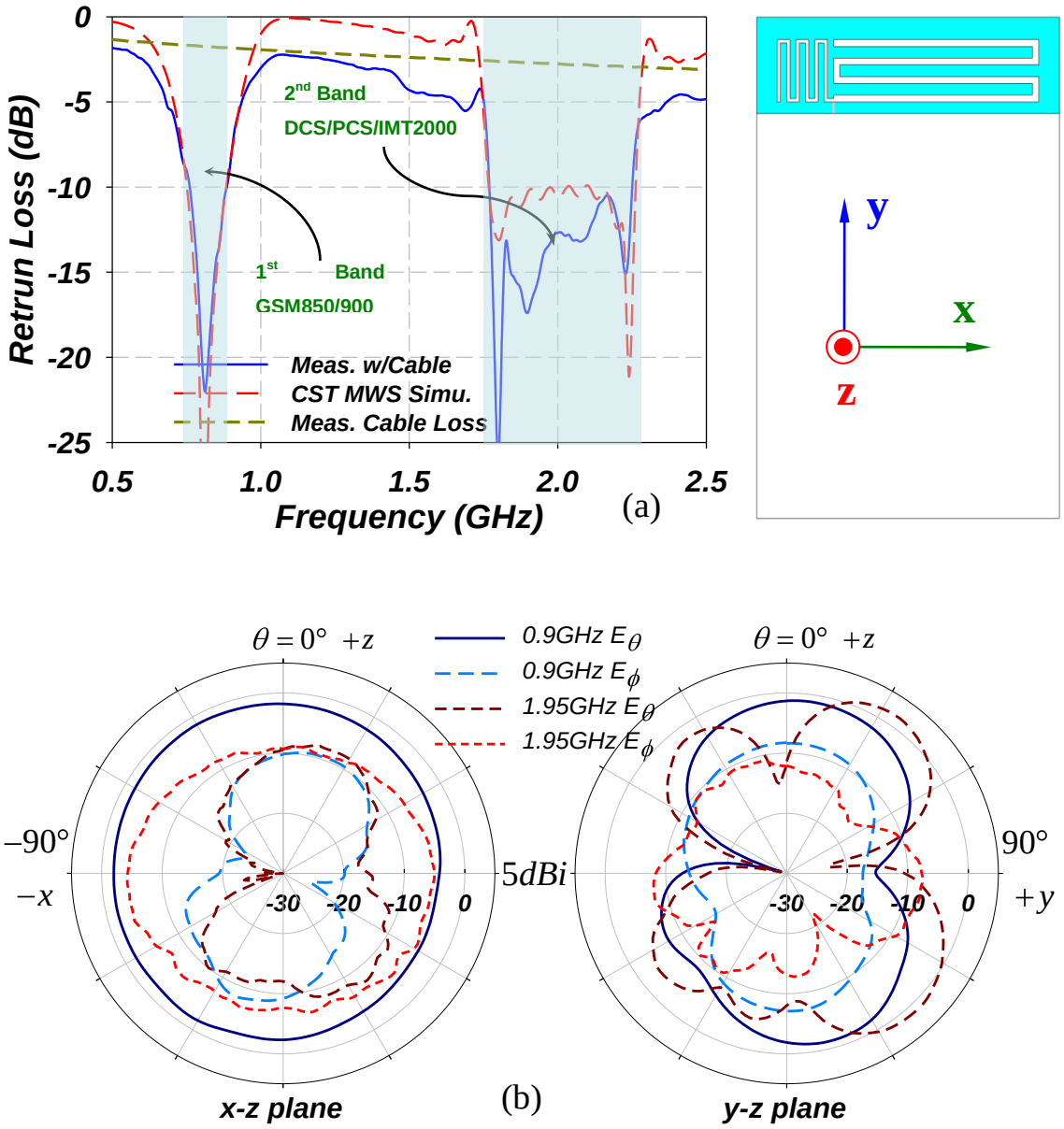

Figure 8.7 (a) Simulated and measured return loss of the WWAN configuration and (b) measured radiation patterns

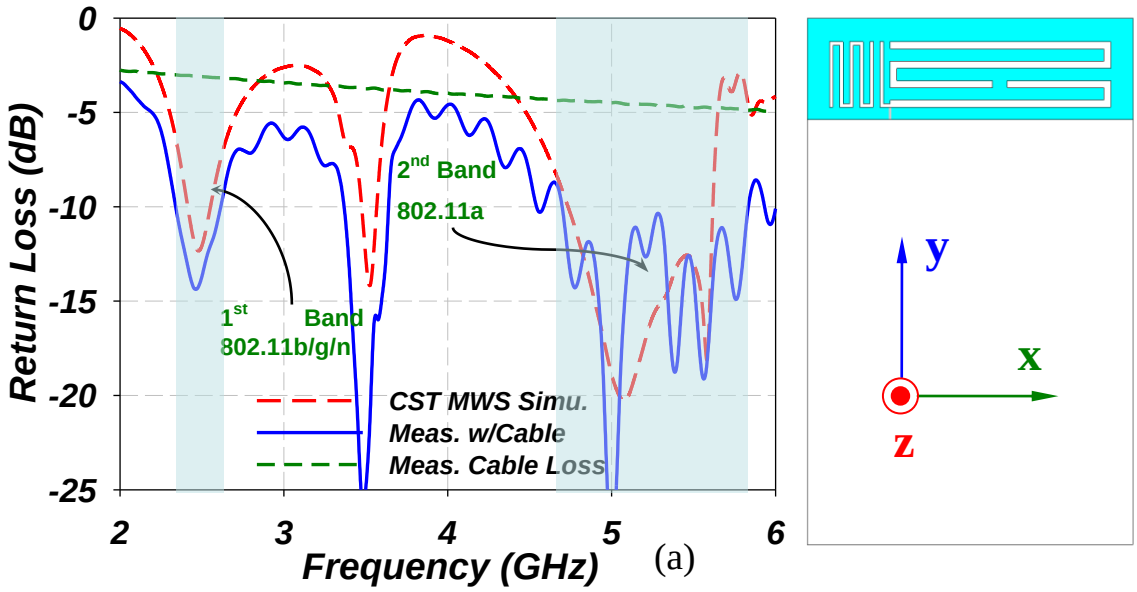

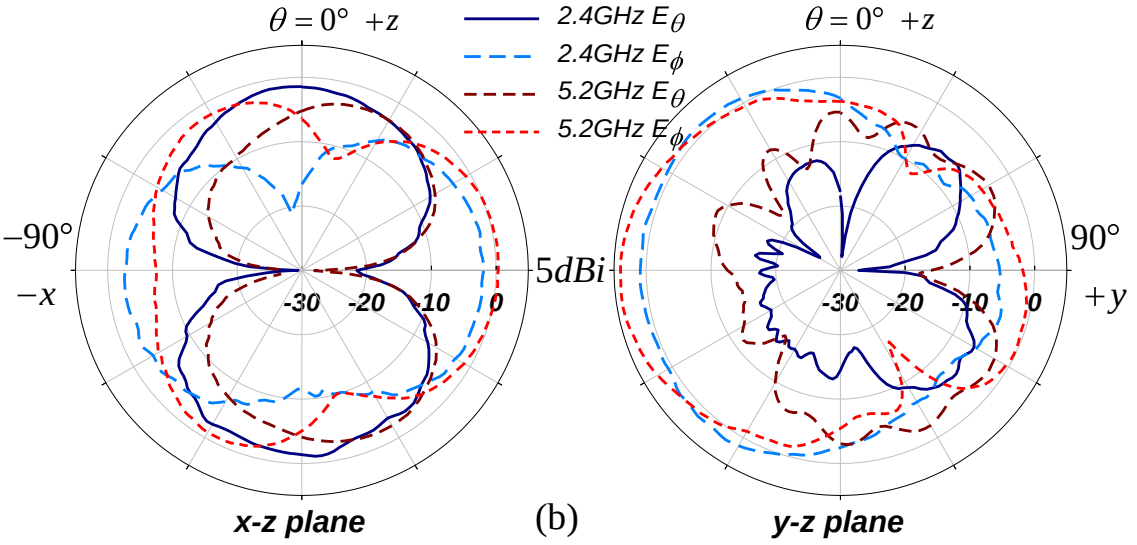

Figure 8.8 (a) Simulated and measured return loss of the WLAN configuration and (b) measured radiation patterns

Table 8-3 Measured Gain of the Reconfigurable Meandered Monopole Antenna

Frequency (GHz)		0.9	1.95	2.4	5.2
Gain (dBi) Max/Average	x-z	-1.0/-2.1	-3.7/-5.4	-0.6/-1.8	4.1/0.3
	y-z	-0.3/-3.7	1.9/-2.7	0.6/-1.5	0.6/-1.4

8.3.2 Twin PIFA Antennas for Laptops with p-i-n Diode Switch

As shown in Figure 8.6, two Microsemi MPP4203 p-i-n diode switches are mounted with opposite orientation across the gaps between the main and parasitic radiators. These switches are controlled by applying +1V or -1V on the coaxial cable to toggle between WWAN and WLAN modes.

The simulated and measured return losses of the WWAN and WLAN configurations are shown in Figure 8.9 and Figure 8.10 respectively, and excellent agreement is observed. Large rectangular metal plates (32cm x 20cm) are used to emulate the lid and body of a laptop. The antenna is placed on the top and side of the metal plate during the measurement and the radiation patterns at the center of each frequency band are shown together with the measured gain of the horizontal cuts given in Table 5-4.

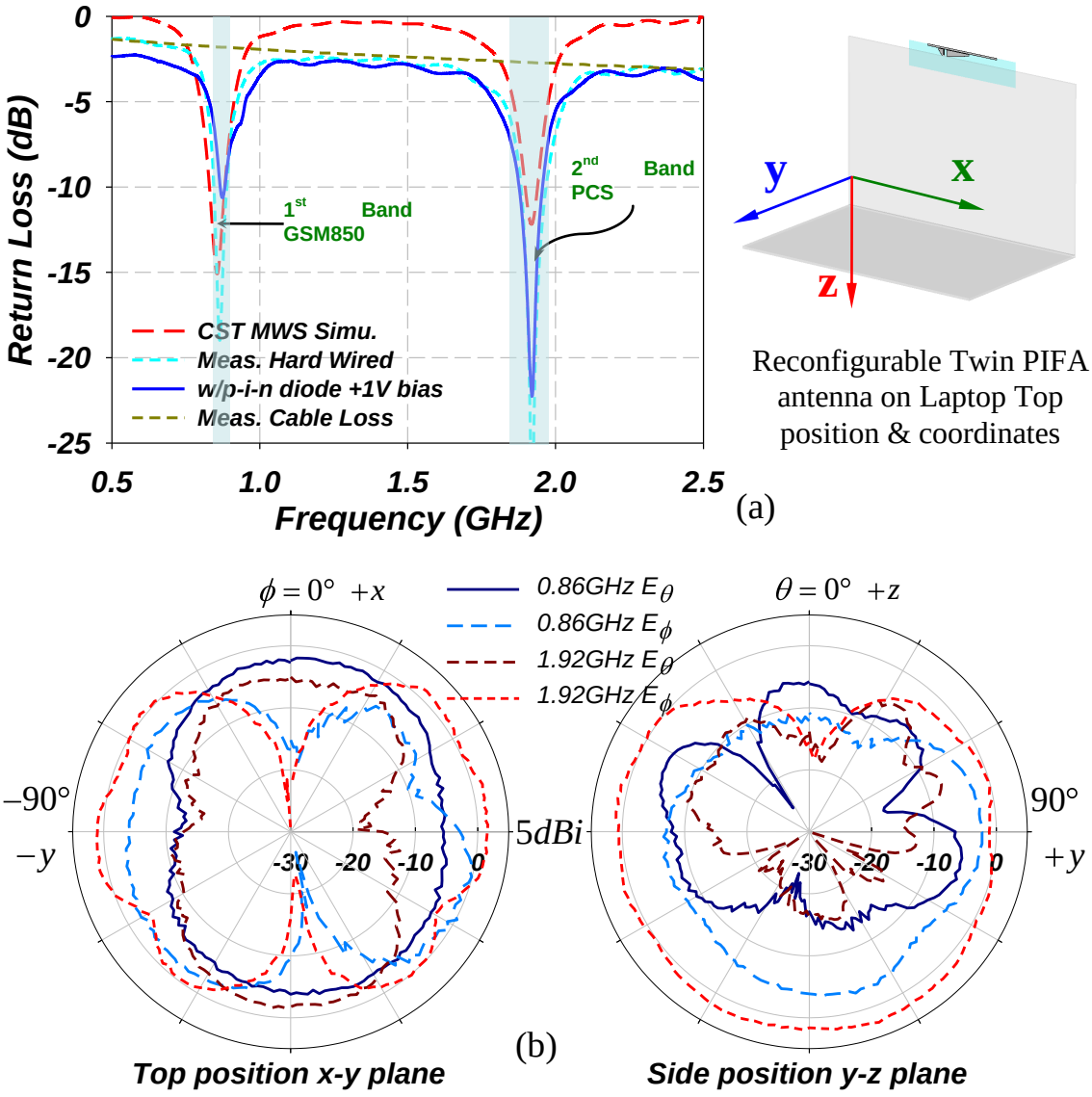

Figure 8.9 (a) Simulated and measured return loss of the WWAN configuration and (b) measured radiation patterns

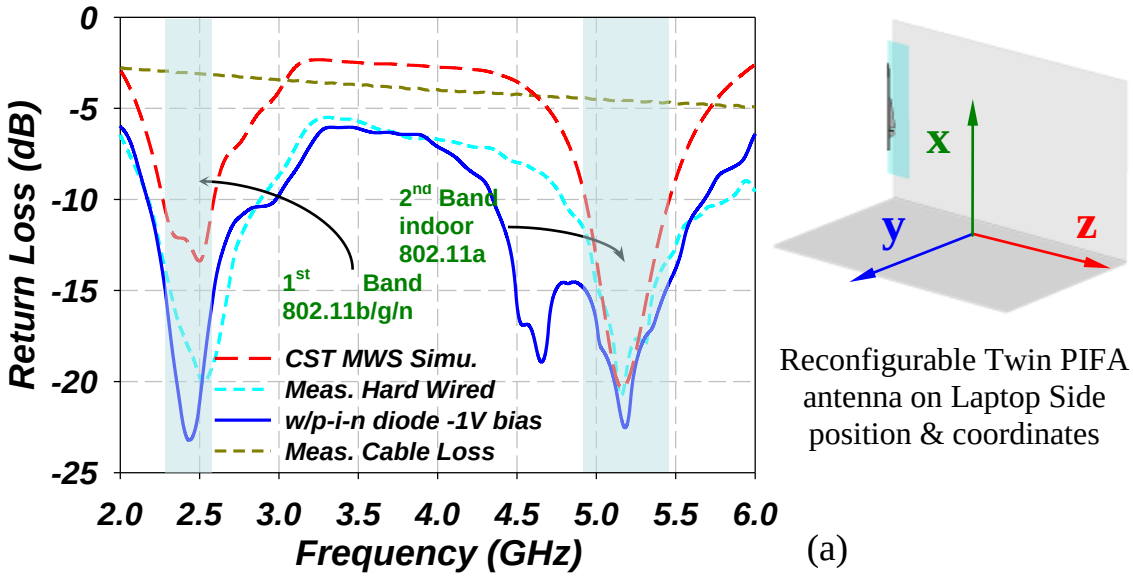

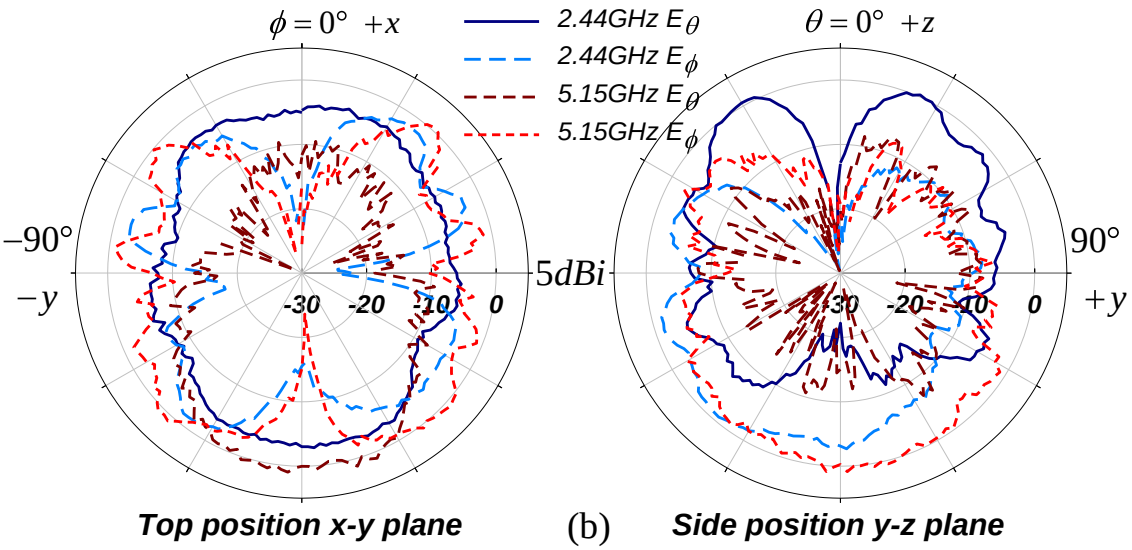

Figure 8.10 (a)Simulated and measured return loss of the WLAN configuration and (b) measured radiation patterns

Table 8-4 Measured Gain of Twin PIFA Antennas with Switches

Frequency (GHz)		0.96	1.92	2.4	5.15
Gain (dBi) Max/Average	Top	2.8/-0.1	1.7/-2.8	0.1/-2.8	2.7/-2.1
	Side	-0.2/-3.0	2.3/-0.8	0.6/-3.1	1.0/-4.4

8.3.3 Reconfigurable Dual PIFA Antenna Efficiency

In order to evaluate the efficiency of the reconfigurable antenna with switches, the average gain is measured with different biasing current conditions and compared to its hard–wired counterpart. As shown in Figure 8.11, as the biasing current increases, the series resistance of p-i-n diode reduces and gain increases. However, after 100mA, the gain start to saturate, and the DC consumption becomes prohibitively high for mobile platform. A bias current around 50mA is desirable for both antenna gain and battery life.

8.4 Conclusion

Reconfigurable multi-band antennas have great potential. Therefore, we have developed tow novel concepts and are introduced here. The first is a meandered monopole structure suitable for all WWAN and WLAN services after bandwidth enhancement. This structure, with its demonstrated excellent gain and omni-directional performance, can be utilized for mobile handsets. Meanwhile the second is a reconfigurable multi-band PIFA antenna which can support the GSM850 and PCS services in one configuration and the WLAN frequencies in the other. With its low profile, it can be embedded into laptop lids. P-i-n diodes have been utilized and integrated with these antennas, and the overall performance of this antenna, as expected, is a function of the driving current.

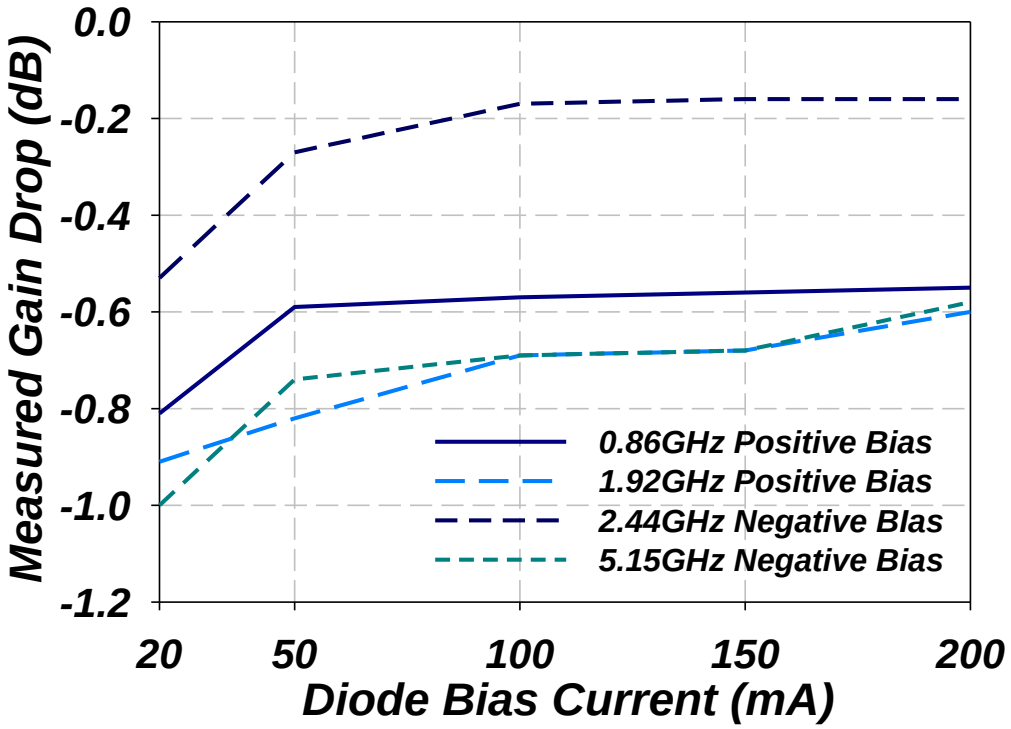

Figure 8.11 Measured average gain drop comparing with hard-wired version at various p-i-n diode biasing conditions

Chapter 9

Conclusions & Future Work

For both the mobile DBS and multi-radio wireless platforms, low profile, low cost antennas have been introduced and successfully developed. With the developed antennas, these communication links' flexibility have been greatly improved by extending the services to mobile platforms for the DBS case and supporting more radios with less number of antennas for the wireless case. Several contributions have been presented in this dissertation and they will be summarized in this chapter.

9.1 Contributions

First and foremost, the travelling wave slotted waveguide and substrate integrated waveguide (SIW) antenna array with symmetric radiating elements have been analyzed. A systematic design procedure of the radiating elements of such array with optimum gain and low sidelobe level is summarized. Several waveguide and SIW slot arrays have been implemented according to the procedure, including a multi-layer slotted SIW array with 32 radiating SIWs on the top layer and a tapered low loss feed networks folded to the back layer. Field tastings were carried out on the developed prototypes, where the developed antenna have demonstrated their capable to acquire the TV signals from the

satellite and have a good reception of all the channels under most weather conditions in Knoxville area.

Second, the propagation and attenuation properties of the SIW structure have been fully characterized. An equivalent dielectric filled waveguide model has been introduced to allow a systematic and straightforward estimation of feed network losses and an easy "translation" of waveguide radiating elements and junction components to SIW implementation.

Third, the synthesis equations for the design of waveguide and SIW T-junction power dividers with arbitrary power split ratio have been successfully developed. Various wideband transitions have been designed and implemented in the slotted SIW array antenna, including transitions from CPWG to SIW and between two stacked layers of a multi-layer SIW structure

Fourth, several single band reconfigurable antennas have been developed including a new wire antennas concepts based on fractal structures, which is suitable for reconfiguration with low number of switches. Two SPST MEMS switches are implemented in the developed structure to allow covering of three distinct wireless frequency bands in three configurable states.

Fifth, a novel concept of reconfigurable multi-band antenna is introduced, where multitudes of switches are used to hop between several multi-band configurations and the advantages of both the multi-band and the reconfigurable antenna structures can be simultaneously achieved while supporting more services. Two design examples of reconfigurable multi-band antennas are given including a meandered monopole antennas for mobile handsets and Twin PIFA antennas for laptop computers.

Last but not least, novel DC bias line topology is introduced to eliminate their parasitic radiation and simplify the biasing of these switches. New switch models have been

developed and their placements have been studied here to allow easy integration of these switches in an antenna environment, i.e. far from the ground plane.

9.2 Direction of Future Work

The concepts and ideas discussed previously in this dissertation offers promising solutions for both the development of low profile antenna arrays for mobile DBS applications and the design of reconfigurable antennas for multi-radio wireless mobile platforms. They also reveal several interesting directions for future research.

9.2.1 Shared Aperture Slotted SIW Arrays for Mobile DBS

In this dissertation, a low profile, high efficiency, travelling wave slotted SIW array antenna has been developed to provide adequate gain for the reception of DBS signal in Knoxville, TN area under clear weather condition. A shared aperture approach could be used, where two to four of these 32 radiating SIWs slot sub-arrays are combined in phase after LNA stages, in order to achieve a higher reliability and an acceptable C/N ratio in more reception areas.

9.2.2 Reconfigurable "Filtenna" for Multi-Radio Wireless Platforms

Based on the results shown in this dissertation, the problem of multi-radio platforms is solvable and the architecture design can be more flexible and intelligent. I have also investigated the feasibility of combining the antennas and filtering functions into one, i.e. a novel multi-radio platform architecture, where the fixed filters on each wireless module are eliminated. Reconfigurable filters are added between the antenna and the antenna switches. Further research can be carried out to develop a novel reconfigurable structure to provide such combined antenna and filter functionalities, to which we refer as "filtennas," and eventually accomplish the reduction of the multi-radio platform complexity and its overall cost.

References

References

[1] **Richharia, M.** *Satellite Communication Systems Design Principles.* McGraw-Hill, Inc., 1995.

[2] **Gomez, Jorge Matos.** *Satellite Broadcast Systems Engineering.* Artech House Publishers, 2002.

[3] **Leon W. Couch, II.** *Digital and Analog Communication Systems.* Pearson Education, 2005.

[4] *An Embedded Antenna for Mobile DBS.* **J. Wang, J.H. Winters.** Monterey, CA, 2004. IEEE AP-S International Symposium on Antennas and Propagation. pp. 4092-4095.

[5] *Efficiency Calculation of Feed Structures and Optimum Number of Antenna Elements in a Subarray for Highest G/T.* **Demir, Simsek.** April 2004, IEEE Transactions on Antennas and Propagation, Vol. 52, pp. 1024-1029.

[6] *Elliptically Polarized Leaky-Wave Array.* **Getsingger, W. J.** March 1962, IRE Transactions on Antennas and Propagations, pp. 165-171.

[7] *Circularly Polarized Slot Radiators.* **Simmons, Alan J.** January 1957, IRE Transactions on Antennas and Propagation, pp. 31-36.

[8] **Balanis, Constantine A.** *Advanced Engineering Electromagnetics.* Wiley & Sons, 1989.

[9] **Elliott, Robert S.** *Antenna Theory and Design (Revised Edition).* John Wiley & Sons, Inc., 2003.

[10] *A Two-Beam Slotted Leaky Waveguide Array for Mobile Reception of Dual-Polarization DBS.* **Kunio Sakakibara, Yuchi Kimura, Jiro Hirokawa, Makoto Ando, Naohisa Goto.** January 1999, IEEE Transactions on Vehicular Technology, Vol. 48.

[11] *Leaky-Wave Antennas I: Rectangular Waveguides.* **L. O. Goldstone, A. A. Oliner.** October 1959, pp. 307-319.

[12] **Hanson, R.C.** *Phased Array Antennas.* John Wiley & Sons Inc., 1997.

[13] *Analysis of a Centered-Inclined Waveguide Slot Coupler*. **Rengarajan, Sembiam R.** May 1989, IEEE Transactions on Microwave Theory and Techniques, Vol. 37, pp. 884-449.

[14] *A Direct Computation of the Frequency Response of Planar Waveguide Slot Arrays.* **G.A. Casula, G.Mazzarella.** July 2004, IEEE Transactions on Antennas and Propagation, Vol. 52, pp. 1909-2004.

[15] *Slotted Arrays for Low Profile Mobile DBS Antennas.* **S. Yang, A.E. Fathy.** Washington, DC, 2005. Proceeding of IEEE AP-S Internatinal Symposium on Antennas and Propagation. pp. 2011-2014.

[16] *Slot Arrays antennas for Mobile DBS.* **S. Yang, A.E. Fathy.** Monticello, IL, 2005. Proceeding of Antenna Applications Symposium. pp. 496-509.

[17] *Synthesis of a Compound T-Junction for a Two-Way Splitter with Arbitrary Power Ratio.* **S. Yang, A.E. Fathy.** Long Beach, CA, 2005. Proceeding of IEEE MTT-S International Microwave Symposium. pp. 985-988.

[18] *Integrated Microstrip and Rectangular Waveguide in Planar Form.* **D. Deslandes, K. Wu.** February 2001, IEEE Microwave and Wireless Component Letter, Vol. 11, pp. 68-70.

[19] *Guided-Wave and Leakage Characteristics of Substrate Integrated Waveguides.* **F.Xu, K. Wu.** January 2005, IEEE Transaction on Microwave Theory and Techniques, Vol. 53, pp. 66-73.

[20] *Synthesis of an Arbitrary Power Split Ratio Divider Using Substrate Integrated Waveguide.* **S. Yang, A.E. Fathy.** Honolulu, HI, 2007. Proceeding of IEEE MTT-S International Microwave Symposium. pp. 427-430.

[21] *An analysis of a waveguide T Junction with an Inductive Post.* **J. Hirokawa, K. Sakurai, M. Ando, N. Goto.** March 1991, IEEE Transactions on Microwave Theory and Techniques, Vol. 39, pp. 563-566.

[22] *Two-way Power Divider for Partially Parallel Feed in Single Layer Slotted Waveguide Arrays.* **K. Fukazawa, J. Hirokawa, M. Ando, and N. Goto.** June 1998, IEICE Transactions on Communication, Vols. E81-B, pp. 1248-1253.

[23] *A Single-Layer Power Divider for a Slotted Waveguide Array Using pi-Junctions with an Inductive Wall.* **T.Takahashi, J. Hirokawa, M. Ando, N. Goto.** January 1996, IEICE Transactions on Communication, Vols. E79-B, pp. 57-61.

[24] *Integrated Transition of Coplanar to Rectangular Waveguides.* **D. Deslandes, K Wu.** Phoenix, AZ, 2001. Proceeding of IEEE MTT-S International Microwave Symposium. pp. 619-622.

[25] *Analysis and Design of Current Probe Transition From Grounded Coplanar to Substrate Integrated Rectangular Waveguides.* **D. Deslandes, K. Wu.** August 2005, IEEE Transactions on Microwave Theory and Techniques, Vol. 53, pp. 2487-2494.

[26] *A High Efficient Vivaldi Antenna Array Design on Thick Substrate and Fed by SIW Structures with Integrated GCPW Feed.* **S. Yang, A. Elsherbini, S. Lin, A.E. Fathy, A. Kamel, H. Elhennawy.** Honolulu, HI, 2007. Proceeding of IEEE AP-S International Symposium on Antennas and Propogation. pp. 1985-1988.

[27] *UWB Tapered Slot Antenna Array Using SIW Technology.* **S. Lin, S. Yang, A.E. Fathy.** Montecello, IL, 2007. Proceeding of Antenna Applications Symposium. pp. 181-192.

[28] *Experimental Development of a Circularly Polarized Antipodal Tapered Slot Antenna Using SIW Feed Printed on Thick Substrate.* **S. Lin, A. Elsherbini, S. Yang, A.E. Fathy, A. Kamel, H. Elhennawy.** Honolulu, HI, 2007. IEEE AP-S International Symposium on Antennas and Propagation. pp. 1533-1536.

[29] *Ku-Band Slot Array Antennas for Low Profile Mobile DBS Application.* **S. Yang, S.H. Suleiman, A.E. Fathy.** Albuquerque, NM, 2006. Proceeding of IEEE AP-S International Symposium on Antennas and Propagation. pp. 3137-3140.

[30] *Evaluation of a Ku Band Printed Circuit Slot Array Antenna Using Planar Near-field Measurements.* **S.H. Suleiman, S. Yang, A.E. Fathy.** Albuquerque, NM, 2006. Proceeding of IEEE AP-S International Symposium on Antennas and Propagation. pp. 433-436.

[31] *Development of a Slotted Substrate Integrated Waveguide (SIW) Array Antennas for Mobile DBS Applications.* **S.Yang, S.H. Suleiman, A.E. Fathy.** Monticello, IL, 2006. Proceeding of Antenna Applications Symposium. pp. 103-131.

[32] *Low Profile Multi-Layer Slotted Substrate Integrated Waveguide (SIW) Array Antenna with Folded Feed Network for Mobile DBS Applications.* **S. Yang, S.H. Suleiman, A.E. Fathy.** Honolulu, HI, 2007. Proceeding of IEEE AP-S International Symposium on Antennas and Propagation. pp. 473-476.

[33] *Cavity Backed Patch Shared Aperture Antenna Approach for Mobile DBS Applications.* **S. Yang, A.E. Fathy.** Albuquerque, NM, 2006. Proceeding of IEEE AP-S International Symposium on Antennas ans Propagation. pp. 3959-3962.

[34] **Balanis, Constantine A.** *Antenna Theory: Analysis and Design, (Third Edition).* Wiley-Interscience, 2005.

[35] *Fractal Antennas: A Novel Antenna Miniagurization Technique, and Applications.* **John P. Gianvittorio, Yahya Rahmat-Samii.** February 2002, IEEE Intennas and Propagation Magazine, Vol. 44.

[36] *A Novel Reconfigurable Maze Antenna for Multi-service Wireless Universal Receivers.* **S. Yang, H.K. Pan, A.E. Fathy, S.M. El-Ghazaly and V.K. Nair.** San Diego, CA, 2006. Proceeding of IEEE MTT-S Radio and Wireless Symposium. pp. 195-198.

[37] *RF MEMS Reconfigurable Trangular Patch Antenna.* **L.M. Feldner, C.D. Nordquist.** 2005. Proceeding of the IEEE AP-S International Symposium on Antennas and Propatation.

[38] *Patch Antenna with Switchable Slot (PASS) in Wireless Communications: Concepts, Designs, and Applications.* **Fan Yang, Yahya Rahmat-Samii.** April 2005, IEEE Antennas and Propagation Magazine, Vol. 47.

[39] *A Novel Radiation Pattern and Frequency Reconfigurable Signle Turn Square Spiral Microstrip Antenna.* **G.H. Huff, J. Feng, S. Zhang and J.T. Bernhard.** February 2003, IEEE Microwave and Wireless Components Letter.

[40] *Planar Monopole Folded Into a Compact Structure for Very-Low-Profile Multi-Band Mobile Phone Antennas.* **Teng, P.L.** April 2002, Microwave and Optical Technology Letter, Vol. 33, pp. 22-25.

[41] *A Dual-Band Antenna For Cellular Applications.* **D. Liu, G. Gaucher, T. Hildner.** Albuquerque, NM, 2006. IEEE AP-S International Symposium on Antennas and Propagation. pp. 4689-4693.

Vita

Songnan Yang received his B.S.E.E. degree from Zhejiang University, P.R. China. In January 2004, he joined the direct Ph.D. program at the University of Tennessee, Knoxville in Electrical Engineering and completed his Doctor of Philosophy degree in 2008. His main research interests include the analysis and design of antennas and arrays for mobile platforms, including wireless and direct broadcast satellite (DBS) applications. As a graduate research and teaching assistant, he has gained experience teaching undergraduate level courses of "Antennas" and "Digital Communications".

Dr. Yang was a recipient of the 2007 IEEE MTT-S Graduate Fellowship. He was the winner of the 2008 IEEE Radio and Wireless Symposium Student Paper Competition, winner of the student paper competition of the 30th Antenna Applications Symposium and 3rd place winner of the 2008 USNC/URSI National Radio Science Meeting Student Paper Competition. He received the URSI Young Scientist Award of the 2007 International Electromagnetic Theory Symposium. He was also the recipient of the 2007 Chinese Government Award for Outstanding Self-Financed Students Abroad, the 2006 University of Tennessee Chancellor's Citations Award for Extraordinary Professional Promise and the 2007 EECS Department Teaching Assistant of the Year Award.

In the summers of 2005 and 2006, and spring of 2008, he worked as an intern at Intel Corp, where he characterized the performance of various wireless radios collocated on a multi-radio platform, studied interference mitigation schemes, and developed reconfigurable antennas for laptops. Dr. Yang has more than 20 refereed journal and conference publications in the area of antenna/arrays and passive components. He also has two pending U.S. Patents. He is a member of Tau Beta Pi and Eta Kappa Nu, honor societies of Engineering and Electrical Engineering students respectively. He is also a student member of IEEE Antennas and Propagation Society and Microwave Theory and Techniques Society.